Usp22 is an intracellular regulator of systemic emergency hematopoiesis

Nikolaus Dietlein, Xi Wang, Jonas Metz, Olivier Disson, Fuwei Shang, Celine Beyersdörffer, Esther Rodríguez Correa, Daniel B Lipka, Yvonne Begus-Nahrmann, Robyn Laura Kosinsky, et al.

Title: Usp22 is an intracellular regulator of systemic emergency hematopoiesis

Authors: Nikolaus Dietlein[1,2,*], Xi Wang[1,3,#], Jonas Metz[2,4,#], Olivier Disson[5], Fuwei Shang[1,6], Celine Beyersdörffer[1], Esther Rodríguez Correa[1], Daniel B. Lipka[7,8], Yvonne Begus-Nahrmann[9], Robyn Laura Kosinsky[10], Steven A. Johnsen[11, 12], Marc Lecuit[5,13,14], Thomas Höfer[4] and Hans-Reimer Rodewald[1,*]

Affiliations:

[1]Division of Cellular Immunology, German Cancer Research Center, Im Neuenheimer Feld 280, 69120 Heidelberg, Germany.

[2]Faculty of Biosciences, Heidelberg University, Im Neuenheimer Feld 234, 69120 Heidelberg, Germany.

[3]State Key Laboratory of Reproductive Medicine, Nanjing Medical University, 101 Longmian Avenue, Nanjing 211166, China.

[4]Division of Theoretical Systems Biology, German Cancer Research Center, Im Neuenheimer Feld 280, 69120 Heidelberg.

[5]Institut Pasteur, Université de Paris, Inserm U1117, Biology of Infection Unit, 75015 Paris, France.

[6]Faculty of Medicine, Heidelberg University, Im Neuenheimer Feld 672, 69120 Heidelberg.

[7]Section Translational Cancer Epigenomics, Department of Translational Medical Oncology, German Cancer Research Center and National Center for Tumor Diseases, Im Neuenheimer Feld 581, 69120 Heidelberg, Germany.

[8]Faculty of Medicine, Otto-von-Guericke-University, Magdeburg, Germany

[9]Institute of Molecular Oncology, Göttingen Center of Molecular Biosciences (GZMB), University Medical Center Göttingen, Göttingen, Germany.

[10]Division of Gastroenterology and Hepatology, Mayo Clinic, 200 First St SW, Rochester, MN 55905, USA.

[11]Robert Bosch Center for Tumor Diseases, Stuttgart, Germany.

[12]Department of General, Visceral & Pediatric Surgery, University Medical Center Göttingen, Göttingen, Germany.

[13]Institut Pasteur, National Reference Center and WHO Collaborating Center Listeria, 75015 Paris, France.
[14]Necker-Enfants Malades University Hospital, Division of Infectious Diseases and Tropical Medicine, APHP, Institut Imagine, 75006, Paris, France
[#] These authors contributed equally.

[*] Correspondence: n.dietlein@dkfz.de and hr.rodewald@dkfz.de

Abstract: Emergency hematopoiesis is a concerted response aimed towards enhanced protection from infection, involving multiple cell types and developmental stages across the immune system. Despite its importance, the underlying molecular regulation remains poorly understood. The deubiquitinase USP22 regulates the levels of monoubiquitinated histone H2B (H2Bub1), which is associated with activation of interferon responses upon viral infection. Here we show that, in the absence of infection or inflammation, mice lacking *Usp22* in all hematopoietic cells display profound systemic emergency hematopoiesis, evident by increased hematopoietic stem cell proliferation, myeloid bias, and extramedullary hematopoiesis. Functionally, loss of *Usp22* results in elevated phagocytosis by neutrophilic granulocytes and enhanced innate protection against *Listeria monocytogenes* infection. At the molecular level, we found this state of emergency hematopoiesis associated with transcriptional signatures of myeloid priming, enhanced mitochondrial respiration, as well as innate and adaptive immunity and inflammation. Augmented expression of many inflammatory genes was linked to elevated locus-specific H2Bub1 levels. Collectively, a tunable epigenetic state promotes systemic emergency hematopoiesis in a cell-autonomous manner and enhances innate protection, paving potential ways towards immune enhancement.

One Sentence Summary: Loss of *Usp22* elicits a cellular and molecular program of emergency hematopoiesis and enhances innate protection *in vivo*.

Main Text:

INTRODUCTION

Emergency hematopoiesis is an alarm state of the immune system which may serve two purposes. First, elevated cell production compensates for greater cell loss during inflammation and infection *(1)*, and, second, 'pre-activation' of immunity facilitates more rapid clearance of infectious agents *(2)*. Consequently, enhanced hematopoietic stem cell (HSC) proliferation *(3-5)*, myeloid-biased cell production *(6)*, extramedullary hematopoiesis *(7)*, or enhanced resistance to infections *(2)* constitute hallmarks of emergency hematopoiesis. While pathogen-associated molecular patterns *(5, 8)* and inflammatory cytokines, including interferons, *(3, 4, 9-11)* can contribute to the state of emergency hematopoiesis, it remains unclear whether an intracellular program conserved across different cell types underlies and coordinates emergency hematopoiesis, or whether emergency hematopoiesis is primarily mediated by circulating inflammatory mediators acting through distinct signaling pathways. Nevertheless, intracellular molecular switches regulating steady state versus emergency hematopoiesis remain poorly understood.

Histone H2B monoubiquitination is an activating histone modification catalyzed by the RNF20/RNF40 E3 ubiquitin ligase complex *(12)*, and monoubiquitinated H2B (H2Bub1) is mainly found in the transcribed regions of highly expressed genes *(13)*. In cell lines, H2Bub1 levels increase at interferon-stimulated gene (ISG) loci upon viral infection and interferon stimulation, and RNF20 is required for proper ISG induction *(14)*. H2Bub1 can be deubiquitinated by USP22, the enzymatically active component of the SAGA deubiquitinase module *(15, 16)*. Collectively, these findings raise the intriguing possibility that *Usp22* might be involved in the restriction of ISG expression *in vivo*, and its downstream biological consequences, including emergency hematopoiesis.

To test this hypothesis and to uncover potential cell-intrinsic and systemic functions of *Usp22* in hematopoiesis and immunity *in vivo*, we analyzed conditional *Usp22* KO mice. We applied a range of approaches, including *in vivo* and *in vitro* hematopoiesis assays, bacterial infection, bulk and single cell transcriptome analysis, and epigenome profiling using ATAC and ChIP sequencing to study the role of USP22 in hematopoiesis. In a cell-autonomous manner, *Usp22* deficiency elicited typical signs of emergency hematopoiesis, including increased HSC proliferation, myeloid bias, and extramedullary hematopoiesis. Emergency hematopoiesis was accompanied by coordinated molecular changes in *Usp22* KO progenitors, comprising increased

expression of genes involved in mitochondrial respiration, transcriptional myeloid priming, and elevated expression of immune-related and inflammatory genes including interferon-stimulated genes (ISG). These cellular and molecular indicators of immune 'pre-activation' were functionally important as shown by heightened phagocytic activity of neutrophilic granulocytes and enhanced innate protection against *Listeria monocytogenes*. Mechanistically, many of the ISG that were upregulated in *Usp22* KO hematopoietic stem and progenitor cells (HSPC) concomitantly showed increased locus-specific H2Bub1 levels, suggesting a physical and functional link between enhanced H2B monoubiquitination and inflammatory gene expression. Collectively, we present evidence that loss, and potentially inhibition, of USP22 orchestrates in a cell-autonomous manner a transcriptional program promoting emergency hematopoiesis and enhanced innate immunity.

RESULTS

Loss of *Usp22* induces emergency hematopoiesis in the absence of infection

Usp22 is expressed throughout hematopoietic stem and progenitor cells, and across the immune system (fig. S1A). To study the effects of *Usp22* deficiency on hematopoiesis and the immune system *in vivo*, we generated pan-hematopoietic *Usp22* KO mice (termed *Usp22* KO hereafter) by crossing Vav1-Cre mice *(17)* with $Usp22^{flox/flox}$ mice (fig. S1B). Single cell genotyping revealed efficient deletion of the *Usp22* gene (fig. S1C). Within the hematopoietic system, loss of *Usp22* resulted in reduced numbers of phenotypic long-term (LT-) HSC (Fig. 1A), and increased numbers of short-term (ST-) HSC (fig. S1D) but had no effect on multipotent progenitor (MPP) numbers (fig. S1D) and bone marrow cellularity (fig. S1E). Proliferation of LT-HSC was enhanced in the absence of *Usp22* (Fig. 1B,C). Since increased HSC proliferation can be associated with HSC exhaustion, we performed serial, competitive bone marrow transplantations (fig. S1F). Like their wild type counterparts, *Usp22* KO bone marrow cells gave rise to multilineage repopulation in four rounds of transplantations (fig. S1G). Consequently, in serial transplantation experiments, *Usp22*-deficient HSC did not show signs of exhaustion.

Strikingly, *Usp22* KO mice showed strongly myeloid-biased numbers of mature cells in the bone marrow, evident by an increase in $CD11b^+$ $Gr\text{-}1^+$ myeloid cells (Fig. 1D), and a concomitant reduction of $B220^+$ B cells (Fig. 1E). To gain global insights into the cellular composition of the bone marrow in *Usp22*-deficient mice, we analyzed total bone marrow by single cell RNA sequencing (scRNA-seq) (Fig. 1F,G). Cell populations were identified based on

their transcriptome (Fig. 1F), and relative frequencies of populations were estimated (Fig. 1G; fig. S1H). This analysis uncovered the strongest increases in NK cells, granulocyte-monocyte progenitors (GMP), and granulocytes in *Usp22* KO relative to wild type bone marrow. In contrast, frequencies of B lymphocytes, dendritic cells, T cells, and erythroid progenitors were diminished in *Usp22* KO bone marrow (Fig. 1G; fig. S1H). Because of the marked enrichment of NK lineage cells, we phenotypically resolved pre-NK progenitors (NKP), NKP, and four stages of NK cell maturation (fig. S1I-L). The stage of increased numbers of NK lineage cells in the bone marrow was identified as $CD27^+$ $CD11b^-$ which corresponds to the most immature NK cells. Pre-NKP were reduced as well as more mature NK cells ($CD27^-$ $CD11b^+$). Impaired erythropoiesis in the bone marrow of *Usp22* KO mice was specified by analysis of stages of red blood cell development (fig. S2A).

In the spleens of *Usp22* KO mice, we found increased numbers of HSC (both LT-HSC and ST-HSC) and MPP (Fig. 1H), as well as increased GMP and megakaryocyte-erythrocyte progenitors (MEP) (Fig. 1I), suggesting mobilization of stem and progenitor cells from the bone marrow, and ongoing extramedullary hematopoiesis in the spleen. Consistent with extramedullary erythropoiesis, numbers of most erythroid differentiation stages were elevated in the spleens of *Usp22*-deficient mice (fig. S2B). Opposing effects on erythropoiesis in bone marrow and spleen led to normal hematocrit in *Usp22* KO mice (fig. S2C).

Collectively, *Usp22*-deficient mice displayed key cellular hallmarks of emergency hematopoiesis, which normally occurs strictly in response to infection or inflammation. We therefore extensively surveyed *Usp22* KO and wild type control mice for pathogens, which yielded no indications of infections (Table S1). Furthermore, serum levels of eleven inflammation-associated cytokines (fig. S3A), as well as IFN-α, IFN-β and IFN-γ (fig. S3B) were not elevated in *Usp22* KO compared to wild type mice. To look for local effects in the bone marrow, we measured 40 infection- and inflammation-associated proteins in bone marrow fluid, and again found no differences (fig. S3C). Taken together, *Usp22* deficiency leads to emergency hematopoiesis in the absence of infection or inflammation. This was evident by reduced LT-HSC numbers, enhanced LT-HSC proliferation, myeloid-biased cell numbers in the bone marrow, HSC mobilization, and extramedullary hematopoiesis in the spleen.

Enhanced myelopoiesis from *Usp22* KO bone marrow

Given that myelopoiesis is phenotypically and functionally central to emergency hematopoiesis *(2, 9, 10, 18)*, we dissected myeloid development in further detail. *Usp22* KO mice showed a strong accumulation of immature granulocytes in the bone marrow, which expressed low levels of Gr-1/Ly6G (Fig. 2A,B; fig. S4A,B), resembling 'left-shifted' granulopoiesis typically seen under inflammatory conditions *(6, 9)*. In line with inflammatory myelopoiesis, numbers of macrophages and Ly6C^{high} inflammatory monocytes, but not Ly6C^{low} patrolling monocytes, were also increased in *Usp22* KO bone marrow (Fig. 2C).

To analyze *in situ* hematopoietic output, including towards myeloid cells, upon loss of *Usp22*, we employed a strategy for endogenous fate mapping. For steady state hematopoiesis, output rates have been estimated based on label propagation emerging from Tie2^{+} HSC using Tie2-MeriCreMer(Tie2-MCM)-mediated induction of YFP expression (Rosa26-loxP-Stop-loxP-YFP) in response to tamoxifen *(19)* (Fig. 2D). We combined this system with conditional inactivation of *Usp22* by Tie2-MCM (Fig. 2E). Fractions of YFP-labeled cells were measured 14 weeks after tamoxifen pulse. The output of monocytes (Fig. 2F), and immature (B220^{+} CD43^{+}), but not mature (B220^{+} CD43^{-}), developing B cells (Fig. 2G) was larger in *Tie2$^{MCM/+}$ Rosa26$^{LSL\text{-}YFP/LSL\text{-}YFP}$ Usp22$^{flox/flox}$* mice compared to *Tie2$^{MCM/+}$ Rosa26$^{LSL\text{-}YFP/LSL\text{-}YFP}$ Usp22$^{+/+}$* mice. Granulocyte output was also larger but the difference did not reach statistical significance ($p = 0.053$) (Fig. 2F). These findings provide evidence for enhanced output, including the generation of monocytes and immature B cells *in vivo*. Together, hematopoiesis in *Usp22* KO bone marrow is characterized by an abundance of immature granulocytes, macrophages and inflammatory monocytes, and by enhanced output *in situ*.

Usp22 deficiency drives enhanced myelopoiesis in a cell-intrinsic manner

In response to infection, emergency myelopoiesis is driven by circulating pro-inflammatory cytokines such as G-CSF, IL-6 and type I IFN *(9-11)*. In contrast, our cytokine profiling in serum and bone marrow fluid of *Usp22* KO mice revealed no indication that these or other tested mediators of emergency myelopoiesis were elevated. This raised the intriguing possibility that emergency hematopoiesis in *Usp22* KO mice resulted from a cell-autonomous mechanism in cis rather than systemically between cells in trans. We first tested this idea by competitive transplantation of *Usp22*-deficient and wild type bone marrow cells into lethally irradiated recipients (Fig. 3A). Donor B cells were mostly from wild type origin, while contributions of wild

type and *Usp22*-deficient donors to myeloid cells were similar (Fig. 3B). Comparison of the ratios of B versus myeloid output revealed a myeloid bias within *Usp22*-deficient donor cells compared to wild type donor cells (Fig. 3C). Of note, the accumulation of immature granulocytes re-emerged specifically from *Usp22* KO but not wild type competitor donor bone marrow cells (Fig. 3D). Myeloid-biased output from *Usp22*-deficient cells was also evident when purified HSC were competitively transplanted (fig. S4C). Hence, the myeloid bias and 'left-shifted' emergency granulopoiesis were reproduced after adoptive transfer of *Usp22* KO bone marrow cells into wild type hosts, implying that enhanced myelopoiesis is cell-intrinsic to *Usp22* KO HSC or bone marrow cells and independent from systemic factors.

To probe the contribution of committed progenitors to enhanced myelopoiesis, we transplanted *Usp22* KO or wild type common myeloid progenitors (CMP), each with wild type competitor bone marrow cells, into lethally irradiated recipient mice (Fig. 3E). At 7 and 10 days post-transplantation, *Usp22* KO CMP contributed more strongly to myeloid compartments in peripheral blood (Fig. 3F), bone marrow and spleen (Fig. 3G), and produced larger absolute numbers of myeloid cells compared to wild type CMP (fig. S4D). Hence, *Usp22*-deficient CMP generated more output on a per cell basis compared to wild type CMP. Enhanced myelopoiesis by *Usp22* KO CMP was cell-autonomous since it was not transferable to wild type competitor cells within the same host (fig. S4D). *Usp22* KO CMP did not persist long term as their contribution to peripheral myeloid cells disappeared by 21 days after transplantation (fig. S4E).

We also observed that myeloid-biased differentiation of *Usp22*-deficient HSPC was apparent *in vitro*. When we cultured wild type and *Usp22* KO HSPC under conditions actively promoting B cell development *(20, 21)*, wild type progenitors gave rise, as expected, to $B220^+$ $CD11b^-$ B lineage cells. In contrast, *Usp22*-deficient progenitors yielded almost exclusively $B220^-$ $CD11b^+$ myeloid lineage cells (Fig. 3H,I). Importantly, in mixed cultures composed of wild type ($CD45.1^+$) and *Usp22* KO ($CD45.2^+$) HSPC, *Usp22*-deficient progenitors again gave rise to myeloid cells while the B cell fate of wild type cells was unperturbed in the presence of *Usp22*-deficient cells. In control cultures composed of $CD45.1^+$ and $CD45.2^+$ wild type HSPC, both progenitors gave rise to B cells (fig. S4F; Fig. 3J,K). Thus, *Usp22* KO progenitors generate myeloid cells even under B cell promoting conditions in a cell-intrinsic manner. This phenotype was not transmittable to co-cultured wild type cells. Additionally, following transduction with a retroviral vector expressing *Usp22* cDNA, cells regained B cell potential (fig. S4G,H). Hence the

developmental bias from B to myeloid lineages is reversible within days upon *Usp22* re-expression. In summary, loss of *Usp22* enhances myeloid output from HSPC and myeloid progenitors *in vivo* and *in vitro* in a cell-autonomous manner. This bias is reversible upon restoration of *Usp22* expression in *Usp22*-deficient progenitors.

Usp22 deficiency enhances innate protection from *Listeria monocytogenes* infection and phagocytosis by neutrophilic granulocytes

To address whether the observed comprehensive signs of emergency hematopoiesis were functionally relevant, we used an established infection model probing early innate defense *(22)*. We infected wild type and *Usp22* KO mice intravenously with a dose of 10^4 colony-forming units (CFU) *Listeria monocytogenes* and determined bacterial burden three days post-infection in blood, and tissue homogenates of brain, liver and spleen. Interestingly, *Usp22* KO mice were markedly more protected, with CFU reduced by one or two orders of magnitude compared to infected wild type mice (Fig. 4A). These data support the conclusion that the state of emergency hematopoiesis brought about by *Usp22* deficiency is associated with increased innate defense against bloodborne bacterial infection.

To directly test a key anti-bacterial function, we measured *in vitro* phagocytosis of fluorescently-tagged E.coli particles (Fig. 4B, C) as well as live E.coli (Fig. 4D) by *ex vivo* purified neutrophilic granulocytes from non-infected wild type and *Usp22* KO mice. Purification selected for granulocytes expressing high levels of Ly6G in both genotypes (fig. S5A). In line with protection against bacteria in the *Listeria* model *in vivo*, enhanced phagocytosis was detected in *Usp22* KO compared to wild type granulocytes in both assays (Fig. 4B-D). Enhanced phagocytosis upon loss of *Usp22* was specific to neutrophils, since it was not apparent in *Usp22*-deficient bone marrow-derived macrophages or peritoneal macrophages (fig. S5B,C). *Usp22* KO neutrophils also showed enhanced TNF-α production *in vitro* upon LPS stimulation but not under steady state conditions (Fig. 4E). Thus, *Usp22* deficiency promotes anti-bacterial innate immunity, at least in part by enhancing neutrophilic granulocyte effector functions.

Usp22 deletion cell-intrinsically impairs B lymphocyte development

Inflammatory stimuli, such as type I interferons or adjuvants, are known to not only enhance myelopoiesis but also to impair B lymphocyte development, leading to reduced numbers of B cell

progenitors in the bone marrow *(6, 23-25)*. Indeed, B cell numbers in the bone marrow of *Usp22* KO mice were diminished (Fig. 1E-G), and dissection of B cell development *(26)* revealed a strong reduction in fraction D ($B220^+$ $CD43^-$ IgM^-) and onwards stages (fig. S6A,B). The decrease of more mature B cells in *Usp22* KO mice was also evident by the altered proportions of $CD43^+$ (more immature) versus $CD43^-$ (more mature) $B220^+$ cells (fig. S6C). The partial developmental block at the transition to the pre-B cell stage (fraction D) was associated with increased apoptosis of pre-B cells and following stages (fig. S6D). The stage of the developmental impairment and the increase in apoptosis resemble effects of *Myc* deficiency on B cell development *(27)*. In line with this notion, RNA sequencing showed strongly decreased expression of *Myc* and *Myc* target genes in *Usp22*-deficient pre-B cells (fig. S6E).

To test whether impaired B cell development in *Usp22* KO mice occurred cell-autonomously, we competitively transplanted *Usp22*-deficient or wild type donor bone marrow cells together with wild type competitor bone marrow cells into lethally irradiated recipients (fig. S6F). The partial block in B cell development, reflected by the larger proportion of $CD43^+$ $B220^+$ cells, was recapitulated in *Usp22*-deficient but not in wild type cells transferred into the same hosts (fig. S6G). As a consequence of impaired B cell development, absolute numbers of splenic $B220^+$ $CD19^+$ B cells were reduced in *Usp22*-deficient mice (fig. S6H), mainly resulting from a reduction in follicular B cells ($CD19^+$ IgM^- IgD^+ $CD93^-$) (fig. S6I). Collectively, *Usp22* KO mice show a cell-intrinsic incomplete block in B cell development which still permits the generation of all splenic B cell subsets.

Loss of *Usp22* enhances inflammatory gene expression in HSPC

To gain insights into the molecular mechanisms underlying emergency hematopoiesis in *Usp22* KO mice, we compared gene expression of wild type and *Usp22* KO HSPC by RNA sequencing, which identified 380 differentially expressed genes (DEG) (212 up- and 168 downregulated in *Usp22* KO HSPC) (Fig. 5A). Gene ontology (GO) term enrichment analysis showed that genes upregulated in *Usp22*-deficient HSPC were associated with inflammation and immune responses, including interferon-stimulated genes (ISG) (GO terms “cellular response to IFN-β” and “cellular response to IFN-γ”, Fig. 5B). Expression of individual DEG within relevant GO terms identified in Fig. 5B is shown in Fig. 5C. Gene set enrichment analysis (GSEA) revealed enhanced expression of both IFN-α and IFN-γ target genes in *Usp22* KO HSPC (fig. S7A), and intersecting

DEG with a comprehensive set of ISG previously found across immune cells *(28)* identified large numbers of ISG upregulated in *Usp22*-deficient HSPC (fig. S7B). Hence, loss of *Usp22* enhances inflammatory gene expression in HSPC in the absence of infection or elevated levels of pro-inflammatory cytokines.

To test whether gene expression changes in *Usp22*-deficient HSPC occurred in a cell-intrinsic manner, we performed RNA sequencing of HSPC isolated from mixed bone marrow chimeras in which *Usp22* KO and wild type bone marrow cells were co-transplanted into the same recipients (Fig. 5D). Transcriptome comparison of *Usp22* KO and wild type HSPC derived from the same hosts (Fig. 5D, bottom panel) identified 153 DEG (68 up- and 85 downregulated in *Usp22* KO) (Fig. 5E). Only a few of the transcriptome changes resulted from the different CD45 allotypes (i.e. donor markers for wild type and *Usp22* KO cells) (fig. S7C-E). Interestingly, transcriptome changes identified in '*ex vivo*' isolated *Usp22* KO HSPC specifically reemerged in transplanted *Usp22*-deficient HSPC but not in wild type HSPC in mixed bone marrow chimeras (Fig. 5F), independent of the CD45 allotype (fig. S7F). In line with the findings from our RNA sequencing experiments, *Usp22* KO HSPC showed increased cell surface expression of MHC class II (MHC II), higher expression of *Stat-1* mRNA and protein, increased *Ifi47* mRNA expression, and elevated MPO protein levels (fig. S8A-E). While most of these are IFN-regulated genes, serum concentrations of IFN-α, IFN-β and IFN-γ were not elevated in *Usp22* KO compared to wild type mice (fig. S3B), and expression of the receptors for type I or type II IFN was not increased (fig. S8F,G). Despite enhanced inflammatory gene expression, Sca-1 levels were not increased in *Usp22* KO HSPC (fig. S8H). Collectively, loss of *Usp22* in hematopoietic cells leads to increased expression of inflammation-associated genes, including ISG. In agreement with absence of elevated systemic interferon levels or signs of infections, gene expression changes in *Usp22* KO cells were not transmittable to wild type cells. Therefore, *Usp22* acts as a cell-intrinsic repressor of inflammatory gene expression.

Usp22 deficiency enhances myeloid transcriptional priming

To investigate transcriptional programs involved in HSPC differentiation in wild type and *Usp22* KO mice, we generated scRNA-seq data of sorted LT-HSC, ST-HSC and MPP from two independent experiments (for details see table S2). We first focused on MPP to explore molecular determinants of the myeloid bias in *Usp22* KO mice. MPP were analyzed for cells that coherently

expressed lineage genes (using SingleR *(29)*), resembling common lymphoid progenitors (CLP), granulocyte-monocyte progenitors (GMP) and megakaryocyte-erythroid progenitors (MEP). We then identified putative differentiation trajectories of these subpopulations from the more immature MPP. We used FateID *(30)* for identifying an informative subset of lineage-specific genes, ordering cells via diffusion map and applying Slingshot *(31)*). Based on trajectory structure and cell-type labels, we defined the following MPP subsets: GMP-biased (branch with MPP resembling GMP), MEP-biased (branch with MPP resembling MEP or CFU-E), lymphoid primed MPP (LMPP) (branch with MPP resembling CLP), and unbiased MPP (cells not assigned to any branch) (Fig. 6A [Exp. 1]; fig S9A [Exp. 2]). This classification was consistent with expression levels of lineage-defining transcription factors (fig. S10), and correlated well with transcriptional signatures *(32)* of previously described lineage-biased MPP subsets *(33)* (fig. S9B).

While the overall topology of these trajectories was similar comparing wild type and *Usp22* KO mice, GMP-biased MPP were increased at least ~1.4-fold, and LMPP were reduced at least ~1.4-fold in *Usp22* KO mice (Fig. 6A; fig S9A). Consistent with enhanced myelopoiesis and NK cell expansion, we observed elevated expression of key transcription factor genes, e.g. *Irf8* and *Cebpb* (both up in GMP-biased MPP), and *Id2* (up in all MPP subsets) (Fig. S10). Moreover, the expression of the GMP signature was increased across LT-HSC, ST-HSC and MPP subsets, while the lymphoid signature was decreased (fig. S11A-D). Unbiased differential expression analysis yielded 20 shared upregulated and 12 shared downregulated genes across MPP subsets. The upregulated genes included immune effector molecules, such as MHC class I and II, *Cd74*, *Stat-1*, and *Gbp3* (fig. S12A-E). Assigning cells to cell-cycle phase by characteristic transcripts, we found that the proportion of cells in G1 phase was decreased in all MPP subsets in *Usp22* KO mice, which suggests faster proliferation of these subsets (Fig. 6B, fig. S9C), consistent with increased EdU incorporation in MPP overall (fig. S9D). Taken together, these data suggest that the enhanced production of mature cells in *Usp22* KO mice is, at least in part, driven by accelerated proliferation of MPP, and that MPP differentiation has increased myeloid bias. Flow cytometry-based enumeration of lineage-biased MPP2 (MEP-biased), MPP3 (GMP-biased) and MPP4 (lymphoid biased) subpopulations showed only marginal differences between wild type and *Usp22* KO mice (fig. S9E). It is possible that under conditions of perturbation such as the emergency hematopoiesis seen in *Usp22*-deficient mice, existing phenotypic definitions of MPP may not accurately reflect lineage priming at MPP stages.

To look for coordinately regulated gene programs in MPP beyond lineage genes, we performed GSEA for GO terms, and grouped significantly enriched terms with overlapping gene sets. As in the bulk RNA sequencing analysis (Fig. 5), we found signatures concordant with activation of innate and adaptive immunity in *Usp22* KO MPP. Further gene sets indicated activation of metabolic processes, including energy metabolism via mitochondrial respiration, and biosynthetic processes (nucleotide metabolism and RNA processing), and are in line with enhanced proliferation of MPP (DNA replication, response to DNA damage stimulus) (fig. S13 [Exp. 1]; fig S14 [Exp. 2]).

Next, we analyzed highly differentially expressed genes (fold change > 1.2 or < 0.833) within GO groups (Fig. 6C, left panel; fig. S9F). These data showed a large number of immune-related genes, the majority of which are involved in innate immune responses. Expression of genes related to MHC I and II antigen presentation was also enhanced in *Usp22* KO MPP (Fig. 6C, right panel). In the first experiment, upregulation of *Mif* (macrophage migration inhibitory factor) and its receptor, *CD74*, contributed to nearly all GO immune subclusters (Fig. 6C, right panel). This also held true for clusters related to metabolism, consistent with the broad functions of *Mif* as a pro-inflammatory regulator of innate immunity *(34, 35)*. However, in the second experiment, *Mif* was only mildly upregulated whereas the upregulation of *Cd74* was consistent (fig. S9F).

Upregulated genes driving the enrichment of GO terms related to aerobic respiration indicated increased oxidative phosphorylation (Exp.1: *Cox6a1*, *Ndufs6*; Exp. 2: *Gadd45gip1*) (Fig. 6C, left panel; fig. S9F); similar terms were also enriched in LT-HSC (fig. S15; fig. S16; fig. S17). This may underlie the increased proliferation and differentiation of HSC and MPP in *Usp22* KO mice, as the switch from glycolysis to oxidative phosphorylation is a driver of HSC proliferation and differentiation *(36-38)*. Moreover, reactive oxygen species (ROS) produced by respiration skew lineage commitment towards myeloid differentiation *(39, 40)*. In sum, the scRNA-seq analysis uncovered, in addition to the activation of innate immunity, a coordinated response of metabolic processes that is consistent with both increased differentiation and myeloid bias driven by *Usp22* KO.

Usp22 deficiency increases H2B monoubiquitination at ISG loci

USP22 serves as a deubiquitinase for monoubiquitinated H2B. Since H2Bub1 has been implicated in ISG transcription downstream of interferon receptor activation *(14)*, we reasoned that

inflammatory gene expression in *Usp22* KO HSPC might result from enhanced H2Bub1 levels. Therefore, we first determined levels of monoubiquitinated H2B by western blotting. Across all tested hematopoietic cell types, H2Bub1 levels were markedly increased in the absence of *Usp22* (Fig. 7A).

Next, we asked how greater H2Bub1 levels affected genome-wide DNA binding. To this end, we performed chromatin immunoprecipitation sequencing (ChIP-seq) for H2Bub1. Since H2Bub1 is mainly associated with gene bodies *(13)*, we focused our analysis on such regions. Our data revealed the typical pattern of gene body H2B monoubiquitination *(41)*, with H2Bub1 levels peaking at the beginning of the transcribed region and then decreasing towards the end of the gene body (fig. S18A). Consistent with RNA polymerase II-dependent recruitment of the RNF20/RNF40 complex *(42)*, H2Bub1 was absent in the gene bodies of non-expressed genes, and abundant in the transcribed regions of strongly expressed genes (fig. S18B). Both of these principle attributes of H2Bub1 were unaffected by *Usp22* deficiency (fig. S18A,B). By comparing *Usp22* KO and wild type HSPC, we identified 2198 genes which exhibited differential H2B monoubiquitination at their gene bodies (Fig. 7B). The vast majority of these loci showed enhanced H2Bub1 levels (2008 hyper- and 190 hypo-ubiquitinated loci in *Usp22* KO vs wild type) (Fig. 7B). To functionally annotate these genes, we performed GO term enrichment analysis, which revealed that hyper-ubiquitinated genes were associated, among other processes, with cytokine responses, defense responses, leukocyte activation and immune responses (Fig. 7C).

In order to link locus-specific H2Bub1 levels with gene expression, we next integrated H2Bub1 ChIP-seq data with bulk RNA sequencing data (Fig. 5). Genome-wide, there was little correlation between change in expression and change in gene body monoubiquitination (Fig. 7D, left panel). In contrast, this correlation was much higher for differentially expressed genes (Fig. 7D, right panel). Next, we focused on loci with the most robust changes ($p<0.05$, FC ≥ 1.5 or FC $\leq 1/1.5$) in both mRNA expression and gene body H2Bub1 levels upon loss of *Usp22* (Fig. 7E). In total, 118 genes fulfilled both criteria, 102 of which showed increased H2Bub1 levels (Fig. 7E, right quadrants), and 93 exhibited both enhanced H2B monoubiquitination and increased mRNA expression in *Usp22* KO HSPC (Fig. 7E, upper right quadrant). These 93 genes correspond to approximately 44 % of the total 212 genes with increased expression (Fig. 5A). Examples of locus-specific H2Bub1 profiles are shown for upregulated, hyperubiquitinated and downregulated, hypoubiquitinated genes (Fig. 7F and fig. S18C). Of note, upregulated, hyperubiquitinated genes

included important immune cell effector molecules, such as *H2-Ab1* and *Mpo* (Fig. 7F). Interestingly, the set of genes differentially expressed and differentially ubiquitinated in *Usp22* KO HSPC was highly enriched for ISG (Fig. 7G). Importantly, all of the ISG among the latter gene set consistently showed enhanced expression and elevated gene body H2Bub1 levels in *Usp22* KO cells (Fig. 7E, red dots). Consequently, loss of *Usp22* results in enhanced H2Bub1 levels and concomitantly increased expression at many ISG loci. To further visualize the effect of *Usp22* deficiency on H2B monoubiquitintion at ISG loci, we assessed average H2Bub1 levels across the gene bodies of interferon target genes, and found that these were elevated for all the classes of ISG analyzed (Fig. 7H; fig. S18D).

Finally, we complemented our analysis with ATAC sequencing to assess whether altered chromatin accessibility underlies the observed gene expression changes. Interestingly, both on average (fig. S18E), and when analyzing individual loci (fig. S18F), genes up- or downregulated in *Usp22* KO HSPC showed no changes in their promoter accessibility. Even the genes shown in Fig. 7E had no changes in their promoter accessibility (fig. S18G). Therefore, gene expression changes in *Usp22*-deficient cells occur independently of altered promoter accessibility. Taken together, our ChIP-seq experiments demonstrate that USP22 deubiquitinates H2Bub1 bound to DNA, and that levels of DNA-bound H2Bub1 are hence elevated in the absence of USP22. Genes that are both hyper-monoubiquitinated and strongly upregulated are highly enriched for ISG, and these changes in gene expression are independent of alterations in promoter accessibility.

DISCUSSION

Normally, hematopoiesis switches from steady state to emergency in response to infection and inflammation. At cellular and systemic levels, triggers mediating emergency hematopoiesis during infections include signals via pathogen-associated molecular patterns (PAMP) and increased concentrations of inflammatory cytokines. HSC and progenitors can directly sense and respond to PAMP *(5, 8)* and inflammatory cytokines *(3, 4, 43)*. Enhanced HSC proliferation *(3, 4)*, overproduction of myeloid cells, especially granulocytes, at the expense of lymphocytes *(6)*, as well as HSC mobilization and extramedullary hematopoiesis *(7)* constitute typical aspects of emergency hematopoieis. Intriguingly, we found all of these hallmarks in mice with pan-hematopoietic *Usp22* inactivation. The key difference we observed in *Usp22* KO mice compared to inflammation- or infection-associated emergency hematopoiesis, however, was an absence of

infections and lack of elevation of analyzed inflammatory cytokines, including G-CSF, IL-6 or type I IFN *(9-11)*. We therefore consider it unlikely that emergency hematopoiesis was induced in *Usp22* KO mice by the typical route via inflammation. Rather, we provide comprehensive data from co-culture experiments and mixed bone marrow chimeras demonstrating a cell-intrinsic and systemic cytokine-independent switch. Key phenotypes, including myeloid-biased hematopoiesis, 'left-shifted' granulopoiesis, impaired B cell development, and enhanced inflammatory gene expression, were not transferred from *Usp22* KO to wild type cells and not reverted in *Usp22*-deficient cells by the presence of wild type cells. While our data clearly show that cell-autonomous, system-wide emergency hematopoiesis can be elicited by loss of *Usp22*, it remains to be determined how *Usp22* expression and H2B monoubiquitination are regulated during inflammation- or infection-induced emergency hematopoiesis.

Enhanced myelopoiesis is currently considered the primary purpose of emergency hematopoiesis. In addition to the restoration of cellular homeostasis after infection, increased myeloid cell production may also provide innate protection against infection. However, because emergency hematopoiesis is experimentally or clinically tightly linked to infection or inflammation *(2)*, it is difficult to disentangle the contribution of emergency hematopoiesis to protective responses. The stronger innate protection of *Usp22* KO mice from *Listeria monocytogenes* infection that we observed might result from both quantitative and qualitative alterations of myeloid cell compartments. While increased myeloid cell numbers in *Usp22* KO mice might provide evidence for the former notion, enhanced phagocytic activity of *Usp22*-deficient neutrophils clearly supports the latter one. Therefore, we propose that emergency hematopoiesis modulates myelopoiesis both in a quantitative and qualitative manner. This idea is also supported by our transcriptome analysis. In line with the myeloid bias, enhanced expression of GMP-associated signatures was observed in HSC and MPP from *Usp22* KO mice, and in fact proportions of transcriptionally GMP-biased MPP were elevated. Among upregulated genes, we found the IFN-γ-inducible transcription factor *Batf2* which has been shown to promote myelopoiesis *(44)*. Collectively, these data provide a molecular underpinning for the enhanced myeloid cell production in *Usp22* KO mice. GO term enrichment analysis suggested elevated mitochondrial activity, which could accelerate differentiation of *Usp22* KO HSC *(38)*. However, direct metabolic studies of mutant and wild type HSC will be required to study mitochondrial activity.

Loss of *Usp22* further lead to the activation of a pro-inflammatory gene expression program in HSPC, including upregulation of a large set of ISG, which normally occurs in response to cytokines. Among these genes were important regulators of innate and adaptive immunity, including MHC II molecules (*H2-Aa*, *H2-Ab1*, *H2-Eb1*), their upstream co-activator (*Ciita*), and myeloid effector molecules (*Elane*, *Mpo*), all of which may contribute to enhanced innate protection by *Usp22* KO myeloid cells. Both stronger protection and the transcriptional 'immune activation' signature in stem and progenitors in *Usp22* KO mice are reminiscent of trained immunity, and future experiments will be required to determine similarities or uniqueness of both states.

Loss of *Usp22* resulted in elevated H2Bub1 levels, in agreement with the role of USP22 as a non-redundant H2Bub1 deubiquitinase in hematopoietic cells *(45-47)*. H2Bub1 is an activating chromatin mark, which can be mainly found in the gene body of expressed genes *(13)*. Perturbed H2B monoubiquitination only affects the expression of a minor fraction of the transcriptome *(41, 48)*, notably including genes induced by cell-extrinsic signals such as nutrient levels, hormones and growth factors *(41, 49, 50)*. These notions are in accordance with the limited number of DEG identified in *Usp22*-deficient hematopoietic progenitors (380 genes), many of which were genes normally induced by IFN. In cell lines, H2Bub1 levels increase at ISG loci in response to type I IFN, and *Rnf20*, the catalytically active component of the E3 ubiquitin ligase complex mediating H2B monoubiquitination, is required for efficient ISG induction *(14)*. Our H2Bub1 ChIP sequencing data demonstrate that loss of *Usp22* leads to increased H2Bub1 levels at dozens of ISG loci, which exhibited concomitant elevated expression, and therefore suggests that enhanced locus-specific H2B monoubiquitination is both required *(14)* and sufficient to drive ISG expression.

Transcriptome changes in *Usp22* KO cells occurred in the absence of altered chromatin accessibility, implying that enhanced ISG expression driven by *Usp22* deficiency and increased H2Bub1 levels are likely caused by events occurring after transcription factor binding and RNA polymerase II recruitment. H2Bub1 has been implicated in the positive regulation of transcriptional elongation *(51)*, which might account for the observed transcriptome changes in *Usp22*-deficient cells. Our data suggest that enhanced H2Bub1 levels are required for the development of the hematopoietic phenotypes seen in *Usp22* KO mice; however, the precise molecular mechanisms linking *Usp22* deficiency to increased inflammatory gene expression remain to be examined. In particular, the specificity in gene regulation upon loss of *Usp22* will

need to be explored given that the number of differentially ubiquitinated genes (DUG) was much larger than the number of DEG. Other chromatin modifications may play a role; for example, levels of H2Bub1 correlate positively with levels of activating histone modifications such as H3K4 methylation. H2Bub1-dependent genes are characterized by broad H3K4me3 peaks at their transcription start sites, which have been implicated in transcriptional elongation *(48)*. Finally, our data cannot rule out the involvement of alternative USP22 substrates identified by others, such as PU.1 *(45)* and SIRT1 *(52)*, in the development of emergency hematopoiesis in *Usp22* KO mice.

Taken together, our results demonstrate that loss of *Usp22* in hematopoietic cells induces phenotypic and functional emergency hematopoiesis in a cell-autonomous manner. These findings shed light on the molecular regulation of a broad state of immune pre-activation, including enhanced innate protection, and might hence have implications for the therapeutic manipulation of this process such as through inhibition of USP22.

MATERIALS AND METHODS

Study design

The aim of this study was to investigate system-wide functions of *Usp22* in the hematopoietic system. Using conditional *Usp22* KO mice, we first determined cellular phenotypes in the *Usp22*-deficient blood and immune system. We performed *in situ* lineage tracing, adoptive cell transfer experiments, and *in vitro* hematopoiesis assays to dissect changes in differentiation of *Usp22* KO stem and progenitor cells, and to distinguish cell-intrinsic from cell-extrinsic mechanisms. *In vivo Listeria monocytogenes* infections, and *in vitro* phagocytosis assays were used to probe important innate effector functions. Bulk and single cell RNA sequencing of wild type and *Usp22*-deficient stem and progenitor cells, combined with comprehensive computational analysis, were used to explore the molecular underpinnings of the observed phenotypes. RNA sequencing data were extended by qRT-PCR and flow cytometry for selected candidate target molecules. The effects of *Usp22* deficiency on H2B monoubiquitination were analyzed using Western Blotting. Transcriptome changes were linked with epigenetic alterations using ATAC-sequencing and ChIP-sequencing for H2Bub1. Detailed descriptions of the experimental, computational and statistical methods used in this study are given below. Sample size and replicates are indicated in the figure legends.

Mice

Usp22^{flox} mice (B6-Usp22$^{tm1c(KOMP)Wtsi}$) were crossed to *Vav1-Cre* (B6.Cg-*Commd10*$^{Tg(Vav1-icre)A2Kio}$/J) *(17)* to obtain *Usp22* KO mice. For fate mapping of LT-HSC, *Usp22*^{flox} mice were crossed to *Tie2-MeriCreMer* (B6;129P2-Tek$^{tm1.1(icre/Esr1*)Hrr}$) *(19) Rosa26-loxP-Stop-loxP-YFP* mice (Gt(ROSA)26Sor$^{tm1.1(EYFP)Cos}$) *(53)*. B6.SJL-Ptprc^{a} Ptprc^{b} mice (CD45.1/CD45.2) were used as recipients in transplantation experiments. Mice were kept in individually ventilated cages under specific pathogen-free conditions in the animal facility of the DKFZ. Age- and sex-matched young adult mice were used for all experiments. For most experiments, Cre-positive mice carrying two *Usp22* wild type alleles were used as wild type controls. Both male and female mice were used. No randomization and no blinding were done. All animal experiments were performed according to institutional and governmental regulations, and approved by the Regierungspräsidium Karlsruhe, Germany.

Bone marrow and CMP transplantation

Recipient mice were lethally irradiated with a split dose of 2 x 5.5 Gy using a Cs137 Gammacell 40 irradiator with three to four hours between irradiation cycles. Donor cells (in PBS) were injected into the tail veins. For competitive bone marrow transplantations, $1x10^6$ test bone marrow cells (derived from *Usp22* KO mice or wild type littermates, both CD45.2) were transplanted together with $1x10^6$ competitor bone marrow cells (CD45.1) into the same recipient (CD45.1/CD45.2). For serial competitive bone marrow transplantations, bone marrow cells isolated from recipient mice at the end of each transplantation round were re-transplanted ($3x10^6$ bone marrow cells per recipient (CD45.1/CD45.2)). For CMP transplantations, $1x10^4$ test CMP (derived from *Usp22* KO or wild type mice, both CD45.2) were transplanted together with $1x10^5$ lineage-depleted competitor bone marrow cells (CD45.1) into the same recipient (CD45.1 or CD45.1/CD45.2). For HSC transplantations, 100 sorted LT-HSC (from *Usp22* KO or wild type mice, both CD45.2) were transplanted together with 10^5 lineage-negative bone marrow cells (CD45.1) into the same recipient (CD45.1/CD45.2). Donor cells were isolated from age-matched male and female mice (5-13 weeks) and transplanted into cohorts of age-matched male and female recipient mice (7-18 weeks). Mice were kept on Neomycin containing drinking water (1.17 g/l) for two weeks after transplantation.

***In vivo* fate mapping of LT-HSC**

Tie2$^{MCM/+}$ *Rosa26*$^{LSL\text{-}YFP/LSL\text{-}YFP}$ *Usp22*$^{+/+}$ and *Tie2*$^{MCM/+}$ *Rosa26*$^{LSL\text{-}YFP/LSL\text{-}YFP}$ *Usp22*$^{flox/flox}$ mice were injected with tamoxifen on five consecutive days (1 mg per day) for Cre induction. After 14 weeks, mice were sacrificed, and the proportion of YFP-labeled cells within different hematopoietic cell compartments in the bone marrow was determined by flow cytometry. Labeling frequencies in myeloid and developing B cells were normalized to the labeling frequency of LT-HSC within the same mouse.

***Listeria monocytogenes* infection and CFU quantification**

Female wild type and *Usp22* KO mice were infected with 10^4 CFU *Listeria monocytogenes* (EGDe strain) by intravenous injection. Three days post-infection, mice were sacrificed, and blood and organs were aseptically harvested. Organs were homogenized in PBS using a tissue homogenizer.

Serial dilutions of blood and tissue homogenates were plated onto BHI to enumerate *L. monocytogenes* CFU.

Blood, serum and bone marrow fluid collection

Blood samples were collected by puncture of the submandibular vein, or by post mortem cardiac puncture. For flow cytometry, blood samples were collected into EDTA-coated tubes, and subjected to red blood cell lysis using RBC lysis buffer (BioLegend) before further processing as described below. For serum preparation, blood was collected into serum tubes, incubated for 30 minutes at room temperature to allow for coagulation, and centrifuged at 15,000g for 90 seconds. Serum samples were frozen in aliquots at -80°C. For bone marrow fluid collection, femora and tibiae were flushed with PBS supplemented with protease inhibitors. Cell suspensions were centrifuged, supernatants (bone marrow fluid) transferred into fresh tubes, and stored at -20°C.

Preparation of single cell suspensions from hematopoietic organs

Bones (tibiae, femura, pelvis and spine) were crushed in FACS buffer (PBS + 5 % FBS), and filtered through 40 μm cell strainers. Spleens were mashed with FACS buffer through pre-wetted 40 μm cell strainers using syringe plungers. Cell numbers were determined using a Cellometer Auto 2000 Cell Viability Counter (Nexcelom).

Flow cytometry and fluorescence activated cell sorting

Single cell suspensions, or lysed blood samples were blocked for 15 minutes in 10 % normal rat serum (diluted in FACS buffer) and stained for 20 minutes (45 minutes for NK and NKP stainings) in titrated dilutions of fluorescent dye-labeled antibodies (in FACS buffer) at 4°C. Live/dead cells were discriminated by Sytox Blue (Thermo Fisher Scientific). For the sorting of HSPC, CMP and B cell progenitors, bone marrow cells were subjected to lineage depletion prior to further antibody staining. Cells were labeled with biotinylated antibodies directed against lineage markers (CD4, CD8, CD11b, CD19 [omitted in the enrichment of B cell progenitors], Gr-1 and Ter119), and were depleted using anti-biotin microbeads (Miltenyi) on LS MACS columns (Miltenyi). Samples were analyzed on a LSRFortessa flow cytometer (BD Biosciences), or sorted on a FACSAria III cell sorter (BD Biosciences). Antibodies and second step reagents were: MPO-FITC (clone 2D4) from Abcam, BP-1-PE (BP-1), CD4-biotin (GK1.5), CD4-FITC (H129.19), CD8a-FITC (53-6.7),

CD11b-FITC (M1/70), CD19-biotin (1D3), CD43-APC and CD43-biotin (S7), CD45-FITC (30-F11), CD45.2-FITC (104), CD45R-APC, CD45R-FITC and CD45R-PerCP-Cy5.5 (RA3-6B2), CD93-BV421 (AA4.1), Gr-1-APC and Gr-1-PE (RB6-8C5), IgM-PE (R6-60.2), Kit-APC (2B8), Ly6G-PerCP-Cy5.5 (1A8), NK1.1-PE (PK136), Ter119-PE (TER-119) and Streptavidin-APC-Cy7 from BD Biosciences, CD3-BV421 (17A2), CD4-BV421 (GK1.5), CD8a-BV421 (53-6.7), CD11b-BV421 (M1/70), CD16/32-PE (93), CD19-BV421 and CD19-BV605 (6D5), CD21/35-PerCP-Cy5.5 (7E9), CD34-FITC (RAM34), CD44-BV605 (IM7), CD45-BV785 (30-F11), CD45.1-BV785 (A20), CD45.2-Alexa Fluor488 and CD45.2-BV605 (104), CD48-Alexa Fluor700 (HM48-1), CD49b APC-Fire750 (DX5), CD71-PE-Cy7 (RI7217), CD115-BV605 (AFS98), CD122-PerCP-Cy5.5 (TM-β1), CD127-PE (SB/199), CD150-PE and CD150-PE-Cy7 (TC15-12F12.2), CD244.2-PE-Cy7 (m2B4(B6)458.1), Gr-1-BV421 (RB6-8C5), IFNAR-1-PE (MAR1-5A3), IgD-APC (11-26c.2a), Kit-BV711 (2B8), Ly6C-PE (HK1.4), Ly6G-PerCP-Cy5.5 (1A8), NK1.1-BV421 (PK136), NKp46-BV605 (29A1.4), TCRγ/δ-BV421 (GL3) and Ter119-BV421 (TER-119) from BioLegend, STAT-1 unlabeled (D1K9Y) from Cell Signaling Technologies, BP-1-biotin (6C3), CD3-APC-eFluor780 (17A2), CD8a-biotin (53-6.7), CD11b-biotin (M1/70.15), CD11b-APC, CD11b-PE, CD11b-PE-Cy7, CD11b-PerCP-Cy5.5 (M1/70), CD16/32-PE-Cy7 (93), CD19-Qdot605 (6D5), CD23-PE-Cy7 (B3B4), CD24-APC-eFluor780 (M1/69), CD27-FITC (LG.7F9), CD34-eFluor660 (RAM34), CD45-PE-Cy7 (30-F11), CD45.1-PE-Cy7 (A20), CD45.2-APC (104), CD45R-PerCP-Cy5.5 (RA3-6B2), CD48-APC and CD48-FITC (HM48-1), CD49b-APC-eFluor780 (DX5), CD127-PE-Cy7 (A7R34), CD135-APC and CD135-PE (A2F10), F4/80-APC (BM8), Gr-1-biotin (RB6-8C5), IFNGR-1-PE (2E2), IgM-FITC (eB121-15F9), IgM-PE-Cy7 (II/41), Kit-APC-eFluor780 and Kit-PE (2B8), MHC II-APC and MHC II-APC-eFluor780 (M5/114.15.2), Rabbit IgG-Alexa Fluor 488 (polyclonal), Sca-1-PE-Cy7 and Sca-1-PerCP-Cy5.5 (D7), Ter119-biotin and Ter119-FITC (TER-119), Streptavidin-APC and Streptavidin-Qdot605 from Thermo Fisher Scientific.

EdU labeling

Mice received 100 μg EdU (Thermo Fisher Scientific) by intraperitoneal injection and were sacrificed two hours later. Bone marrow cells were isolated, depleted and stained as described above with the modification that Zombie Red dye (BioLegend) was used for live/dead cell discrimination. Afterwards, cells were subjected to Click chemistry based EdU detection using the

Click-iT Plus EdU Alexa Fluor 488 Flow Cytometry Kit (Thermo Fisher Scientific) according to the manufacturer's instructions. Samples were labeled with FxCycle Violet stain to assess DNA content, and data were acquired on a LSRFortessa flow cytometer (BD Biosciences).

Annexin V labeling

Bone marrow cells were isolated and stained as described above. Annexin V labeling was performed using the FITC Annexin V Apoptosis Detection Kit (BD Biosciences) according to the manufacturer's instructions with minor modifications. 10^6 bone marrow cells were labeled using 3 µl of FITC Annexin V. Sytox Blue was used for live/dead cell discrimination. Data were acquired on a LSRFortessa flow cytometer (BD Biosciences).

***In vitro* phagocytosis assay**

Neutrophilic granulocytes were purified by magnetic cell separation using anti-Ly6G antibody (clone 1A8) from bone marrow of wild type and *Usp22* KO mice. Bone marrow-derived macrophages (BMDM) were differentiated from total bone marrow cells for 5 days in the presence of M-CSF (10 ng/ml). Peritoneal macrophages were obtained by pertitoneal lavage. Equal numbers of neutrophils, BMDM or peritoneal macrophages were seeded onto 24-well plates and incubated with pHrodo red-labeled *E. coli* particles for two hours at 37°C. Cells were harvested, washed with PBS and analyzed on a LSRFortessa flow cytometer (BD Biosciences).

***In vitro* bactericidal assay**

DH5α E.coli were grown to an OD_{600} of ca. 0.5, diluted 1:125 in 1xHBSS and pre-incubated with 10% mouse serum for 10 minutes at 37°C for opsonization. 10^6 *ex vivo* purified bone marrow neutrophils were resuspended in 500 µl 1xHBSS, supplemented with 10% mouse serum and incubated for 10 minutes at 37°C. 550 µl of opsonized bacteria suspension were added to granulocyte samples and incubated at 37°C on a shaking heating block for 90 minutes. Bacteria-granulocyte suspensions were serially diluted in LB medium, and plated onto LB agar plates to enumerate E.coli CFU counts.

***In vitro* LPS stimulation**

Ex vivo purified bone marrow neutrophils were incubated with 2 μg/ml LPS at 37°C for 18 hours. Supernatants were harvested and used for LEGENDplex assays to determine levels of pro-inflammatory cytokines.

Measurement of inflammatory cytokine serum levels

Serum levels of IL1-α, IL-1β, IL-6, IL-10, IL-12p70, IL-17A, IL-23, IL-27, GM-CSF, MCP-1 and TNF-α were determined using the LEGENDplex mouse inflammation panel (BioLegend) according to the manufacturer's instructions with minor modifications. Samples were analyzed on a LSRFortessa flow cytometer (BD Biosciences).

Measurement of interferon serum levels

Serum levels of IFN-α, IFN-β and IFN-γ were determined using the LEGENDplex mouse type 1/2 interferon panel (BioLegend) according to the manufacturer's instructions. Samples were analyzed on a LSRFortessa flow cytometer (BD Biosciences).

Measurement of inflammatory cytokine levels in bone marrow fluid

Levels of C5/C5a, CCL1, CCL2, CCL3, CCL4, CCL5, CCL11, CCL12, CCL17, CXCL1, CXCL2, CXCL9, CXCL10, CXCL11, CXCL12, CXCL13, G-CSF, GM-CSF, sICAM-1, IFN-γ, IL1-α, IL-1β, IL-1ra, IL-2, IL-3, IL-4, IL-5, IL-6, IL-7, IL-10, IL-12p70, IL-13, IL-16, IL-17, IL-23, IL-27, M-CSF, TIMP-1, TNF-α and TREM-1 in bone marrow fluid were determined using the ProteomeProfiler mouse cytokine array panel A (R&D Ssystems) according to the manufacturer's instructions. Protein concentration of bone marrow fluid was determined using BCA assay, and equal amounts of protein were used for cytokine detection.

RNA extraction

RNA was extracted from sorted cells using the Arcturus PicoPure RNA Isolation Kit (Thermo Fisher Scientific) according to the manufacturer's instructions including the on-column DNase digestion step.

qRT-PCR

cDNA was synthesized from RNA using the SuperScript Vilo cDNA synthesis kit (Thermo Fisher Scientific) according to the manufacturer's instructions. Oligo-dT primers were additionally added to the reaction mix. cDNA was diluted and used for qRT-PCR using SYBR Green PCR Master Mix (Thermo Fisher Scientific) on a Viia7 Real-Time PCR System (Applied Biosystems). Fold change expression values were determined with the comparative delta Ct method using *Sdha* as reference gene. Primer sequences are given in Table S3.

Single-cell *Usp22* genotyping

Single cells were sorted directly into PCR tubes containing 25 µl PCR lysis buffer (1x Buffer 1 from the Expand Long Template PCR System [Roche], 0.5 mg/ml Proteinase K) and lysed for 1h at 55°C. Proteinase K was heat-inactivated for 10 min at 95°C before 25 µl 2x PCR mix were added for the first amplification. 2 µl of the first PCR reaction were used as template for the second round of nested PCR amplification. Primer sequences are given in Table S4.

Western Blot

Cell pellets were resuspended in RIPA buffer supplemented with Complete Protease Inhibitor Cocktail (Roche), incubated for 30 minutes on ice and sonicated using a Bioruptor Plus sonicator. Samples were cleared of debris by centrifugation. Cell lysates were supplemented with Laemmli Buffer, heat-denatured, and separated by SDS-PAGE. Equal cell numbers were loaded. Proteins were transferred to PVDF membranes. Membranes were blocked in 5 % milk (in TBS-Tween) and probed with primary antibodies overnight. Primary antibodies were detected using HRP-conjugated secondary antibodies in combination with ECL substrate solution. Due to differences in their signal strengths, different exposure times were chosen for the detection of H2B and H2Bub1. Antibodies used were: anti-H2B (clone mAbcam 52484, Abcam, order no. 52484), anti-H2Bub1 (clone D11, Cell Signaling Technologies, order no. 5546S), HRP-conjugated goat-anti-mouse IgG (Thermo Fisher Scientific, order no. 32430), HRP-conjugated goat-anti-rabbit IgG (Thermo Fisher Scientific, order no. 32460). Results shown in Fig. 7A are representative of n=8 mice/genotype analyzing whole tissue lysates from various hematopoietic organs (bone marrow, spleen and thymus) or lysates of purified hematopoietic cell types.

OP9 assay

Sorted LSK (500 cells/well on 24-well plates) were plated onto irradiated OP9 feeder cells in B cell differentiation medium (MEMα + 20 % FBS + Penicillin/Streptomycin + 10 ng/ml rmFlt3L + 5 ng/ml rmIL-7) and cultured for 1.5 to 3 weeks, before cells were collected by pipetting and stained for flow cytometry.

Gamma-retroviral (GRV) transduction of LSK

The GRV backbone pMIG was a gift from William Hahn (Addgene plasmid # 9044). GRV particles were produced by transient transfection of Phoenix GP cells and concentrated using Retro-X concentrator (Takara). Sorted LSK were pre-expanded for two days, spin-infected (multiplicity of infection = 15) in the presence of polybrene and subjected to OP9 *in vitro* differentiation assays.

Transcriptome and epigenome profiling

RNA sequencing, single cell RNA sequencing, OMNI-ATAC sequencing and H2Bub1 ChIPmentation, and associated computational analysis are provided in Supplementary Methods.

Statistical analysis

Graphs were prepared using GraphPad Prism or R. Statistical details, including definition of center and precision measures, number of replicates per genotype (n) as well as statistical tests used can be found in the figure legends. Statistical significance was tested using Student's t-test, Mann-Whitney test, one-way ANOVA with Sidak's post-hoc test or two-way ANOVA with Sidak's post-hoc test.

Supplementary Materials

Table S3. Primers used for qRT-PCR.

Table S4. Primers used for *Usp22* single-cell genotyping.

Table S5. Indexing primers used for the preparation of ChIP and ATAC sequencing libraries.

Supplementary data file S1. Bulk RNA sequencing.

Supplementary data file S2. scRNA sequencing.

Supplementary data file S3. Raw data excel file.

References and Notes

1. S. Boettcher, M. G. Manz, Regulation of Inflammation- and Infection-Driven Hematopoiesis. *Trends Immunol.* **38**, 345-357 (2017).

2. B. Brook, D. J. Harbeson, C. P. Shannon, B. Cai, D. He, R. Ben-Othman, F. Francis, J. Huang, N. Varankovich, A. Liu, W. Bao, M. Bjerregaard-Andersen, F. Schaltz-Buchholzer, L. Sanca, C. N. Golding, K. L. Larsen, O. Levy, B. Kampmann, R. Tan, A. Charles, J. L. Wynn, F. Shann, P. Aaby, C. S. Benn, S. J. Tebbutt, T. R. Kollmann, N. Amenyogbe, BCG vaccination-induced emergency granulopoiesis provides rapid protection from neonatal sepsis. *Sci Transl Med* **12** (2020), doi:10.1126/scitranslmed.aax4517.

3. M. A. G. Essers, S. Offner, W. E. Blanco-Bose, Z. Waibler, U. Kalinke, M. A. Duchosal, A. Trumpp, IFNα activates dormant haematopoietic stem cells in vivo. *Nature* **458**, 904-908 (2009).

4. M. T. Baldridge, K. Y. King, N. C. Boles, D. C. Weksberg, M. A. Goodell, Quiescent haematopoietic stem cells are activated by IFN-γ in response to chronic infection. *Nature* **465**, 793-797 (2010).

5. H. Takizawa, K. Fritsch, L. V. Kovtonyuk, Y. Saito, C. Yakkala, K. Jacobs, A. K. Ahuja, M. Lopes, A. Hausmann, W.-D. Hardt, Á. Gomariz, C. Nombela-Arrieta, M. G. Manz, Pathogen-Induced TLR4-TRIF Innate Immune Signaling in Hematopoietic Stem Cells Promotes Proliferation but Reduces Competitive Fitness. *Cell Stem Cell* **21**, 225–240.e5 (2017).

6. Y. Ueda, M. Kondo, G. Kelsoe, Inflammation and the reciprocal production of granulocytes and lymphocytes in bone marrow. *J. Exp. Med.* **201**, 1771–1780 (2005).

7. A. Burberry, M. Y. Zeng, L. Ding, I. Wicks, N. Inohara, S. J. Morrison, G. Núñez, Infection mobilizes hematopoietic stem cells through cooperative NOD-like receptor and Toll-like receptor signaling. *Cell Host Microbe* **15**, 779–791 (2014).

8. Y. Nagai, K. P. Garrett, S. Ohta, U. Bahrun, T. Kouro, S. Akira, K. Takatsu, P. W. Kincade, Toll-like receptors on hematopoietic progenitor cells stimulate innate immune system replenishment. *Immunity* **24**, 801–812 (2006).

9. S. Boettcher, P. Ziegler, M. A. Schmid, H. Takizawa, N. van Rooijen, M. Kopf, M. Heikenwalder, M. G. Manz, Cutting edge: LPS-induced emergency myelopoiesis depends on TLR4-expressing nonhematopoietic cells. *J. Immunol.* **188**, 5824–5828 (2012).

10. C. Lasseaux, M.-P. Fourmaux, M. Chamaillard, L. F. Poulin, Type I interferons drive inflammasome-independent emergency monocytopoiesis during endotoxemia. *Sci. Rep.* **7**, 16935 (2017).

11. L. Romani, A. Mencacci, E. Cenci, R. Spaccapelo, C. Toniatti, P. Puccetti, F. Bistoni, V. Poli, Impaired neutrophil response and CD4+ T helper cell 1 development in interleukin 6-deficient mice infected with Candida albicans. *J. Exp. Med.* **183**, 1345–1355 (1996).

12. B. Zhu, Y. Zheng, A.-D. Pham, S. S. Mandal, H. Erdjument-Bromage, P. Tempst, D. Reinberg, Monoubiquitination of Human Histone H2B: The Factors Involved and Their Roles in HOX Gene Regulation. *Mol. Cell* **20**, 601–611 (2005).

13. N. Minsky, E. Shema, Y. Field, M. Schuster, E. Segal, M. Oren, Monoubiquitinated H2B is associated with the transcribed region of highly expressed genes in human cells. *Nat. Cell Biol.* **10**, 483–488 (2008).

14. G. J. Fonseca, G. Thillainadesan, A. F. Yousef, J. N. Ablack, K. L. Mossman, J. Torchia, J. S. Mymryk, Adenovirus Evasion of Interferon-Mediated Innate Immunity by Direct Antagonism of a Cellular Histone Posttranslational Modification. *Cell Host Microbe* **11**, 597–606 (2012).

15. X.-Y. Zhang, M. Varthi, S. M. Sykes, C. Phillips, C. Warzecha, W. Zhu, A. Wyce, A. W. Thorne, S. L. Berger, S. B. McMahon, The Putative Cancer Stem Cell Marker USP22 Is a Subunit of the Human SAGA Complex Required for Activated Transcription and Cell-Cycle Progression, *Mol. Cell* **29**. 102–111 (2008).

16. Y. Zhao, G. Lang, S. Ito, J. Bonnet, E. Metzger, S. Sawatsubashi, E. Suzuki, X. Le Guezennec, H. G. Stunnenberg, A. Krasnov, S. G. Georgieva, R. Schüle, K.-I. Takeyama, S. Kato, L. Tora, D. Devys, A TFTC/STAGA Module Mediates Histone H2A and H2B Deubiquitination, Coactivates Nuclear Receptors, and Counteracts Heterochromatin Silencing. *Mol. Cell* **29**, 92–101 (2008).

17. J. de Boer, A. Williams, G. Skavdis, N. Harker, M. Coles, M. Tolaini, T. Norton, K. Williams, K. Roderick, A. J. Potocnik, D. Kioussis, Transgenic mice with hematopoietic and lymphoid specific expression of Cre. *Eur. J. Immunol.* **33**, 314–325 (2003).

18. S. Boettcher, R. C. Gerosa, R. Radpour, J. Bauer, F. Ampenberger, M. Heikenwalder, M. Kopf, M. G. Manz, Endothelial cells translate pathogen signals into G-CSF-driven emergency granulopoiesis. *Blood* **124**, 1393–1403 (2014).

19. K. Busch, K. Klapproth, M. Barile, M. Flossdorf, T. Holland-Letz, S. M. Schlenner, M. Reth, T. Höfer, H.-R. Rodewald, Fundamental properties of unperturbed haematopoiesis from stem cells in vivo. *Nature* **518**, 542–546 (2015).

20. T. Nakano, H. Kodama, T. Honjo, Generation of lymphohematopoietic cells from embryonic stem cells in culture. *Science* **265**, 1098–1101 (1994).

21. S. K. Cho, T. D. Webber, J. R. Carlyle, T. Nakano, S. M. Lewis, J. C. Zúñiga-Pflücker, Functional characterization of B lymphocytes generated in vitro from embryonic stem cells. *Proc. Natl. Acad. Sci. U.S.A.* **96**, 9797–9802 (1999).

22. C. Maudet, S. Levallois, O. Disson, M. Lecuit, Innate immune responses to Listeria in vivo. *Curr. Opin. Microbiol.* **59**, 95–101 (2021).

23. Y. Ueda, K. Yang, S. J. Foster, M. Kondo, G. Kelsoe, Inflammation controls B lymphopoiesis by regulating chemokine CXCL12 expression. *J. Exp. Med.* **199**, 47–58 (2004).

24. H. Nagaoka, G. Gonzalez-Aseguinolaza, M. Tsuji, M. C. Nussenzweig, Immunization and infection change the number of recombination activating gene (RAG)-expressing B cells in the periphery by altering immature lymphocyte production. *J. Exp. Med.* **191**, 2113–2120 (2000).

25. Q. Lin, C. Dong, M. D. Cooper, Impairment of T and B cell development by treatment with a type I interferon. *J. Exp. Med.* **187**, 79–87 (1998).

26. R. R. Hardy, C. E. Carmack, S. A. Shinton, J. D. Kemp, K. Hayakawa, Resolution and characterization of pro-B and pre-pro-B cell stages in normal mouse bone marrow. *J. Exp. Med.* **173**, 1213–1225 (1991).

27. M. Vallespinós, D. Fernández, L. Rodríguez, J. Alvaro-Blanco, E. Baena, M. Ortiz, D. Dukovska, D. Martínez, A. Rojas, M. R. Campanero, I. Moreno de Alborán, B Lymphocyte Commitment Program Is Driven by the Proto-Oncogene c-myc. *J. Immunol.* **186**, 6726–6736 (2011).

28. S. Mostafavi, H. Yoshida, D. Moodley, H. LeBoité, K. Rothamel, T. Raj, C. J. Ye, N. Chevrier, S.-Y. Zhang, T. Feng, M. Lee, J.-L. Casanova, J. D. Clark, M. Hegen, J.-B. Telliez, N. Hacohen, P. L. De Jager, A. Regev, D. Mathis, C. Benoist, T. I. G. P. Consortium, Parsing the Interferon Transcriptional Network and Its Disease Associations. *Cell* **164**, 564–578 (2016).

29. D. Aran, A. P. Looney, L. Liu, E. Wu, V. Fong, A. Hsu, S. Chak, R. P. Naikawadi, P. J. Wolters, A. R. Abate, A. J. Butte, M. Bhattacharya, Reference-based analysis of lung single-cell sequencing reveals a transitional profibrotic macrophage. *Nat. Immunol.* **20**, 163–172 (2019).

30. J. S. Herman, Sagar, D. Grün, FateID infers cell fate bias in multipotent progenitors from single-cell RNA-seq data. *Nat. Methods* **15**, 379–386 (2018).

31. K. Street, D. Risso, R. B. Fletcher, D. Das, J. Ngai, N. Yosef, E. Purdom, S. Dudoit, Slingshot: cell lineage and pseudotime inference for single-cell transcriptomics. *BMC Genomics* **19**, 477 (2018).

32. A. E. Rodriguez-Fraticelli, S. L. Wolock, C. S. Weinreb, R. Panero, S. H. Patel, M. Jankovic, J. Sun, R. A. Calogero, A. M. Klein, F. D. Camargo, Clonal analysis of lineage fate in native haematopoiesis. *Nature* **553**, 212-216 (2018).

33. E. M. Pietras, D. Reynaud, Y.-A. Kang, D. Carlin, F. J. Calero-Nieto, A. D. Leavitt, J. M. Stuart, B. Göttgens, E. Passegué, Functionally Distinct Subsets of Lineage-Biased Multipotent Progenitors Control Blood Production in Normal and Regenerative Conditions, *Cell Stem Cell* **17**, 35–46 (2015).

34. T. Calandra, T. Roger, Macrophage migration inhibitory factor: a regulator of innate immunity. *Nat. Rev. Immunol.* **3**, 791–800 (2003).

35. R. De, S. Sarkar, S. Mazumder, S. Debsharma, A. A. Siddiqui, S. J. Saha, C. Banerjee, S. Nag, D. Saha, S. Pramanik, U. Bandyopadhyay, Macrophage migration inhibitory factor regulates mitochondrial dynamics and cell growth of human cancer cell lines through CD74-NF-κB signaling. *J. Biol. Chem.* **293**, 19740–19760 (2018).

36. M.-D. Filippi, S. Ghaffari, Mitochondria in the maintenance of hematopoietic stem cells: new perspectives and opportunities. *Blood* **133**, 1943–1952 (2019).

37. L. Papa, M. Djedaini, R. Hoffman, Mitochondrial Role in Stemness and Differentiation of Hematopoietic Stem Cells. *Stem Cells Int.* **2019**, 4067162 (2019).

38. N. Vannini, M. Girotra, O. Naveiras, G. Nikitin, V. Campos, S. Giger, A. Roch, J. Auwerx, M. P. Lutolf, Specification of haematopoietic stem cell fate via modulation of mitochondrial activity. *Nat. Commun.* **7**, 13125 (2016).

39. S. Yalcin, D. Marinkovic, S. K. Mungamuri, X. Zhang, W. Tong, R. Sellers, S. Ghaffari, ROS-mediated amplification of AKT/mTOR signalling pathway leads to myeloproliferative syndrome in Foxo3(-/-) mice. *EMBO J.* **29**, 4118–4131 (2010).

40. C. L. Bigarella, R. Liang, S. Ghaffari, Stem cells and the impact of ROS signaling. *Development* **141**, 4206–4218 (2014).

41. E. Shema, I. Tirosh, Y. Aylon, J. Huang, C. Ye, N. Moskovits, N. Raver-Shapira, N. Minsky, J. Pirngruber, G. Tarcic, P. Hublarova, L. Moyal, M. Gana-Weisz, Y. Shiloh, Y. Yarden, S. A. Johnsen, B. Vojtesek, S. L. Berger, M. Oren, The histone H2B-specific ubiquitin ligase RNF20/hBRE1 acts as a putative tumor suppressor through selective regulation of gene expression. *Genes Dev.* **22**, 2664–2676 (2008).

42. F. Zhang, X. Yu, WAC, a Functional Partner of RNF20/40, Regulates Histone H2B Ubiquitination and Gene Transcription. *Mol. Cell* **41**, 384–397 (2011).

43. E. M. Pietras, C. Mirantes-Barbeito, S. Fong, D. Loeffler, L. V. Kovtonyuk, S. Zhang, R. Lakshminarasimhan, C. P. Chin, J.-M. Techner, B. Will, C. Nerlov, U. Steidl, M. G. Manz, T. Schroeder, E. Passegué, Chronic interleukin-1 exposure drives haematopoietic stem cells towards precocious myeloid differentiation at the expense of self-renewal. *Nat. Cell. Biol.* **18**, 607–618 (2016).

44. K. A. Matatall, M. Jeong, S. Chen, D. Sun, F. Chen, Q. Mo, M. Kimmel, K. Y. King, Chronic Infection Depletes Hematopoietic Stem Cells through Stress-Induced Terminal Differentiation. *Cell Rep.* **17**, 2584–2595 (2016).

45. J. Melo-Cardenas, Y. Xu, J. Wei, C. Tan, S. Kong, B. Gao, E. Montauti, G. Kirsammer, J. D. Licht, J. Yu, P. Ji, J. D. Crispino, D. Fang, USP22 deficiency leads to myeloid leukemia upon oncogenic Kras activation through a PU.1-dependent mechanism. *Blood* **132**, 423–434 (2018).

46. J. T. Cortez, E. Montauti, E. Shifrut, J. Gatchalian, Y. Zhang, O. Shaked, Y. Xu, T. L. Roth, D. R. Simeonov, Y. Zhang, S. Chen, Z. Li, J. M. Woo, J. Ho, I. A. Vogel, G. Y. Prator, Bin Zhang, Y. Lee, Z. Sun, I. Ifergan, F. Van Gool, D. C. Hargreaves, J. A. Bluestone, A. Marson, D. Fang, CRISPR screen in regulatory T cells reveals modulators of Foxp3. *Nature* **582**, 416-420 (2020).

47. C. Li, T. Irrazabal, C. C. So, M. Berru, L. Du, E. Lam, A. K. Ling, J. L. Gommerman, Q. Pan-Hammarström, A. Martin, The H2B deubiquitinase Usp22 promotes antibody class switch recombination by facilitating non- homologous end joining. *Nat. Commun.* **9**, 1–12 (2018).

48. W. Xie, S. Nagarajan, S. J. Baumgart, R. L. Kosinsky, Z. Najafova, V. Kari, M. Hennion, D. Indenbirken, S. Bonn, A. Grundhoff, F. Wegwitz, A. Mansouri, S. A. Johnsen, RNF40 regulates gene expression in an epigenetic context-dependent manner. *Genome Biol.* **18**, 32 (2017).

49. A. Shukla, S. R. Bhaumik, H2B-K123 ubiquitination stimulates RNAPII elongation independent of H3-K4 methylation. *Biochem. Biophys. Res. Commun.* **359**, 214–220 (2007).

50. T. Prenzel, Y. Begus-Nahrmann, F. Kramer, M. Hennion, C. Hsu, T. Gorsler, C. Hintermair, D. Eick, E. Kremmer, M. Simons, T. Beissbarth, S. A. Johnsen, Estrogen-Dependent Gene Transcription in Human Breast Cancer Cells Relies upon Proteasome-Dependent Monoubiquitination of Histone H2B. *Cancer Res.* **71**, 5739–5753 (2011).

51. R. Pavri, B. Zhu, G. Li, P. Trojer, S. Mandal, A. Shilatifard, D. Reinberg, Histone H2B monoubiquitination functions cooperatively with FACT to regulate elongation by RNA polymerase II. *Cell* **125**, 703–717 (2006).

52. Z. Lin, H. Yang, Q. Kong, J. Li, S.-M. Lee, B. Gao, H. Dong, J. Wei, J. Song, D. D. Zhang, D. Fang, USP22 Antagonizes p53 Transcriptional Activation by Deubiquitinating Sirt1 to Suppress Cell Apoptosis and Is Required for Mouse Embryonic Development. *Mol. Cell* **46**, 484–494 (2012).

53. S. Srinivas, T. Watanabe, C. S. Lin, C. M. William, Y. Tanabe, T. M. Jessell, F. Costantini, Cre reporter strains produced by targeted insertion of EYFP and ECFP into the ROSA26 locus. *BMC Dev. Biol.* **1**, 4 (2001).

54. M. R. Corces, A. E. Trevino, E. G. Hamilton, P. G. Greenside, N. A. Sinnott-Armstrong, S. Vesuna, A. T. Satpathy, A. J. Rubin, K. S. Montine, B. Wu, A. Kathiria, S. W. Cho, M. R. Mumbach, A. C. Carter, M. Kasowski, L. A. Orloff, V. I. Risca, A. Kundaje, P. A. Khavari, T. J. Montine, W. J. Greenleaf, H. Y. Chang, An improved ATAC-seq protocol reduces background and enables interrogation of frozen tissues. *Nat. Methods* **14**, 959–962 (2017).

55. J. D. Buenrostro, B. Wu, H. Y. Chang, W. J. Greenleaf, ATAC-seq: A Method for Assaying Chromatin Accessibility Genome-Wide. *Curr. Protoc. Mol. Biol.* **109**, 1–9 (2015).

56. C. Schmidl, A. F. Rendeiro, N. C. Sheffield, C. Bock, ChIPmentation: fast, robust, low-input ChIP-seq for histones and transcription factors. *Nat. Methods* **12**, 963–965 (2015).

57. M. Dodt, J. T. Roehr, R. Ahmed, C. Dieterich, FLEXBAR-Flexible Barcode and Adapter Processing for Next-Generation Sequencing Platforms. *Biology (Basel)* **1**, 895–905 (2012).

58. B. Langmead, S. L. Salzberg, Fast gapped-read alignment with Bowtie 2. *Nat. Methods* **9**, 357–359 (2012).

59. D. Kim, G. Pertea, C. Trapnell, H. Pimentel, R. Kelley, S. L. Salzberg, TopHat2: accurate alignment of transcriptomes in the presence of insertions, deletions and gene fusions. *Genome Biol.* **14**, R36 (2013).

60. A. Dobin, C. A. Davis, F. Schlesinger, J. Drenkow, C. Zaleski, S. Jha, P. Batut, M. Chaisson, T. R. Gingeras, STAR: ultrafast universal RNA-seq aligner. *Bioinformatics* **29**, 15–21 (2012).

61. S. Anders, P. T. Pyl, W. Huber, HTSeq--a Python framework to work with high-throughput sequencing data. *Bioinformatics* **31**, 166–169 (2015).

62. M. I. Love, W. Huber, S. Anders, Moderated estimation of fold change and dispersion for RNA-seq data with DESeq2. *Genome Biol.* **15**, 31–54 (2014).

63. Y. Zhang, T. Liu, C. A. Meyer, J. Eeckhoute, D. S. Johnson, B. E. Bernstein, C. Nusbaum, R. M. Myers, M. Brown, W. Li, X. S. Liu, Model-based analysis of ChIP-Seq (MACS). *Genome Biol.* **9**, R137 (2008).

64. F. Ramírez, D. P. Ryan, B. Grüning, V. Bhardwaj, F. Kilpert, A. S. Richter, S. Heyne, F. Dündar, T. Manke, deepTools2: a next generation web server for deep-sequencing data analysis. *Nucleic Acids Res.* **44**, W160–165 (2016).

65. A. Liberzon, C. Birger, H. Thorvaldsdóttir, M. Ghandi, J. P. Mesirov, P. Tamayo, The Molecular Signatures Database (MSigDB) hallmark gene set collection. *Cell Syst.* **1**, 417–425 (2015).

66. M. D. Young, M. J. Wakefield, G. K. Smyth, A. Oshlack, Gene ontology analysis for RNA-seq: accounting for selection bias. *Genome Biol.* **11**, R14 (2010).

67. A. Subramanian, P. Tamayo, V. K. Mootha, S. Mukherjee, B. L. Ebert, M. A. Gillette, A. Paulovich, S. L. Pomeroy, T. R. Golub, E. S. Lander, J. P. Mesirov, Gene set enrichment analysis: a knowledge-based approach for interpreting genome-wide expression profiles. *Proc. Natl. Acad. Sci. U.S.A.* **102**, 15545–15550 (2005).

68. Y. Hao, S. Hao, E. Andersen-Nissen, W. M. 3. Mauck, S. Zheng, A. Butler, M. J. Lee, A. J. Wilk, C. Darby, M. Zager, P. Hoffman, M. Stoeckius, E. Papalexi, E. P. Mimitou, J. Jain, A. Srivastava, T. Stuart, L. M. Fleming, B. Yeung, A. J. Rogers, J. M. McElrath, C. A. Blish, R. Gottardo, P. Smibert, R. Satija, Integrated analysis of multimodal single-cell data. *Cell* **184**, 3573–3587.e29 (2021).

69. R. A. Amezquita, A. T. L. Lun, E. Becht, V. J. Carey, L. N. Carpp, L. Geistlinger, F. Marini, K. Rue-Albrecht, D. Risso, C. Soneson, L. Waldron, H. Pagès, M. L. Smith, W. Huber, M. Morgan, R. Gottardo, S. C. Hicks, Orchestrating single-cell analysis with Bioconductor. *Nat. Methods* **17**, 137–145 (2020).

70. C. Hafemeister, R. Satija, Normalization and variance stabilization of single-cell RNA-seq data using regularized negative binomial regression. *Genome Biol.* **20**, 296 (2019).

71. T. S. P. Heng, M. W. Painter, The Immunological Genome Project: networks of gene expression in immune cells. *Nat. Immunol.* **9**, 1091–1094 (2008).

72. J. Choi, T. M. Baldwin, M. Wong, J. E. Bolden, K. A. Fairfax, E. C. Lucas, R. Cole, C. Biben, C. Morgan, K. A. Ramsay, A. P. Ng, M. Kauppi, L. M. Corcoran, W. Shi, N. Wilson, M. J. Wilson, W. S. Alexander, D. J. Hilton, C. A. de Graaf, Haemopedia RNA-seq: a database of gene expression during haematopoiesis in mice and humans. *Nucleic Acids Res.* **47**, D780–D785 (2019).

73. M. Morgan, L. Shepherd, AnnotationHub: Client to access AnnotationHub resources. R package version 3.2.0. (2021), doi:10.18129/B9.bioc.AnnotationHub.

74. D. Risso, K. Schwartz, G. Sherlock, S. Dudoit, GC-content normalization for RNA-Seq data, *BMC Bioinformatics* **12**, 480 (2011).

75. P.-L. Germain, A. Lun, W. Macnair, M.D. Robinson, Doublet identification in single-cell sequencing data using scDblFinder. *F1000Research* **10** (2021), doi:10.12688/f1000research.73600.1.

76. P. Angerer, L. Haghverdi, M. Büttner, F. J. Theis, C. Marr, F. Buettner, destiny: diffusion maps for large-scale single-cell data in R. *Bioinformatics* **32**, 1241–1243 (2016).

77. T. Wu, E. Hu, S. Xu, M. Chen, P. Guo, Z. Dai, T. Feng, L. Zhou, W. Tang, L. Zhan, X. Fu, S. Liu, X. Bo, G. Yu, clusterProfiler 4.0: A universal enrichment tool for interpreting omics data. *Innovation (N Y)* **2**, 100141 (2021).

Acknowledgments: We thank Katrin Busch for providing *Tie2-MeriCreMer* mice, James Di Santo for advice on NK cell phenotyping, Kurt Reifenberg, Lena Hornetz, Annalena Riedasch, Angelika Frenznick, and the team of animal caretakers (Central Animal Laboratory DKFZ) for support and expert animal husbandry, Katja Schmidt and her team (Microbiological Diagnostics Laboratory DKFZ) for expert microbiological diagnostics, the Genomics and Proteomics Core Facility (DKFZ) for providing Illumina sequencing services, Annette Kopp-Schneider (Division of Biostatistics DKFZ) and Nils Becker (Division of Theoretical Systems Biology DKFZ) for expert advice on data analysis, Joschka Hey (Division of Cancer Epigenomics DKFZ) for critical advice on ATAC sequencing experiments, Beyza Erbil, Tobias Fischer, Celine Bauer (all Division of Cellular Immunology DKFZ) and Oliver Mücke (Division of Cancer Epigenomics DKFZ) for expert technical assistance, and the Genomics Unit of the Centre for Genomic Regulation, Barcelona, for Illumina sequencing services. We are grateful to Branko Cirovic, Hans Jörg Fehling, Klaus Rajewsky, Axel Roers and Hedda Wardemann for discussions, and all members of the Rodewald laboratory for ongoing support and discussions.

Funding:

N.D. was supported by a Helmholtz Graduate School for Cancer Research fellowship (N.D.), D.B.L. by Deutsche Krebshilfe Grant 70112574, M.L. and O.D. by Institut Pasteur and Inserm core funding, H.-R.R. and T.H. by Sonderforschungsbereich (SFB) 873-B11, and H.-R.R. by the European Research Council Advanced Grant 742883, the Helmholtz I & I Initiative program, and the Leibniz program of the Deutsche Forschungsgemeinschaft.

Author contributions: N.D. conceived the study, designed and performed experiments, interpreted results, and wrote the paper, X.W. and J.M. analyzed molecular data computationally, O.D. and M.L. performed Listeria infections, C.B. and E.R.C. performed experiments, F.S. prepared scRNA-seq libraries, D.B.L. provided support for ChIP sequencing experiments, Y.B.-N., R.L.K. and S.A.J. provided *Usp22* flox mice, T.H. supervised computational biology and wrote the paper, X.W. and D.B.L. edited the paper, and H.-R.R. supervised the study, interpreted results, and wrote the paper.

Competing interests: The German Cancer Research Center filed an international patent application (PCT/EP2022/056187) related to this work. N.D. and H.-R.R. are listed as inventors. The authors have no additional competing interests.

Data and materials availability: Bulk RNA sequencing, single cell RNA sequencing, ChIP sequencing as well as ATAC sequencing data have been deposited in GEO under the following accession number: GSE212758. Scripts for the analysis of single cell RNA sequencing data are available on GitHub (https://github.com/jome1994/Analysis_of_single_cell_data_for_Usp22_project/tree/v1.0.1) and Zenodo (https://zenodo.org/record/7011238#.Y1v59y1h3GK). All data needed to evaluate the conclusions in the paper are present in the paper or the Supplementary Materials.

Figure captions:

Fig. 1. Loss of *Usp22* induces cellular hallmarks of emergency hematopoiesis. (**A**) Absolute numbers of LT-HSC (Lineage$^-$ Sca-1$^+$ Kit$^+$ (LSK) CD150$^+$ CD48$^-$) in the bone marrow of wild type and *Usp22* KO mice (n=12 mice per genotype in 4 experiments). (**B**) Cell cycle analysis of wild type and *Usp22* KO LT-HSC based on EdU incorporation (n=3-4 mice per genotype in 2 experiments). (**C**) Distribution of wild type and *Usp22* KO LT-HSC across cell cycle phases determined by scRNA-seq (n=1 mouse per genotype). (**D**+**E**) Absolute numbers of CD11b$^+$ Gr-1$^+$ myeloid cells (**D**), and B220$^+$ B cells (**E**) in the bone marrow of wild type and *Usp22* KO mice (n=12 mice per genotype in 4 experiments). (**F**) UMAP representation of scRNA-seq data of total bone marrow cells from wild type and *Usp22* KO mice (n=1 mouse per genotype; representative of 2 independent experiments). Cells are labeled by cell type (annotated by SingleR) (left panel) or genotype (right panel). (**G**) log2 fold change (FC) of the frequencies of the indicated cell types in *Usp22* KO compared to wild type bone marrow determined by scRNA-seq (n=1 mouse per genotype; experiment 2 shown in fig. S1H). Shown are the observed log2 FC values in 95% confidence intervals determined by bootstrapping. (**H**+**I**) Absolute numbers in the spleens of LT-HSC (defined as in **A**), ST-HSC (LSK CD150$^-$ CD48$^-$) and MPP (LSK CD150$^-$ CD48$^+$) (**H**), and CMP (Lineage$^-$ Sca-1$^-$ Kit$^+$ (LS$^-$K) CD16/32$^-$ CD34$^+$), GMP (LS$^-$K CD16/32$^+$ CD34$^+$) and MEP (LS$^-$K CD16/32$^-$ CD34$^-$) (**I**) from wild type and *Usp22* KO mice (n=8 mice per genotype in 2 experiments). Mean ± s.d. (**A**, **B**, **D, E, H, I**). * p<0.05; ** p<0.01; *** p<0.001; **** p<0.0001; n.s. (not significant) by unpaired, two-tailed Student's t-test.

Fig. 2. Enhanced myelopoiesis from *Usp22* KO bone marrow. (**A**) Flow cytometric analysis of wild type and *Usp22* KO bone marrow cells stained for CD11b and Gr-1 (pre-gated on single live cells). (**B**) Gr-1 median fluorescence intensity (MFI) of CD11b$^+$Gr-1$^+$ bone marrow cells (gated as shown in **A**) from wild type and *Usp22* KO mice normalized to wild type (n=12 mice per genotype in 4 experiments). (**C**) Absolute numbers of Ly6C^{low} and Ly6C^{high} monocytes (both Lineage$^-$ CD45$^+$ Ly6G$^-$ CD115$^+$), and macrophages (Lineage$^-$ CD45$^+$ Ly6G$^-$ CD115$^-$ F4/80$^+$ SSC^{low}) in the bone marrow of wild type and *Usp22* KO mice (n=6 mice per genotype in 2 experiments). (**D**) Schematic of fate mapping of LT-HSC as described in *(19)*). Tamoxifen administration leads to the heritable induction of YFP expression in LT-HSC (orange cells, middle panel). Through

differentiation, YFP-labeled cells accumulate in progenitor and mature cell compartments (right panel). (**E**) Experimental scheme for Tie2-MCM-mediated fate mapping of wild type and *Usp22* KO LT-HSC. (**F**+**G**) YFP labeling frequency of $CD11b^+$ $Ly6G^+$ granulocytes and $CD11b^+$ $Ly6C^{high}$ monocytes (n=5 mice per genotype in 1 experiment) (**F**), and early $B220^+$ $CD43^+$ and late $B220^+$ $CD43^-$ B cell progenitors (n=5 mice per genotype in 1 experiment) (**G**) in the bone marrow normalized to the labeling frequency of LT-HSC in mice described in **E**. Mean ± s.d. (**B**, **C**, **F**, **G**,). p-values, given as * $p<0.05$; ** $p<0.01$; *** $p<0.001$; **** $p<0.0001$; n.s. (not significant) (**B**, **C**) or indicated in the figures (**F**, **G**), by unpaired, two-tailed Student's t-test.

Fig. 3. *Usp22* deficiency drives enhanced myelopoiesis in a cell-intrinsic manner. (**A**) Experimental setup for the generation of mixed bone marrow chimeras. (**B**) Contribution of wild type or *Usp22* KO bone marrow cells to B cells ($B220^+$) and myeloid cells ($CD11b^+$ $Gr\text{-}1^+$) in the bone marrow of recipient mice 20-22 weeks after transplantation (n=6 mice). (**C**) Ratio of myeloid cell chimerism and B cell chimerism in the bone marrow of mixed bone marrow chimeras comparing wild type and *Usp22* KO donors (n=28-32 mice per genotype in 5 experiments). **(D)** Gr-1 MFI of the indicated donor $CD11b^+$ $Gr\text{-}1^+$ myeloid cells (gated as shown in Fig. 2A) from mixed bone marrow chimeras described in **A**. All values were normalized to $CD45.2^+$ wild type myeloid cells (n=6 mice per genotype; data representative of 1 out of 4 experiments). (**E**) Transplantation of wild type or *Usp22* KO CMP together with total bone marrow competitor cells into lethally irradiated recipients. (**F**+**G**) Relative contributions of wild type and *Usp22* KO CMP to $CD11b^+$ myeloid cells in peripheral blood over time (**F**), and in bone marrow and spleen (10 days after transplantation) (**G**) (n=5 mice per genotype; representative of 1 out of 3 experiments. (**H**) Absence of lineage markers CD11b (myeloid) and B220 (B lineage) on sorted wild type and *Usp22* KO lineage marker$^-$ $Sca\text{-}1^+$ Kit^+ (LSK) cells before *in vitro* differentiation (top panels), and CD11b versus B220 expression 3 weeks after *in vitro* differentiation (bottom panels) (representative of 4 experiments). (**I**) Relative proportions of $B220^+$ B cells and $CD11b^+$ myeloid cells (gated as shown in bottom row of **H**) 3 weeks after *in vitro* differentiation of wild type or *Usp22* KO LSK. Each dot represents the mean of 3-5 cultures from one donor mouse. Graph represents the results from 5 mice per genotype analyzed in 4 experiments. (**J**) *In vitro* differentiation (as in **H**), mixing either wild type or *Usp22* KO LSK (both $CD45.2^+$) with wild type competitor LSK ($CD45.1^+$). After 3 weeks, cells were gated for CD45.1 versus CD45.2 (see fig.

S4F), and analyzed as in **H**. (**K**) Relative proportions of $B220^+$ B cells and $CD11b^+$ myeloid cells (gated as in **J**) in cultures derived from mixed LSK (n=4 replicates from one mouse per genotype). Mean ± s.d. (**B**, **C**, **D**, **F**, **G**, **I**, **K**). * p<0.05; ** p<0.01; *** p<0.001; **** p<0.0001; n.s. (not significant) by unpaired, two-tailed Student's t-test (**B**, **C**, **F**, **G**, **I**, **K**) or one-way ANOVA with Sidak's post-hoc test (**D**).

Fig. 4. *Usp22* deficiency enhances anti-bacterial innate immunity. (**A**) Quantification of *Listeria monocytogenes* CFU in blood, spleen, liver and brain of wild type and *Usp22* KO mice three days post-infection (n=13 mice per genotype in 2 experiments). Data points at 10^0 represent mice for which we did not detect any bacteria. (**B**) Flow cytometric assessment of the phagocytic activity of *ex vivo* purified bone marrow neutrophilic granulocytes ($Ly6G^+$) derived from wild type and *Usp22* KO mice incubated for two hours with fluorescently labeled (pHrodo red) *E. coli* particles. (**C**) pHrodo median fluorescence intensity (MFI) of bone marrow neutrophilic granulocytes from wild type and *Usp22* KO mice incubated with fluorescent *E. coli* particles described in **B** (n=2 replicates from 2 mice per genotype; data shown are from 1 out of 2 experiments). (**D**) E.coli CFU counts in co-cultures of DH5α E.coli cells with wild type or *Usp22* KO neutrophils normalized to the input number of bacteria (dashed line). The bacteria-only control (w/o Gran) is an estimate for uninhibited bacterial growth during the culture period (n=5-7 mice per genotype in 2 experiments). (**E**) TNF-α concentration in the supernatant of *ex vivo* purified wild type or *Usp22* KO bone marrow neutrophils cultured in the presence or absence of LPS. Concentrations were normalized to those of unstimulated wild type neutrophils (n=5 mice per genotype in 3 experiments). Median ± interquartile range (**A**), mean ± s.d. (**C**-**E**). * p<0.05; ** p<0.01; *** p<0.001; **** p<0.0001; n.s. (not significant) by unpaired, two-tailed Mann-Whitney test (**A**), two-way ANOVA with Sidak's post-hoc test (**C**, **E**), or one-way ANOVA with Sidak's post-hoc test (**D**).

Fig. 5. Loss of *Usp22* enhances inflammatory gene expression in HSPC. (**A**) Volcano plot showing log2 fold change (FC) in expression and the associated -log10 p-value of individual genes (dots) in *Usp22*-deficient LSK based on RNA sequencing. Significantly differentially expressed genes (DEG) (p<0.05, FC ≥ 1.5 or FC ≤ 1/1.5) are highlighted in orange. (**B**) GO term enrichment analysis of DEG upregulated in *Usp22* KO versus wild type LSK. (**C**) Heatmap showing the

expression of genes differentially expressed between wild type and *Usp22* KO LSK (n=3 mice per genotype) within selected GO terms identified in **B.** (**D**) Experimental setup of RNA sequencing of LSK isolated from mixed bone marrow chimeras. $CD45.2^+$ wild type (top panel) or $CD45.2^+$ *Usp22* KO (bottom panel) bone marrow cells were each transplanted together with $CD45.1^+$ wild type bone marrow cells into lethally irradiated $CD45.1^+/CD45.2^+$ recipient mice (n=4-5 mice per genotype). 8-9 weeks after transplantation, transcriptomes of *Usp22* KO and wild type LSK retrieved from the same host were compared by RNA sequencing. To control for transcriptome changes caused by the different CD45 allotypes of the analyzed cell populations, $CD45.2^+$ wild type and $CD45.1^+$ wild type LSK isolated from the same recipient were analyzed in parallel (see fig. S7C,D). (**E**) Expression of genes differentially expressed between *Usp22* KO and wild type LSK isolated from the same host (bottom panel of **D**) (n=4 LSK samples per genotype) (for gene list, see also Supplementary data file S1). (**F**) Gene set enrichment analysis (GSEA) plots comparing *Usp22* KO and wild type LSK from the same recipients based on DEG shown in **A**. Enrichment of upregulated and downregulated genes shown in left and right panels, respectively.

Fig. 6. Loss of *Usp22* results in myeloid transcriptional priming. (**A**) Diffusion maps of wild type and *Usp22* KO MPP based on scRNA-seq (experiment 1 shown; experiment 2 in fig. S9A). (**B**) Transcriptome-based cell cycle distribution of wild type and *Usp22* KO MPP subsets (n=1 mouse per genotype in 1 experiment). (**C**) Expression (log2 fold change) of genes driving the enrichment of the indicated GO groups 1-13 (for GO term derivation, see fig. S13) (left panel: genes contributing to any GO group; right panel: genes contributing to the GO group "Immune processes"). Only genes with a fold change > 1.2 or < 0.83 are shown. Grey fields represent genes not contributing to the enrichment of the respective GO group.

Fig. 7. *Usp22* deficiency increases H2B monoubiquitination at ISG loci. (**A**) Western blot analysis for H2B and H2Bub1 in bone marrow LSK, and splenic B ($CD19^+B220^+$), T (both $CD4^+$ and $CD8a^+$ cells) and myeloid cells ($CD11b^+$) from wild type and *Usp22* KO mice (n=8 mice per genotype). (**B**) Volcano plot showing log2 fold change (FC) in gene body H2Bub1 levels and the associated -log10 p-value of individual genes (dots) upon *Usp22* deletion in LSK based on ChIP sequencing. Significantly differentially ubiquitinated genes (DUG) ($p<0.05$, $FC \geq 1.5$ or $FC \leq 1/1.5$) are highlighted in orange (n=2 replicates per genotype). (**C**) GO term enrichment analysis

of genes hyper-monoubiquitinated in *Usp22* KO versus wild type LSK. (**D**) Correlation between change in gene body monoubiquitination and change in mRNA expression (based on RNA sequencing data described in Fig. 5A) comparing *Usp22* KO against wild type LSK for individual genes (dots), shown for all genes (left panel), or selectively for differentially expressed genes (right panel). (**E**) Correlation between change in gene body monoubiquitination and change in mRNA expression for genes differentially expressed and ubiquitinated between wild type and *Usp22* KO LSK. ISG are highlighted in red. (**F**) H2Bub1 ChIP sequencing tracks of the *H2-Ab1* (top panel) and *Mpo* (bottom panel) loci in wild type and *Usp22* KO LSK. (**G**) Fraction of ISG *(28)* within all genes detected in RNA sequencing and H2Bub1 ChIP sequencing (black bar), and the set of genes differentially expressed and differentially ubiquitinated in *Usp22* KO LSK (red bar). p-value was determined using Fisher's exact test. (**H**) Average H2Bub1 ChIP sequencing signal across gene bodies of IFN-α target genes (top panels) and IFN-γ target genes (bottom panels) in wild type and *Usp22* KO LSK. TSS = Transcription start site; TES = Transcription end site.

Figure 1

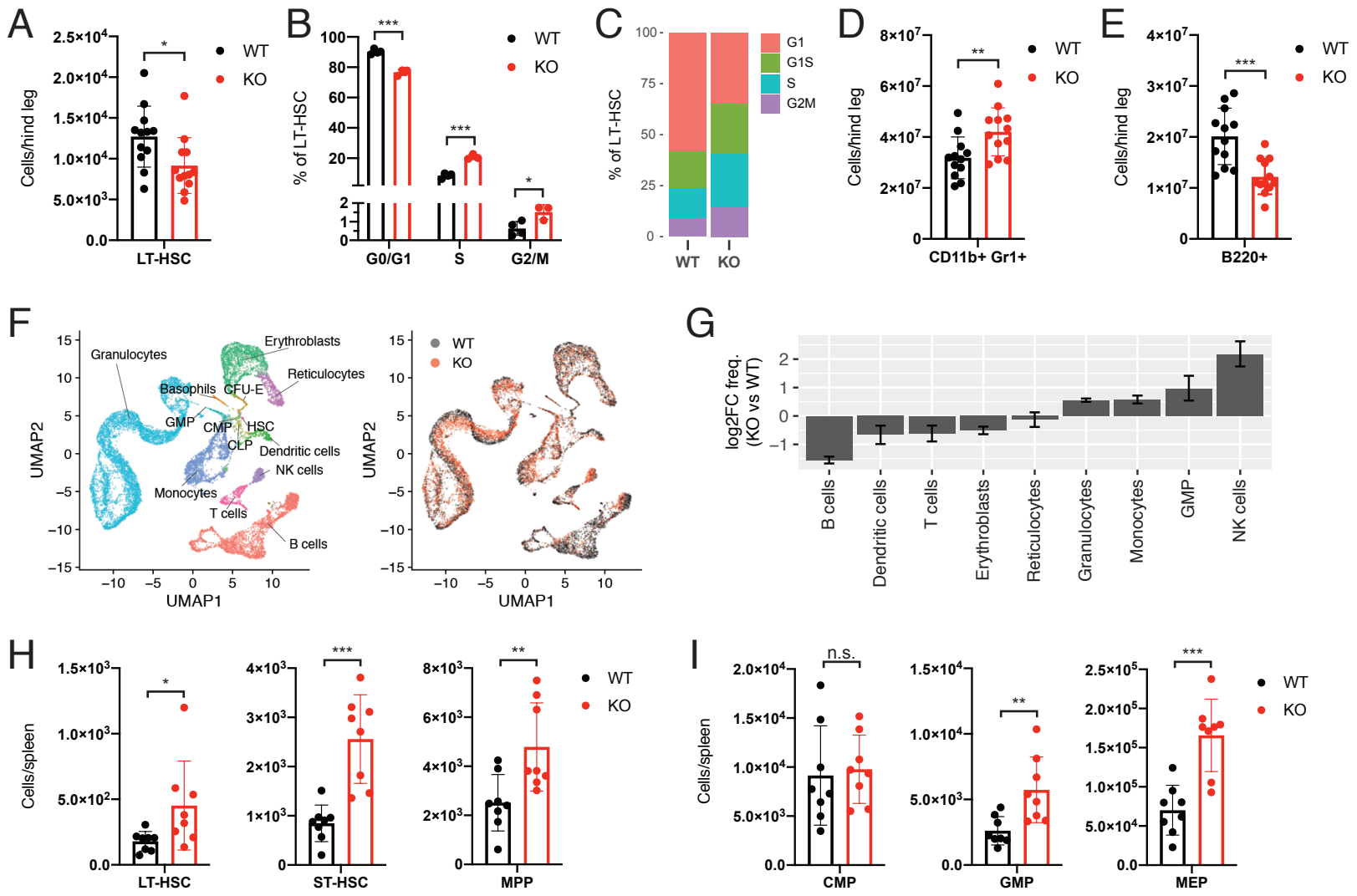
A
Cells/hind leg
WT
KO
LT-HSC
B
% of LT-HSC
G0/G1
S
G2/M
C
% of LT-HSC
G1
G1S
S
G2M
WT
KO
D
Cells/hind leg
CD11b+ Gr1+
E
Cells/hind leg
B220+
F
Granulocytes
Erythroblasts
Reticulocytes
Basophils
CFU-E
GMP
CMP
HSC
CLP
Dendritic cells
NK cells
Monocytes
T cells
B cells
UMAP1
UMAP2
G
log2FC freq. (KO vs WT)
B cells
Dendritic cells
T cells
Erythroblasts
Reticulocytes
Granulocytes
Monocytes
GMP
NK cells
H
Cells/spleen
LT-HSC
ST-HSC
MPP
I
Cells/spleen
n.s.
CMP
GMP
MEP

Figure 2

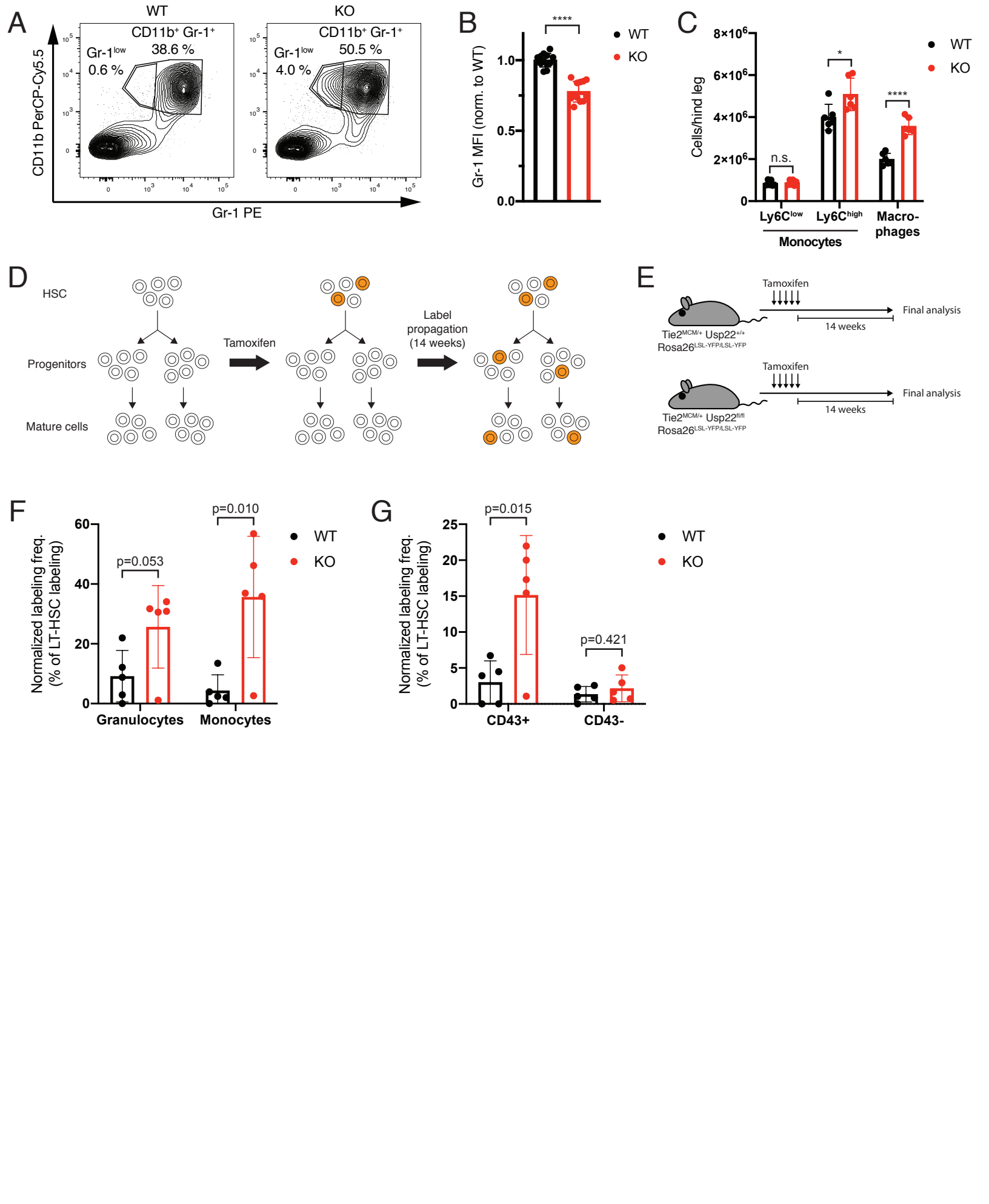
A
WT
KO
CD11b⁺ Gr-1⁺
Gr-1low
38.6 %
0.6 %
50.5 %
4.0 %
CD11b PerCP-Cy5.5
Gr-1 PE
B
****
WT
KO
Gr-1 MFI (norm. to WT)
1.0
0.5
0.0
C
8×10⁶
6×10⁶
4×10⁶
2×10⁶
0
Cells/hind leg
n.s.
*
****
Ly6Clow
Ly6Chigh
Macro-phages
Monocytes
D
HSC
Progenitors
Mature cells
Tamoxifen
Label propagation (14 weeks)
E
Tamoxifen
Final analysis
14 weeks
Tie2MCM/+ Usp22+/+ Rosa26LSL-YFP/LSL-YFP
Tie2MCM/+ Usp22fl/fl Rosa26LSL-YFP/LSL-YFP
F
p=0.010
p=0.053
Normalized labeling freq. (% of LT-HSC labeling)
60
40
20
0
Granulocytes
Monocytes
G
p=0.015
p=0.421
25
20
15
10
5
0
CD43+
CD43-

Figure 3

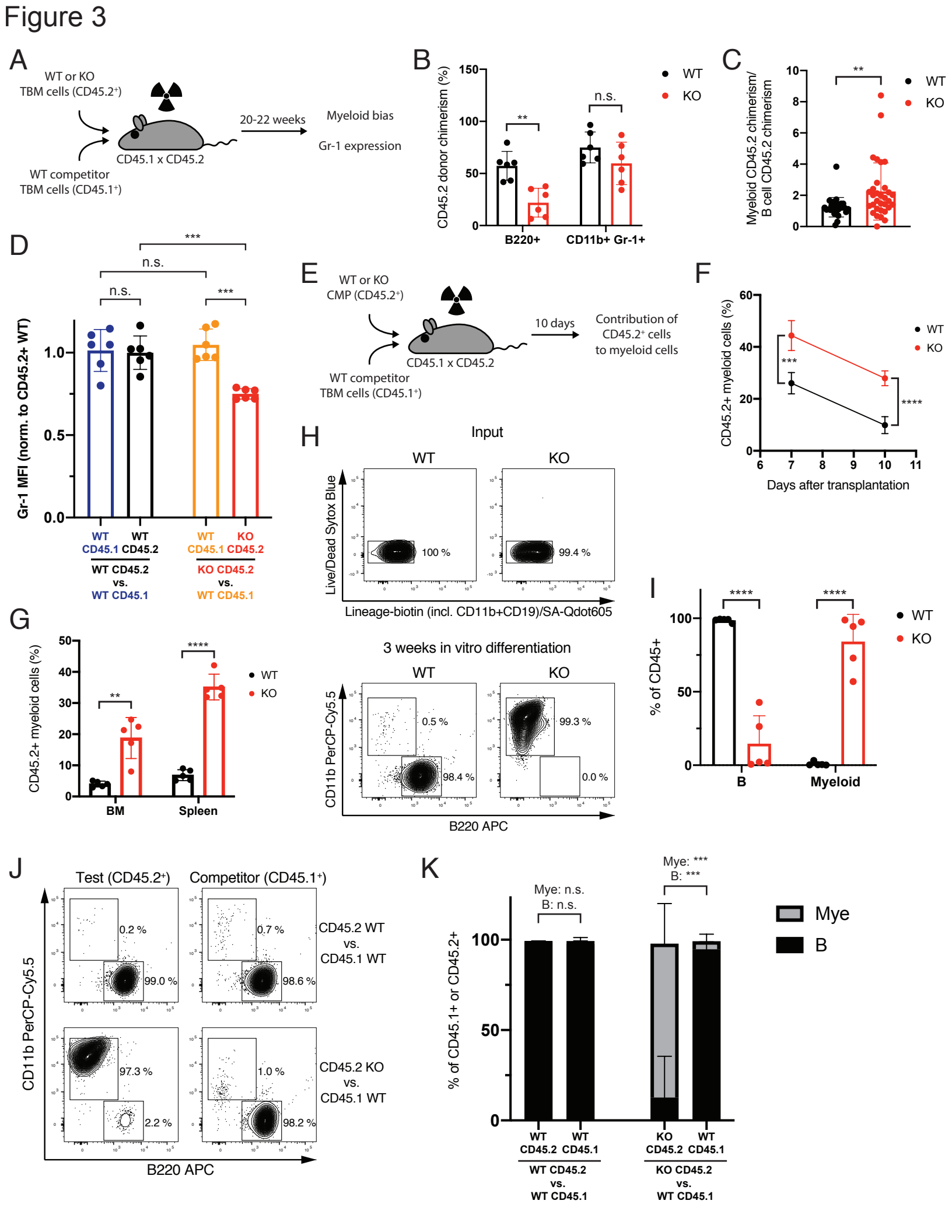
A
WT or KO
TBM cells (CD45.2+)
WT competitor
TBM cells (CD45.1+)
CD45.1 x CD45.2
20-22 weeks
Myeloid bias
Gr-1 expression
B
CD45.2 donor chimerism (%)
WT
KO
**
n.s.
B220+
CD11b+ Gr-1+
C
Myeloid CD45.2 chimerism/
B cell CD45.2 chimerism
**
WT
KO
D
***
n.s.
n.s.
***
Gr-1 MFI (norm. to CD45.2+ WT)
WT CD45.1 WT CD45.2
WT CD45.2 vs. WT CD45.1
WT CD45.1 KO CD45.2
KO CD45.2 vs. WT CD45.1
E
WT or KO
CMP (CD45.2+)
WT competitor
TBM cells (CD45.1+)
CD45.1 x CD45.2
10 days
Contribution of
CD45.2+ cells
to myeloid cells
F
CD45.2+ myeloid cells (%)
***
****
WT
KO
Days after transplantation
G
CD45.2+ myeloid cells (%)
**
****
WT
KO
BM
Spleen
H
Input
WT
KO
Live/Dead Sytox Blue
100 %
99.4 %
Lineage-biotin (incl. CD11b+CD19)/SA-Qdot605
3 weeks in vitro differentiation
WT
KO
CD11b PerCP-Cy5.5
0.5 %
98.4 %
99.3 %
0.0 %
B220 APC
I
% of CD45+
****
****
WT
KO
B
Myeloid
J
Test (CD45.2+)
Competitor (CD45.1+)
CD11b PerCP-Cy5.5
0.2 %
99.0 %
0.7 %
98.6 %
CD45.2 WT
vs.
CD45.1 WT
97.3 %
2.2 %
1.0 %
98.2 %
CD45.2 KO
vs.
CD45.1 WT
B220 APC
K
Mye: n.s.
B: n.s.
Mye: ***
B: ***
% of CD45.1+ or CD45.2+
Mye
B
WT CD45.2 WT CD45.1
WT CD45.2 vs. WT CD45.1
KO CD45.2 WT CD45.1
KO CD45.2 vs. WT CD45.1

Figure 4

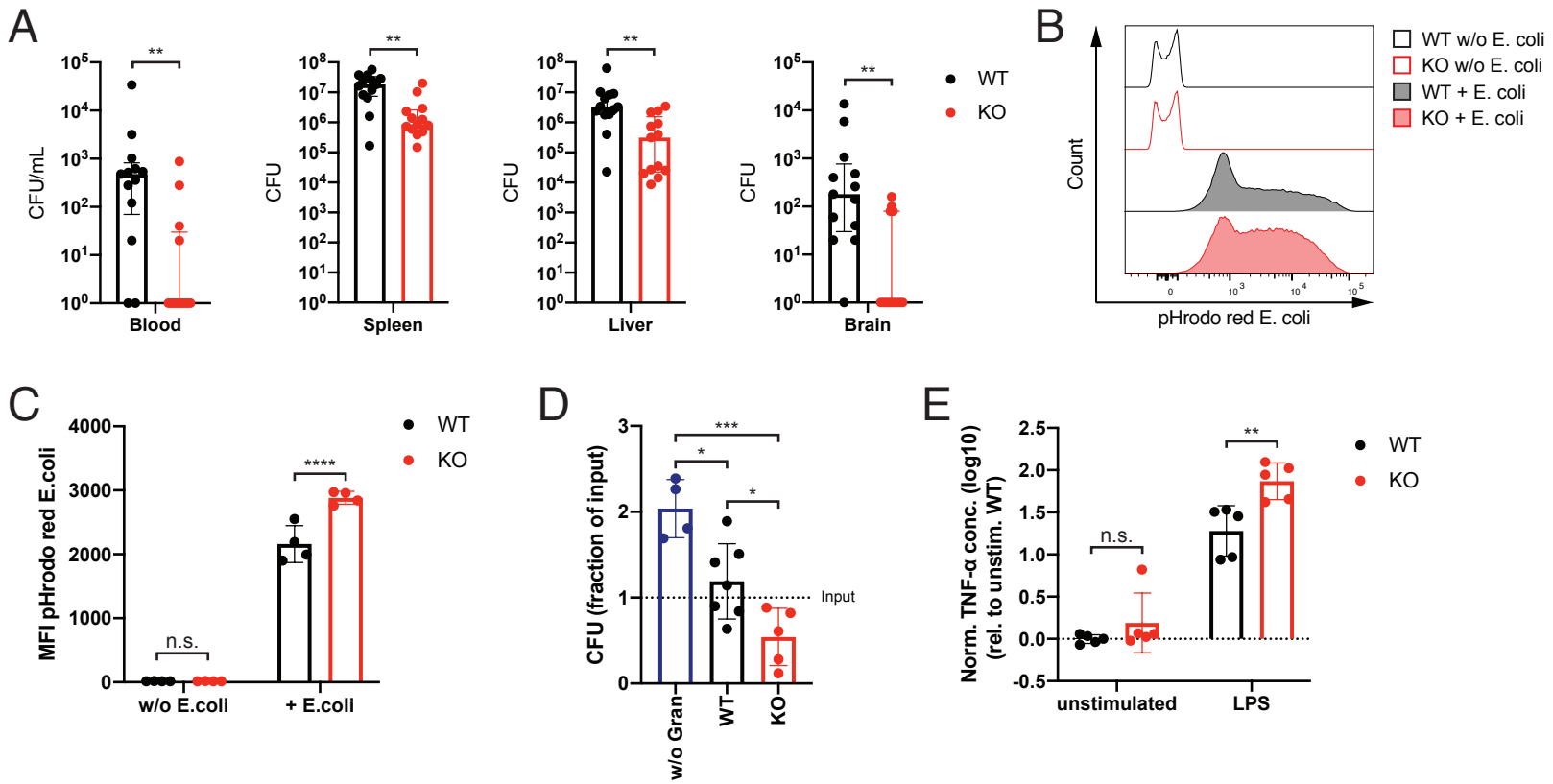
A
CFU/mL
Blood
CFU
Spleen
CFU
Liver
CFU
Brain
**
WT
KO
B
Count
pHrodo red E. coli
WT w/o E. coli
KO w/o E. coli
WT + E. coli
KO + E. coli
C
MFI pHrodo red E.coli
n.s.
****
w/o E.coli
+ E.coli
WT
KO
D
CFU (fraction of input)
***
*
*
Input
w/o Gran
WT
KO
E
Norm. TNF-α conc. (log10)
(rel. to unstim. WT)
n.s.
**
unstimulated
LPS
WT
KO

Figure 5

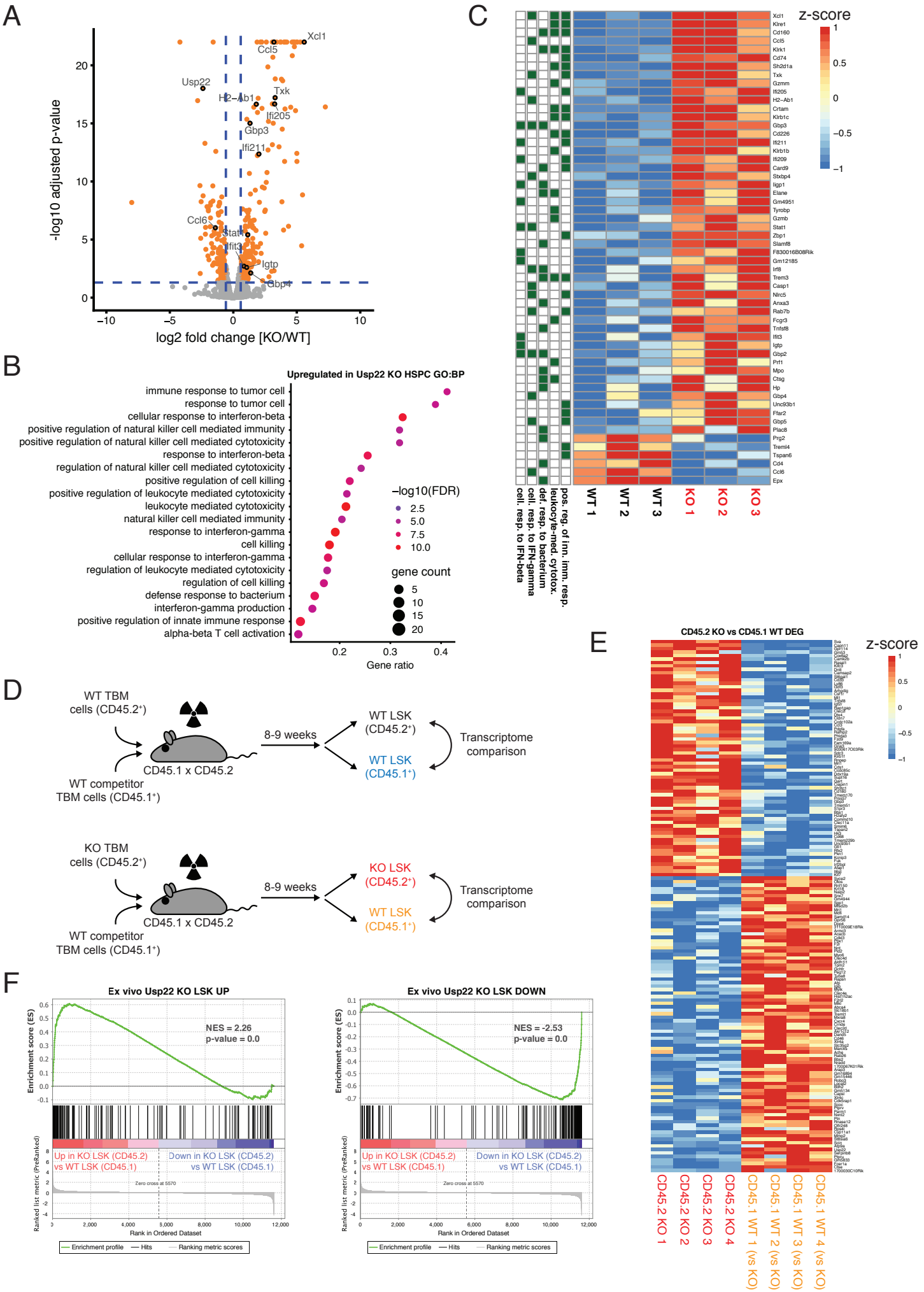
A
-log10 adjusted p-value
log2 fold change [KO/WT]
Xcl1
Ccl5
Usp22
Txk
H2−Ab1
Ifi205
Gbp3
Ifi211
Ccl6
Stat1
Ifit3
Igtp
Gbp4
B
Upregulated in Usp22 KO HSPC GO:BP
immune response to tumor cell
response to tumor cell
cellular response to interferon-beta
positive regulation of natural killer cell mediated immunity
positive regulation of natural killer cell mediated cytotoxicity
response to interferon-beta
regulation of natural killer cell mediated cytotoxicity
positive regulation of cell killing
positive regulation of leukocyte mediated cytotoxicity
leukocyte mediated cytotoxicity
natural killer cell mediated immunity
response to interferon-gamma
cell killing
cellular response to interferon-gamma
regulation of leukocyte mediated cytotoxicity
regulation of cell killing
defense response to bacterium
interferon-gamma production
positive regulation of innate immune response
alpha-beta T cell activation
−log10(FDR)
gene count
Gene ratio
C
z-score
WT 1
WT 2
WT 3
KO 1
KO 2
KO 3
pos. reg. of inn. imm. resp.
leukocyte-med. cytotox.
def. resp. to bacterium
cell. resp. to IFN-gamma
cell. resp. to IFN-beta
D
WT TBM cells (CD45.2+)
CD45.1 x CD45.2
WT competitor TBM cells (CD45.1+)
8-9 weeks
WT LSK (CD45.2+)
WT LSK (CD45.1+)
Transcriptome comparison
KO TBM cells (CD45.2+)
KO LSK (CD45.2+)
E
CD45.2 KO vs CD45.1 WT DEG
z-score
CD45.2 KO 1
CD45.2 KO 2
CD45.2 KO 3
CD45.2 KO 4
CD45.1 WT 1 (vs KO)
CD45.1 WT 2 (vs KO)
CD45.1 WT 3 (vs KO)
CD45.1 WT 4 (vs KO)
F
Ex vivo Usp22 KO LSK UP
NES = 2.26
p-value = 0.0
Ex vivo Usp22 KO LSK DOWN
NES = -2.53
p-value = 0.0
Enrichment score (ES)
Ranked list metric (PreRanked)
Up in KO LSK (CD45.2) vs WT LSK (CD45.1)
Down in KO LSK (CD45.2) vs WT LSK (CD45.1)
Zero cross at 5570
Rank in Ordered Dataset
Enrichment profile
Hits
Ranking metric scores

Figure 6

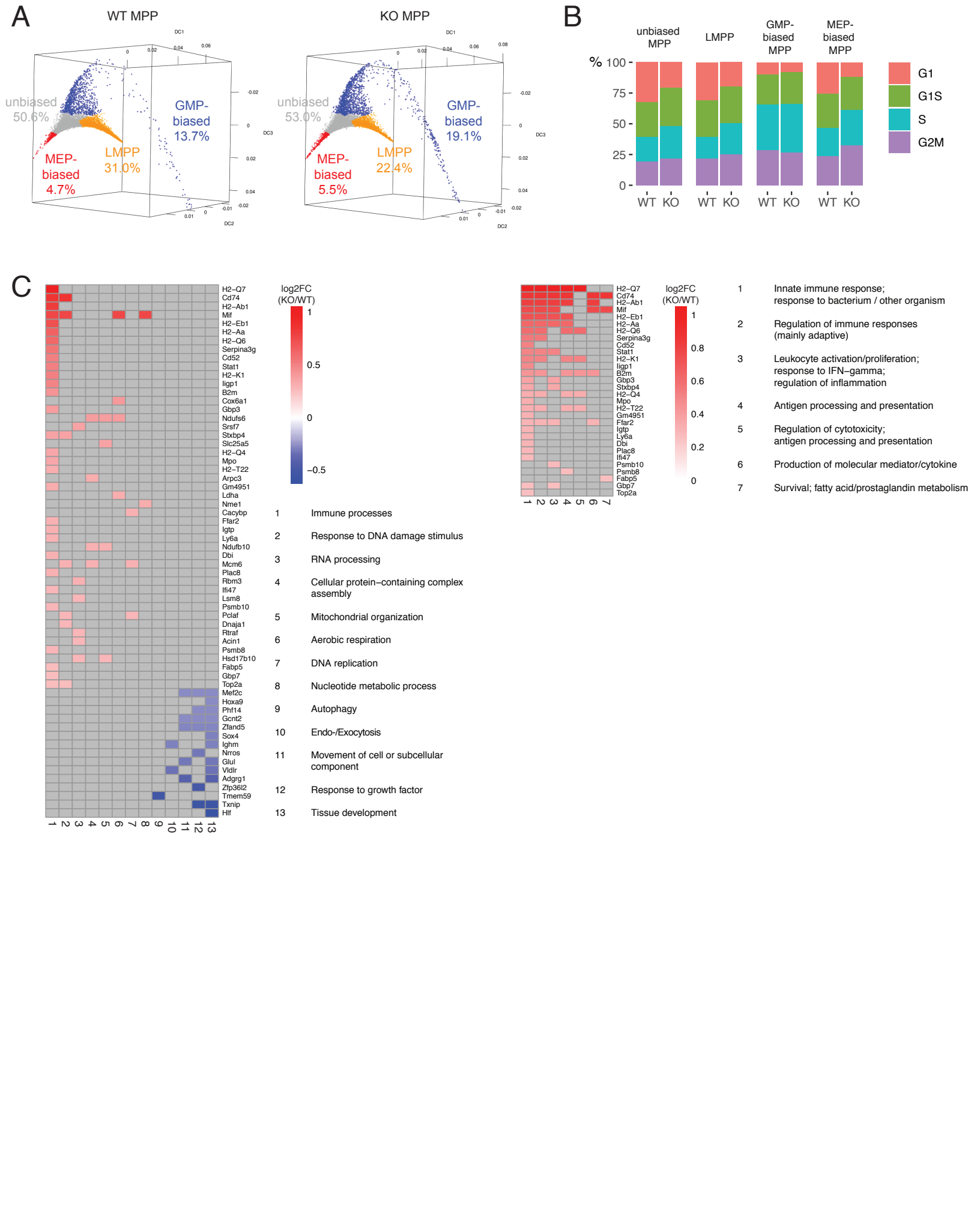
A
WT MPP
KO MPP
unbiased 50.6%
MEP-biased 4.7%
LMPP 31.0%
GMP-biased 13.7%
unbiased 53.0%
MEP-biased 5.5%
LMPP 22.4%
GMP-biased 19.1%
B
unbiased MPP
LMPP
GMP-biased MPP
MEP-biased MPP
% 100
75
50
25
0
WT KO
G1
G1S
S
G2M
C
log2FC (KO/WT)
1
0.5
0
−0.5
H2−Q7
Cd74
H2−Ab1
Mif
H2−Eb1
H2−Aa
H2−Q6
Serpina3g
Cd52
Stat1
H2−K1
Iigp1
B2m
Cox6a1
Gbp3
Ndufs6
Srsf7
Stxbp4
Slc25a5
H2−Q4
Mpo
H2−T22
Arpc3
Gm4951
Ldha
Nme1
Cacybp
Ffar2
Igtp
Ly6a
Ndufb10
Dbi
Mcm6
Plac8
Rbm3
Ifi47
Lsm8
Psmb10
Pclaf
Dnaja1
Rtraf
Acin1
Psmb8
Hsd17b10
Fabp5
Gbp7
Top2a
Mef2c
Hoxa9
Phf14
Gcnt2
Zfand5
Sox4
Ighm
Nrros
Glul
Vldlr
Adgrg1
Zfp36l2
Tmem59
Txnip
Hlf
1 2 3 4 5 6 7 8 9 10 11 12 13
1 Immune processes
2 Response to DNA damage stimulus
3 RNA processing
4 Cellular protein−containing complex assembly
5 Mitochondrial organization
6 Aerobic respiration
7 DNA replication
8 Nucleotide metabolic process
9 Autophagy
10 Endo-/Exocytosis
11 Movement of cell or subcellular component
12 Response to growth factor
13 Tissue development
log2FC (KO/WT)
1
0.8
0.6
0.4
0.2
0
1 2 3 4 5 6 7
1 Innate immune response; response to bacterium / other organism
2 Regulation of immune responses (mainly adaptive)
3 Leukocyte activation/proliferation; response to IFN−gamma; regulation of inflammation
4 Antigen processing and presentation
5 Regulation of cytotoxicity; antigen processing and presentation
6 Production of molecular mediator/cytokine
7 Survival; fatty acid/prostaglandin metabolism

Figure 7

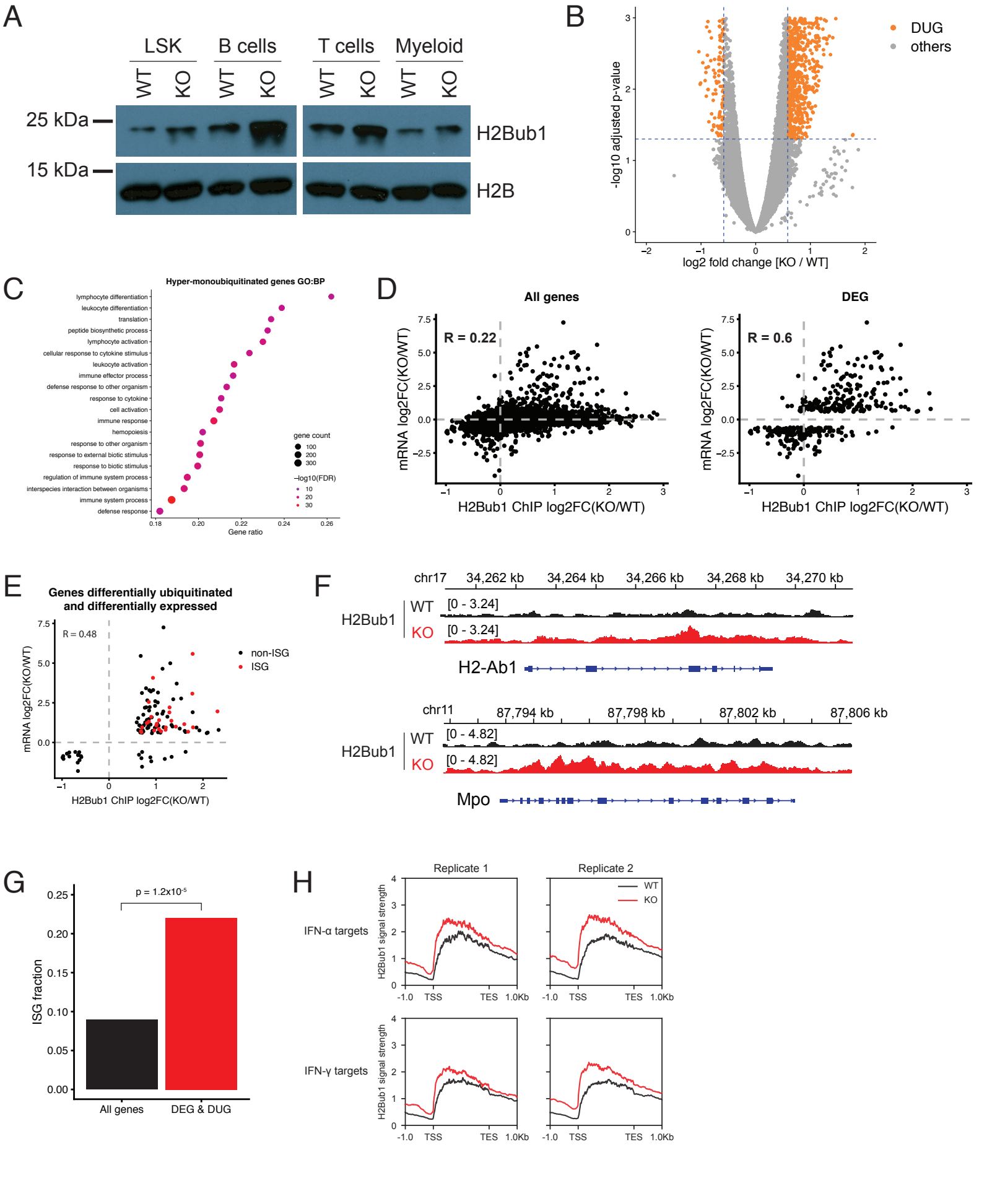
A
LSK
B cells
T cells
Myeloid
WT
KO
25 kDa
15 kDa
H2Bub1
H2B
B
DUG
others
-log10 adjusted p-value
log2 fold change [KO / WT]
C
Hyper-monoubiquitinated genes GO:BP
lymphocyte differentiation
leukocyte differentiation
translation
peptide biosynthetic process
lymphocyte activation
cellular response to cytokine stimulus
leukocyte activation
immune effector process
defense response to other organism
response to cytokine
cell activation
immune response
hemopoiesis
response to other organism
response to external biotic stimulus
response to biotic stimulus
regulation of immune system process
interspecies interaction between organisms
immune system process
defense response
gene count
−log10(FDR)
Gene ratio
D
All genes
DEG
R = 0.22
R = 0.6
mRNA log2FC(KO/WT)
H2Bub1 ChIP log2FC(KO/WT)
E
Genes differentially ubiquitinated and differentially expressed
R = 0.48
non-ISG
ISG
mRNA log2FC(KO/WT)
H2Bub1 ChIP log2FC(KO/WT)
F
chr17
34,262 kb
34,264 kb
34,266 kb
34,268 kb
34,270 kb
H2Bub1
WT
KO
[0 - 3.24]
H2-Ab1
chr11
87,794 kb
87,798 kb
87,802 kb
87,806 kb
[0 - 4.82]
Mpo
G
p = 1.2x10-5
ISG fraction
All genes
DEG & DUG
H
Replicate 1
Replicate 2
WT
KO
IFN-α targets
IFN-γ targets
H2Bub1 signal strength
-1.0
TSS
TES
1.0Kb

SUPPLEMENTARY METHODS

RNA sequencing

Equal amounts of total RNA were converted into double-stranded cDNA using the SMARTer Ultra Low Input RNA for Illumina Sequencing – HV kit according to the manufacturer's instructions. Sequencing libraries were prepared with the NEBNext ChIP-Seq Library Prep Master Mix Set for Illumina according to the manufacturer's instructions with the following modifications. 10 µl of adapter-ligated double-stranded cDNA were amplified using NEBNext Multiplex Oligos for Illumina (25 µM primers), NEBNext High-Fidelity 2x PCR Master Mix and 15 cycles of PCR. Libraries were validated using an Agilent 2200 TapeStation and a Qubit fluorometer. 50 bp single-read sequencing of pooled libraries was performed on an Illumina HiSeq 2000 v4.

Single cell RNA sequencing

FACS-purified cells (2 replicates per population and genotype isolated from age- and sex-matched mice taken from the same colony) were resuspended in PBS and processed using the Chromium System (Chromium Single Cell 3' Reagent Kits v3, 10x Genomics) according to the manufacturer's instructions (CG000183 RevA/CG000206 RevD). In brief, single cells were encapsulated into droplets and mRNA was captured with indexed beads. After reverse transcription, indexed cDNA was cleaned up and amplified with the following PCR program: 3 min at 98 °C, 13-14 x (15 s at 98 °C, 20 s at 63 °C, 1 min at 72 °C) and final extension for 3 min at 72 °C. To generate sequencing libraries, 25% of the cDNA were used as input for fragmentation, Illumina sequencing adapter ligation and indexing PCR. Indexing PCR was performed with the following program: 45s at 98 °C, 13-14 x (20 s at 98 °C, 30s s at 54 °C, 20s at 72 °C) and final extension for 1 min at 72 °C. After quality control, libraries were pooled and sequenced on Illumina HiSeq4000 and Nextseq 1000/2000 platforms using the parameters recommended by 10x Genomics.

OMNI-ATAC sequencing

OMNI-ATAC sequencing was performed as described in *(54)* with minor modifications. Briefly, 50,000 sorted LSK were lyzed and nuclei subjected to Tn5 mediated transposition for 30 minutes

at 37°C. DNA was purified using Ampure XP beads and used for indexing PCR. Sequences of the used indexing primers are given in Table S5. The number of PCR cycles was determined by qRT-PCR as described in *(55)*. Amplified libraries were purified by two-sided Ampure XP bead purification and validated on a Bioanalyzer (Agilent). 50 bp paired-end sequencing of pooled libraries was performed on an Illumina HiSeq2500.

ChIPmentation for H2Bub1

H2Bub1 ChIPmentation of LSK was performed according to *(56)* with minor modifications. Sorted LSK were subjected to cross-linking in 1 % formaldehyde (in PBS) for 10 minutes at room temperature, and cross-linking was stopped by adding glycine. Pellets of cross-linked cells were resuspended in shearing buffer (10 mM Tris-HCl pH 8, 0.1% SDS, 1 mM EDTA) supplemented with Complete Protease Inhibitor Cocktail (Roche), and chromatin was sheared to an average fragment size of 200-250 bp. DNA concentrations were assessed using a Qubit fluorometer, equal amounts of sheared chromatin were diluted in ChIPmentation dilution buffer (20 mM HEPES pH 8.0, 150 mM NaCl, 0.1 % SDS, 1 % Triton-X, 1 mM EDTA, 0.5 mM EGTA), and incubated with anti-H2Bub1 (clone D11, Cell Signaling Technologies, order no. 5546S) or rabbit isotype control (BioLegend, order no. 910801) antibody over night at 4°C. On the next day, pre-blocked magnetic Protein A beads were added, and samples incubated for two hours at 4°C. Bead-bound chromatin fragments were separated on a magnetic tube rack and washed before they were subjected to tagmentation. Chromatin fragments bound to magnetic beads were resuspended in 30 µl Tagmentation mix (14 µl H_2O, 15 µl Tagment DNA Buffer [Illumina, order no. 15027866], 1 µl Tagment DNA Enzyme [Illumina, order no. 15027865]), and incubated for 10 minutes at 37°C. Bead-bound chromatin was washed and decross-linked in elution buffer containing Proteinase K for eight hours at 56°C. Decross-linked chromatin was purified using Ampure XP beads, subjected to indexing PCR as described in the section "OMNI-ATAC sequencing" and purified again with Ampure XP beads. Purified libraries were validated on a Bioanalyzer instrument. 50 bp single-end sequencing of pooled libraries was performed on an Illumina HiSeq2500.

RNA sequencing data processing and analysis

The RNA sequencing reads were first subjected to adapter trimming and low-quality read filtering using *flexbar* (version 2.5) *(57)* with the following parameters: -u 10 -m 32 -ae RIGHT -at 2 -ao

2. Reads that were mapped to the reference sequences of rRNA, tRNA, snRNA, snoRNA, and miscRNA (available from Ensembl and RepeatMasker annotation) using *Bowtie* 2 (version 2.2.9) *(58)* with default parameters (in --end-to-end & --sensitive mode) were excluded. The remaining reads were then mapped to the mouse reference genome (mm10) using *Tophat2* (version 2.1.1) *(59)* with the parameters -N 2 --read-gap-length 2 --read-edit-dist 3 --min-anchor 6 --library-type fr-unstranded --segment-mismatches 2 --segment-length 25, or *STAR* (version 2.7.3a) *(60)* with key parameters --outFilterMismatchNmax 8 --outFilterMismatchNoverLmax 0.04 --alignIntronMin 20 --alignIntronMax 100000 --outFilterType BySJout --outFilterIntronMotifs RemoveNoncanonicalUnannotated. Reads that were mapped to multiple genomic sites were discarded in the following analysis. *HTSeq-count* (version 0.9.1) *(61)* was used to count reads mapped to annotated genes, with parameters -f bam -r pos -s no -a 10.

Differentially expressed gene analysis was performed with the R package *DESeq2* (version 1.16.0) *(62)*. In brief, size factor estimation was first conducted to normalize the data across samples, followed by dispersion estimation to account for the negative binomial distributed count data in RNA sequencing. Finally, gene expression fold changes were calculated and the significance of the gene expression difference was estimated using the Wald test. To control the false discovery rate in multiple testing, the raw p-values were adjusted using the Benjamini–Hochberg (BH) procedure. Genes with adjusted p-values less than 0.05 and fold changes over 1.5 folds were considered as differentially expressed.

ChIP sequencing data processing and analysis

The ChIP sequencing reads were first subjected to adapter trimming and low-quality read filtering using *flexbar* (version 2.5) *(57)* with the following parameters: -u 5 -m 26 -ae RIGHT -at 2 -ao 1. The trimmed reads were mapped to the mouse reference genome (mm10) using *Bowtie* 2 (version 2.2.9) *(58)* with default parameters. Reads that mapped to mitochondrial DNA or with low mapping quality (< 30) were excluded for downstream analysis. Duplicate reads due to PCR amplification of single DNA fragments during library preparation were identified using *Picard* (version 2.17.3; available at http://broadinstitute.github.io/picard) and thus removed from the downstream analysis.

To obtain the pure signal of monoubiquitinated H2B, H2Bub1 ChIP sequencing data were compared to the input data (libraries prepared from DNA of cells from replicate set 1) using the

bdgcmp command of *macs2* (version 2.1.1) *(63)* for signal fold enrichment. The resulting signal was then used for drawing signal profiles and heatmaps. To identify differentially ubiquitinated genes, we counted the deduplicated reads overlapping with gene bodies (introns included) of individual genes. *DESeq2* (version 1.16.0) *(62)* was then used for statistical comparison of the read counts obtained from wild type and *Usp22*-deficient LSK, with a procedure similar to the analysis of the RNA sequencing data. Genes with adjusted p-values less than 0.05 and fold changes over 1.5 folds were considered as differentially ubiquitinated.

ATAC sequencing data processing and analysis

The processing steps of ATAC sequencing data for read trimming, mapping and deduplication were the same as those for the ChIP sequencing data. Genome-wide chromatin accessibility was quantified using *bamCoverage* from the *deeptools* python toolkit suit (version 3.4.3) *(64)* based on the deduplicated reads. To compare data from different libraries, the accessibility signal was normalized using library scale factors. Thus, the normalized accessibility signal was used for drawing signal profiles and heatmaps. To identify genes with differential accessibility in their promoters, we counted the deduplicated reads overlapping with gene promoters (defined as a 2000-bp window centered at a gene's transcription start site). *DESeq2* (version 1.16.0) *(62)* was then used for statistical comparison of the read counts obtained from wild type and *Usp22*-deficient LSK, with a similar procedure as for analyzing the RNA sequencing data. Genes with adjusted p-values less than 0.05 and fold changes over 1.5 folds were considered as the ones with differential promoter accessibility.

GO/hallmark signature enrichment analysis

The gene symbols were mapped to GO terms/hallmark gene sets using either R packages *GO.db*, *AnnotationDbi*, and *org.Mm.e.g.db*, or based on the *MSigDB* collections*(65)*. Gene sets with at least 10 genes in background (i.e. all expressed genes) were tested for enrichment in DEG using the GOseq method provided in the R package *goseq (66)*. The raw p-values were then adjusted using the Benjamini–Hochberg (BH) procedure. Gene set enrichment analysis (GSEA) *(67)* was performed using the GSEA JAVA interface (version 4.0.3) available at https://www.gsea-msigdb.org/gsea/.

Computational analysis of single-cell RNA-sequencing data

FASTQ files were processed by 10x Genomics Cell Ranger version 3.1.0 using the reference transcriptome mm10-3.0.0. The resulting filtered feature-barcode matrices were used for analyses in R. The complete analysis workflow in R can be reproduced by running the scripts provided on GitHub.

A renv.lock file is provided to reproduce the R environment with all required packages in the used versions. During the analysis in R, single cell data were stored in two main object types: Seurat- and SingleCellExperiment object *(68, 69)*. The count matrices were processed in R using version 4.0.1 of the Seurat software. For all samples, cells with fewer than 200 detected genes were excluded and only genes that were detected in at least three cells were retained. Cells were further filtered in a sample-specific manner based on a lower and upper threshold of the number of detected genes and the percentage of counts assigned to mitochondrial transcripts. Count data of all samples were normalized using the SCTransform function *(70)* of the Seurat package. For each gene in each cell, the function computes the Pearson residual from a generalized linear model in which sequencing depth is used as a covariate. All genes with a variance of model residuals larger than 1.3 were selected for dimensionality reduction and principal component analysis (PCA) was conducted using Seurat's RunPCA function with default parameters. The number of principal components (PC) used for downstream analysis was estimated by ranking the PC based on their standard deviation and selecting the top n PC above the strong drop in standard deviation. Cells were clustered by first computing a shared-nearest-neighbor graph based on Euclidean distance between cells in PCA space (FindNeighbors function), followed by the identification of modules of the graph (FindClusters function, using the Louvain algorithm). UMAP embeddings were generated using the RunUMAP function. In some cases, the n.neighbors and min.dist parameters were adjusted to preserve the global connectivity of the cell populations.

To annotate each cell, we identified the reference cell type that had highest correlation with the cell's raw gene counts, using SingleR *(29)*. Raw bulk RNA-seq read count data of reference populations were downloaded from two databases: ImmGen (GSE109125, GSE122108; *(71)*) and Haemosphere (Haemopedia-Mouse-RNASeq_raw.txt and Haemopedia-Mouse-RNASeq_samples.txt; *(72)*). Ensemble gene IDs in the Haemosphere data set were translated to symbols using the AnnotationHub software *(73)*. Only untreated samples which were purified from total bone marrow were used. Additionally, data from T cells and NKT cells isolated from other

tissues were extracted from GSE109125 as those cell types were not available from total bone marrow. Only genes detected in all reference and single-cell data were used for the correlation analysis. The data of the reference samples were normalized by first dividing each read count by the length of the respective gene (EDASeq; *(74)*) and then multiplying it with a sample-specific factor to ensure that the normalized values of each sample sum up to 10^6. The obtained transcript per million (TPM) values were log2-transformed to allow gene selection in SingleR. Samples of populations including multiple other cell types were removed to avoid inconclusive annotations. The pruned labels returned by SingleR were used to annotate the cells.

To assign cells to a particular cell cycle phase, a two-dimensional UMAP embedding of the respective populations was computed based on sequencing-depth corrected log-transformed counts of S-phase and G2M-phase-specific genes. For this purpose, gene lists provided by the Seurat package were used. In the obtained UMAP embedding, cells were arranged in a circular shape and annotated by cell cycle phase using Seurat's CellCycleScoring function. As the boundary between G0/G1 and S-phase was very fuzzy, intermediate cells were classified as G1S-cells. Intermediate cells were defined as those cells, with a UMAP-based neighborhood (n=200) in which the smallest category (either G1 or S) made up more than 5% of the neighborhood.

To compare cell-type frequencies between wild type and *Usp22* KO, each total bone marrow sample (one WT and one KO) was initially processed individually until potential doublets were removed using the scDblFinder package *(75)*. Then both samples were pooled and re-processed including normalization. Cells were annotated by SingleR and labels were adjusted by summarizing some categories or adjusting them to cluster boundaries. Adjustment to cluster boundaries was performed to improve separation between NK and T cells and between B cells and CLP (CLP in the B cell cluster were relabeled as B cells). For each condition, cells were sampled with replacement. The sample size was set equal to the original number of cells in the respective sample. The log2(fold-changes) of the observed cell-type frequencies were computed between the conditions. Sampling and computation of fold-changes were repeated 10,000 times and 95% confidence intervals were estimated.

Branching events were resolved in MPP using diffusion modelling: Until stated, data of both conditions were processed separately. Cells were annotated by SingleR to identify MPP with GMP-, CLP- or MEP-like transcriptome. Effects of cell cycle were regressed out during normalization and the Pearson residuals of genes with a residual variance larger than 1.3 were used

for the next step. Additionally, few cells annotated as NK, T, preT, proB, basophil, eosinophil, dendritic cell or monocyte were excluded as it was important to include only cells forming a continuum of transcriptomic states. The fateBias function of the FateID package *(30)* was used to classify each retained MPP as LMPP, GMP- or MEP-biased starting from the most mature cells identified by SingleR annotation. In each iteration, the fateBias function internally trained a random forest model to classify cells based on expression values of lineage-specific genes. The training started with the annotated endpoint cells and iteratively assigned more undifferentiated cells to a branch. Genes that were most important for classification during the first 25% of all iterations were extracted from the trained models using the impGenes function. Genes important during later iterations were not used as it can be expected that classification accuracy decreases for cells that show less lineage-bias. Only genes selected as lineage markers in both conditions were selected for the next steps. Selected genes (n=45) contained many known markers of lineage specification like Mpo, Flt3, Dntt and Elane (same genes were used for the analysis of the replicated experiment). After the extraction of lineage-specific genes, data of both conditions were pooled and normalization was repeated without regressing out effects of cell cycle. Sequencing-depth corrected, log-transformed counts of lineage-specific genes were used for computing a diffusion map using the destiny package *(76)*. After removing few extreme cells on diffusion component (DC) 3 (annotated as Pre-CFU-E), the diffusion map was recomputed. The first three dimensions resolved all branching events of interest. Clustering was performed on the cells' first three diffusion coordinates. The MEP-biased branch, which had the smallest distance to MPP that were annotated as HSC by SingleR, was defined as root cluster whereas the branches with GMP-biased MPP and LMPP were defined as tip clusters. Trajectories were inferred from the root to the tip clusters applying the Slingshot Software *(31)* with default parameters. Cells which were – according to pseudo-time – located between the tip of the MEP branch and the center of HSC-like cells, were labeled as MEP-biased cells. The remaining cells were labeled as GMP-biased MPP or LMPP if they were only assigned to one of the two trajectories. Cells assigned to both trajectories were annotated as unbiased MPP.

To perform gene expression comparisons between MPP of both conditions while accounting for differential cell distributions along the differentiation trajectories, MPP were sampled in the following manner: Only wild type cells whose first nearest neighbor in the diffusion embedding was a KO cell were retained in the embedding. KO cells were retained if they were the

first neighbor of at least one WT cell and could also be sampled multiple times if they were a direct neighbor of more than one WT cell. 81.8% of the retained KO cells were only sampled once and only 1.5% were sampled more than two times with a maximum of four. This suggests that results were unlikely to be distorted by strong overrepresentation of individual cells. To assess the effect of sampling, results were always compared to results obtained when using the original populations. Overall, the results were comparable.

To analyze differential expression of genes indicating lineage priming, those were first identified by a Wilcoxon test: GMP-biased MPP or LMPP were compared to all other MPP subsets and only genes that were significantly differentially expressed in all pairwise comparisons were defined as LMPP or GMP-bias signature genes (adjusted p-value < 0.05). Genes were filtered by a fold change threshold of 1.25 as subtle but significant changes should also be considered. For each cell, module scores were computed for both signatures using Seurat's AddModuleScore function. The same signatures were used to analyse the replicated experiment.

Gene Set Enrichment Analysis (GSEA) was conducted using the gseGO function of the ClusterProfiler package *(77)*. Significant (adjusted p-value < 0.05) Gene Ontology (GO) terms of the category "Biological Processes" were grouped based on overlaps of the corresponding gene sets: Two GO terms were added to the same group if their corresponding gene sets had a Jaccard similarity of at least 0.3. Afterwards, only GO groups with more than 70 leading edge genes in total were retained and manually annotated. For LT-HSC a threshold of 100 leading edge genes was used. Those thresholds were adjusted in the replicated experiment to retain GO groups of comparable size. The GO group containing terms related to immunity was further subdivided using hierarchical clustering based on Jaccard similarity. For GSEA of MPP, the MPP populations which were corrected for differential cell distribution along differentiation trajectories were used. For LT-HSC, the complete wild type and KO population was used.

MPP subset-specific differential expression analyses between genotypes were done using a Wilcoxon test implemented in Seurat's FindMarkers function. To reduce shrinkage of fold changes in genes with low average expression, the default pseudo-count of 1 was lowered to 0.1. Genes with a log2(fold change) > 0.25 or < -0.25 and an adjusted p-value < 0.05 were considered differentially expressed. Before plotting significant changes, fold changes of DEG were recomputed with a pseudo-count of 1 to ensure consistency with other plots.

Figure S1

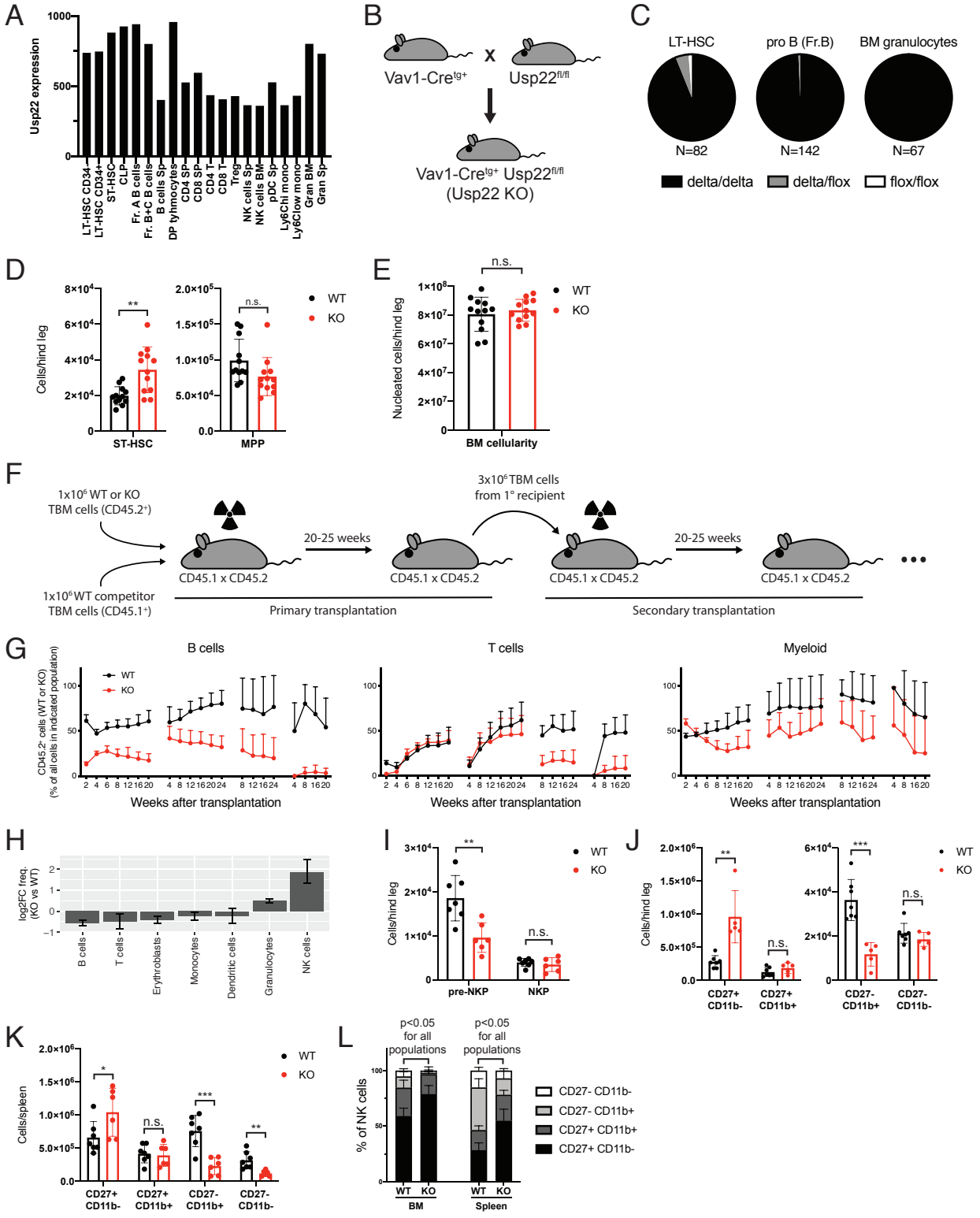

Fig. S1. Characterization of hematopoiesis in *Usp22* KO mice. (**A**) *Usp22* mRNA expression levels in the indicated hematopoietic cell types based on publicly available bulk RNA sequencing

data from the Immgen database *(71)*. (**B**) Transgenic Vav1-Cre mice were crossed with mice carrying a floxed *Usp22* allele to obtain mice with pan-hematopoietic *Usp22* deficiency (*Usp22* KO). (**C**) *Usp22* genotype of individual cells within the indicated cell populations isolated from *Usp22* KO mice determined by single-cell PCR (n=67-142 cells) (delta/delta = KO). (**D**) Absolute cell numbers of ST-HSC and MPP in the bone marrow of wild type and *Usp22* KO mice (n=12 mice per genotype in 4 experiments). (**E**) Absolute numbers of nucleated cells in the bone marrow of wild type and *Usp22* KO mice (n=12 mice per genotype in 4 experiments). (**F**) Experimental setup for serial competitive bone marrow transplantation. Wild type or *Usp22* KO bone marrow cells (both CD45.2) were transplanted together with wild type competitor bone marrow cells (CD45.1) into irradiated recipients (CD45.1/CD45.2). (**G**) Contribution of wild type or *Usp22* KO bone marrow cells (both CD45.2) to all (CD45.1 + CD45.2 + CD45.1/CD45.2) B cells ($CD19^+$), T cells ($CD3^+$) and myeloid cells ($CD11b^+$) in peripheral blood in serial competitive bone marrow transplantation experiments described in **F**. (**H**) log2 fold change (FC) of the frequencies of the indicated cell types in the bone marrow of *Usp22* KO compared to wild type mice determined by scRNA-seq (experiment 2). Shown are the observed log2 FC values in 95% confidence intervals determined by bootstrapping. (**I**) Absolute numbers of pre-NK progenitor (pre-NKP; Lin^- $CD45^+$ $CD27^+$ $CD244^+$ $CD127^+$ $Flt3^-$ $CD122^-$) and NK progenitor cells (NKP; Lin^- $CD45^+$ $CD27^+$ $CD244^+$ $CD127^+$ $Flt3^-$ $CD122^+$) in the bone marrow of wild type and *Usp22* KO mice (n=6-7 mice per genotype in 3 experiments). (**J**+**K**) Absolute numbers of the indicated NK cell populations (pre-gated as Lin^- $CD45^+$ $NK1.1^+$ $NKp46^+$ $DX5^+$) in the bone marrow (**J**) (n=5-7 mice per genotype in 3 experiments) and spleen (**K**) (n=6-7 mice per genotype in 3 experiments) of wild type and *Usp22* KO mice. (**L**) Relative frequencies of the indicated NK cell populations within total NK cells (n=8-9 mice per genotype in 4 experiments). Mean ± s.d. (**D**, **E**, **G**, **I**-**L**). * $p<0.05$; ** $p<0.01$; *** $p<0.001$; **** $p<0.0001$; n.s. (not significant) by unpaired, two-tailed Student's t-test.

Figure S2

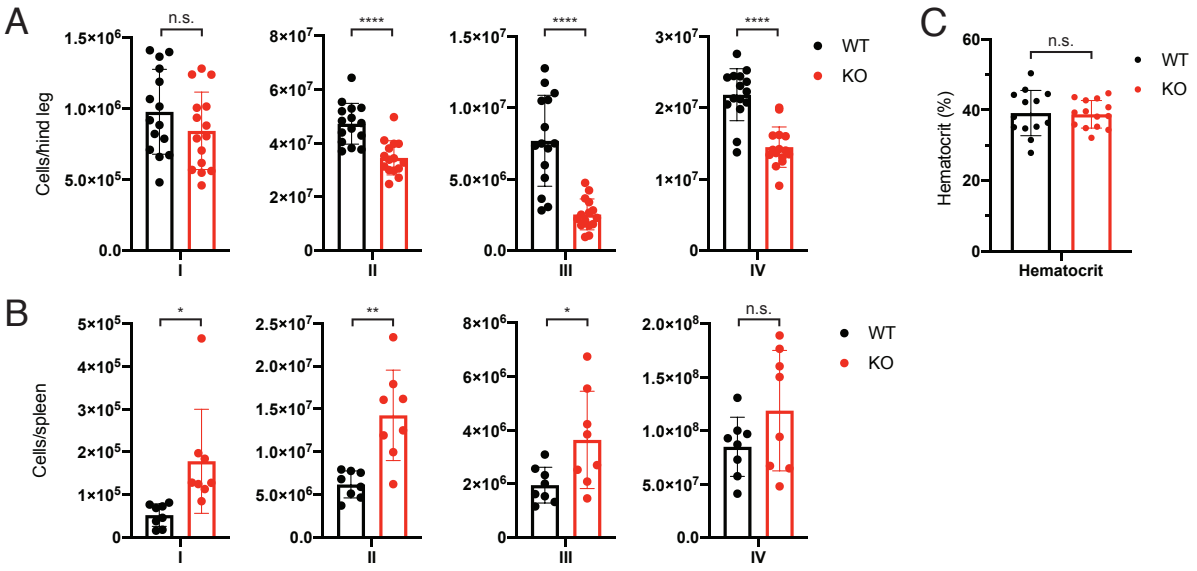

Fig. S2. Erythropoiesis and extramedullary hematopoiesis in *Usp22*-deficient mice. (**A**+**B**) Absolute numbers of proerythroblasts (I) ($CD71^{high}$ $Ter119^{low}$), basophilic erythroblasts (II) ($CD71^{high}$ $Ter119^{high}$), late basophilic and chromatophilic erythroblasts (III) ($CD71^{int}$ $Ter119^{high}$), and orthochromatophilic erythroblasts (IV) ($CD71^{neg}$ $Ter119^{high}$) in the bone marrow (n=15 mice per genotype in 5 experiments) (**A**) and in the spleen (n=8 mice per genotype in 2 experiments) (**B**) of wild type and *Usp22* KO mice. (**C**) Hematocrit of wild type and *Usp22* KO mice (n=13-14 mice per genotype). Mean ± s.d. (**A**-**C**). * $p<0.05$; ** $p<0.01$; *** $p<0.001$; **** $p<0.0001$; n.s. (not significant) by unpaired, two-tailed Student's t-test.

Figure S3

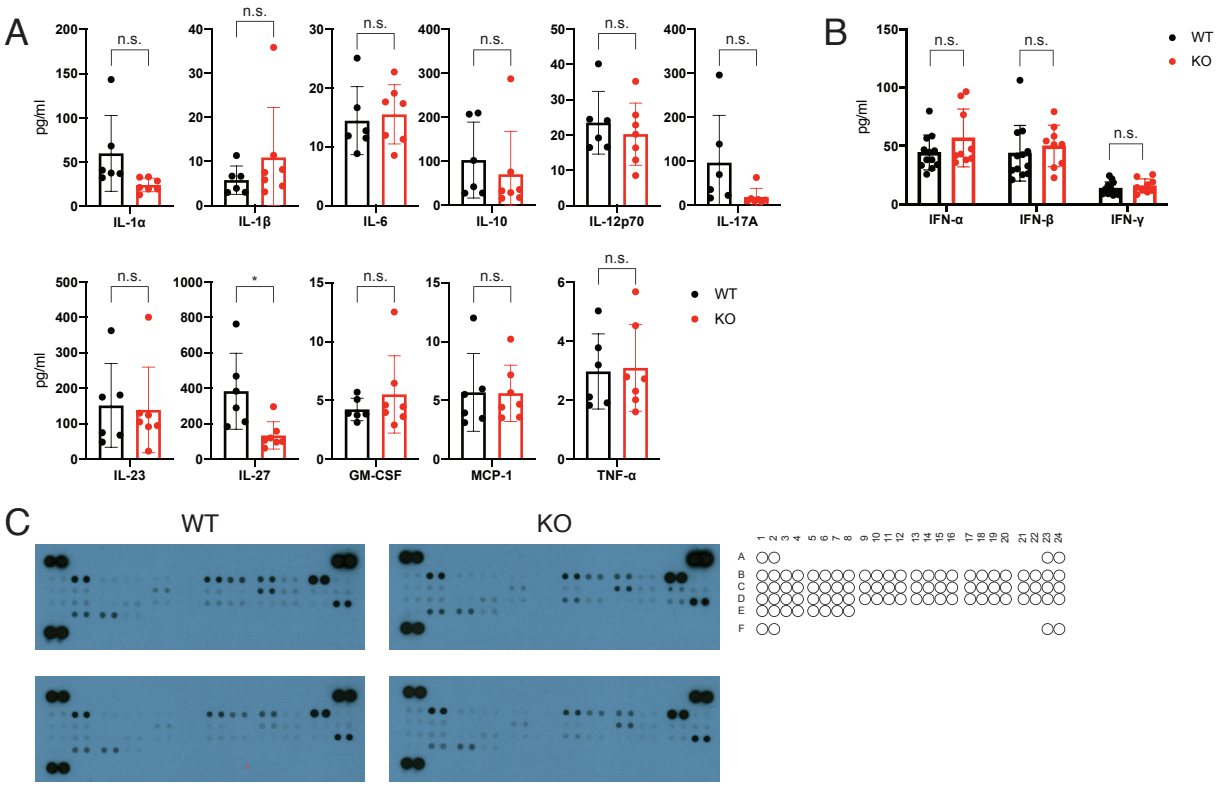

Fig. S3. Emergency hematopoiesis in *Usp22* KO mice in the absence of inflammation. (**A**) Serum concentrations of the indicated cytokines in wild type and *Usp22* KO mice (n=6-7 mice per genotype). (**B**) Serum concentrations of IFN-α, IFN-β and IFN-γ in wild type and *Usp22* KO mice (n=9-12 mice per genotype). (**C**) Detection of inflammatory cytokines (using cytokine array) in the bone marrow supernatant of wild type and *Usp22* KO mice. Analyte coordinates: A1+2: Reference spot, A23+24: Reference spot, B1+2: CXCL13, B3+4: C5/C5a, B5+6: G-CSF, B7+8: GM-CSF, B9+10: CCL1, B11+12: CCL11, B13+14: sICAM-1, B15+16: IFN-γ, B17+18: IL-1α, B19+20: IL-1β, B21+22: IL-1ra, B23+24: IL-2, C1+2: IL-3, C3+4: IL-4, C5+6: IL-5, C7+8: IL-6, C9+10: IL-7, C11+12: IL-10, C13+14: IL-13, C15+16: IL-12p70, C17+18: IL-16, C19+20: IL-17, C21+22: IL-23, C23+24: IL-27, D1+2: CXCL10, D3+4: CXCL11, D5+6: CXCL1, D7+8: M-CSF, D9+10: CCL2, D11+12: CCL12, D13+14: CXCL9, D15+16: CCL3, D17+18: CCL4, D19+20: CXCL2, D21+22: CCL5, D23+24: CXCL12, E1+2: CCL17, E3+4: TIMP-1, E5+6: TNF-α, E7+8: TREM-1, F1+2: Reference spot, F23+24: Negative control. Mean ± s.d. (**A**, **B**). * p<0.05; ** p<0.01; *** p<0.001; **** p<0.0001; n.s. (not significant) by unpaired, two-tailed Student's t-test.

Figure S4

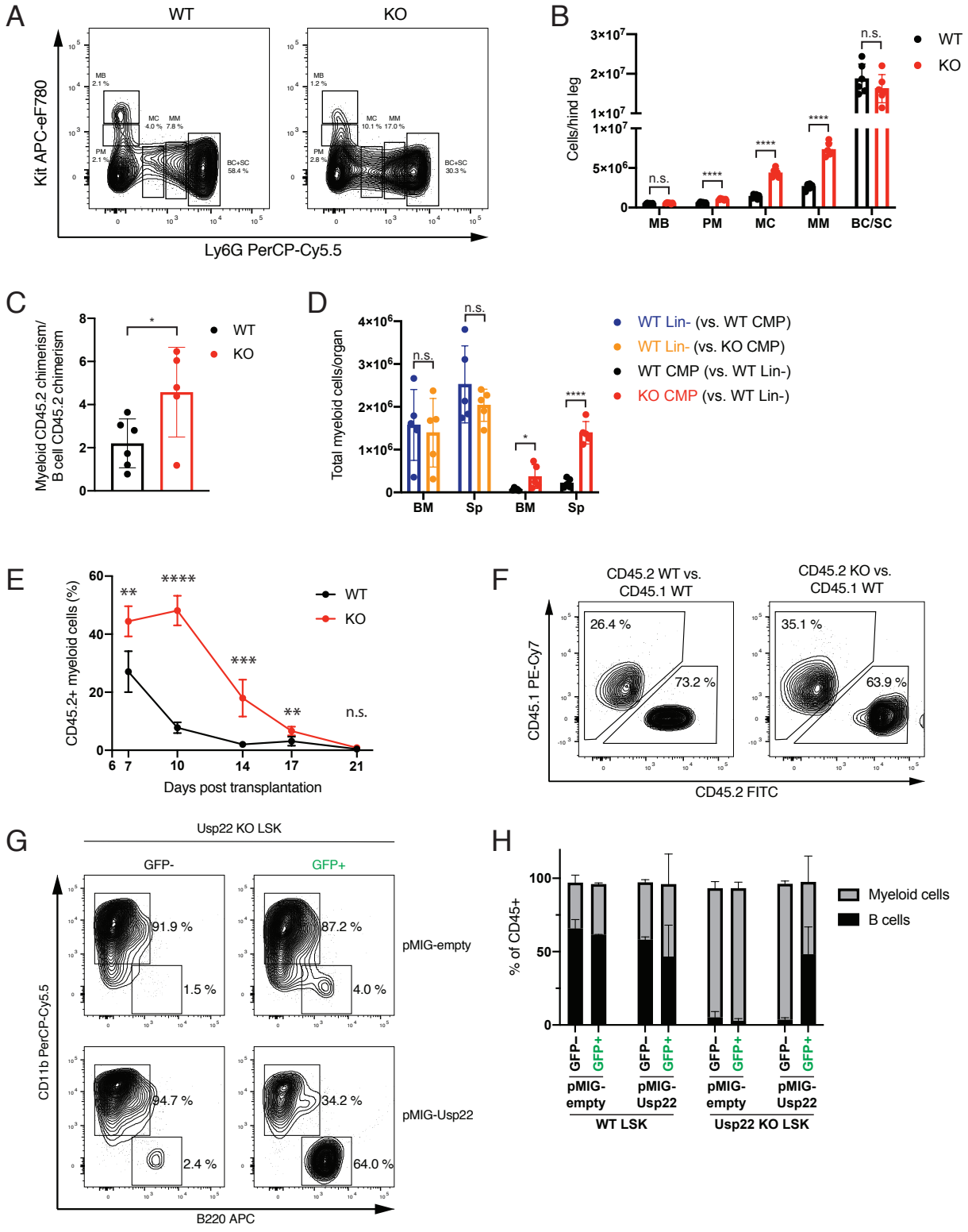

Fig. S4. Cell-autonomous emergency myelopoiesis in *Usp22*-defcient mice. (**A**) Expression of Kit and Ly6G resolves stages of myelopoiesis, i.e. myeloblasts (MB), promyelocytes (PM),

myelocytes (MC), metamyelocytes (MM), band cells (BC) and segmented cells (SC) in wild type and *Usp22* KO bone marrow cells. Cells were pre-gated on lineage marker (B220, CD4, CD8 and Ter119)$^-$ cells, and via a non-MEP gate. (**B**) Absolute numbers of MB, PM, MC, MM and BC/SC (gated as in **A**) in the bone marrow of wild type and *Usp22* KO mice (n=6 mice per genotype in 2 experiments). (**C**) Ratio of myeloid over B cell chimerism in the bone marrow of mice transplanted with wild type or *Usp22*-deficient HSC together with wild type competitor bone marrow cells (n=5-6 from 1 experiment). (**D**) Total myeloid output per organ of the indicated progenitors 10 days after transplantation (n=5 mice per genotype, data representative of 1 out of 3 experiments). (**E**) Contributions of wild type and *Usp22* KO CMP to CD11b$^+$ myeloid cells in peripheral blood of recipient mice followed-up for 21 days (n=5 mice per genotype from 1 experiment). (**F**) Gating of CD45.1$^+$ and CD45.2$^+$ cells in competitive OP9 cultures (Fig. 3J,K). (**G**) CD11b and B220 expression in cells differentiated *in vitro* for 1.5 weeks from *Usp22* KO LSK transduced with the indicated vectors. Transduced cells were identified based on GFP expression. (**H**) Relative proportions of B220$^+$ B cells and CD11b$^+$ myeloid cells (gated as in **G**) within cells differentiated for 1.5 weeks *in vitro* from wild type and *Usp22* KO LSK transduced with the indicated gamma-retroviral expression vectors (n=3 replicates from 1 experiment). The partial myeloid cell production in these experiments also from wild type progenitors presumably results from the cellular pre-expansion conditions required for viral transduction prior to the differentiation assay. Mean ± s.d. (**B**, **C**, **D**, **E**, **H**). * $p<0.05$; ** $p<0.01$; *** $p<0.001$; **** $p<0.0001$; n.s. (not significant) by unpaired, two-tailed Student's t-test.

Figure S5

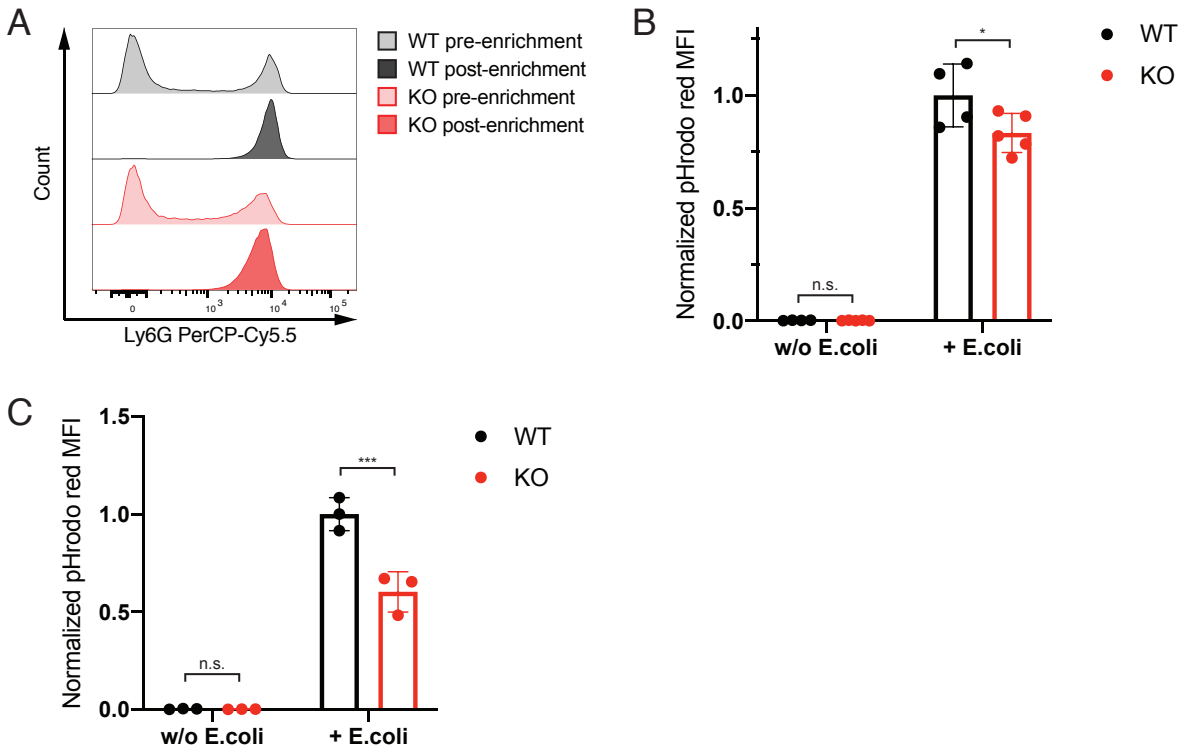

Fig. S5. Ly6G expression on granulocytes and phagocytosis by macrophages. (**A**) Flow cytometric analysis of Ly6G expression levels in *ex vivo* purified bone marrow neutrophilic granulocytes from wild type and *Usp22* KO mice. (**B**) pHrodo median fluorescence intensity (MFI) of bone marrow-derived macrophages from wild type and *Usp22* KO mice incubated with fluorescent *E. coli* particles *in vitro* for 2 hours (n=4-5 mice per genotype in 2 experiments). (**C**) pHrodo median fluorescence intensity (MFI) of peritoneal macrophages from wild type and *Usp22* KO mice incubated with fluorescent *E. coli* particles *in vitro* for 2 hours (n=3 mice per genotype in 2 experiments). Mean ± s.d. (**B**, **C**).* p<0.05; ** p<0.01; *** p<0.001; **** p<0.0001; n.s. (not significant) by two-way ANOVA with Sidak's post-hoc test.

Figure S6

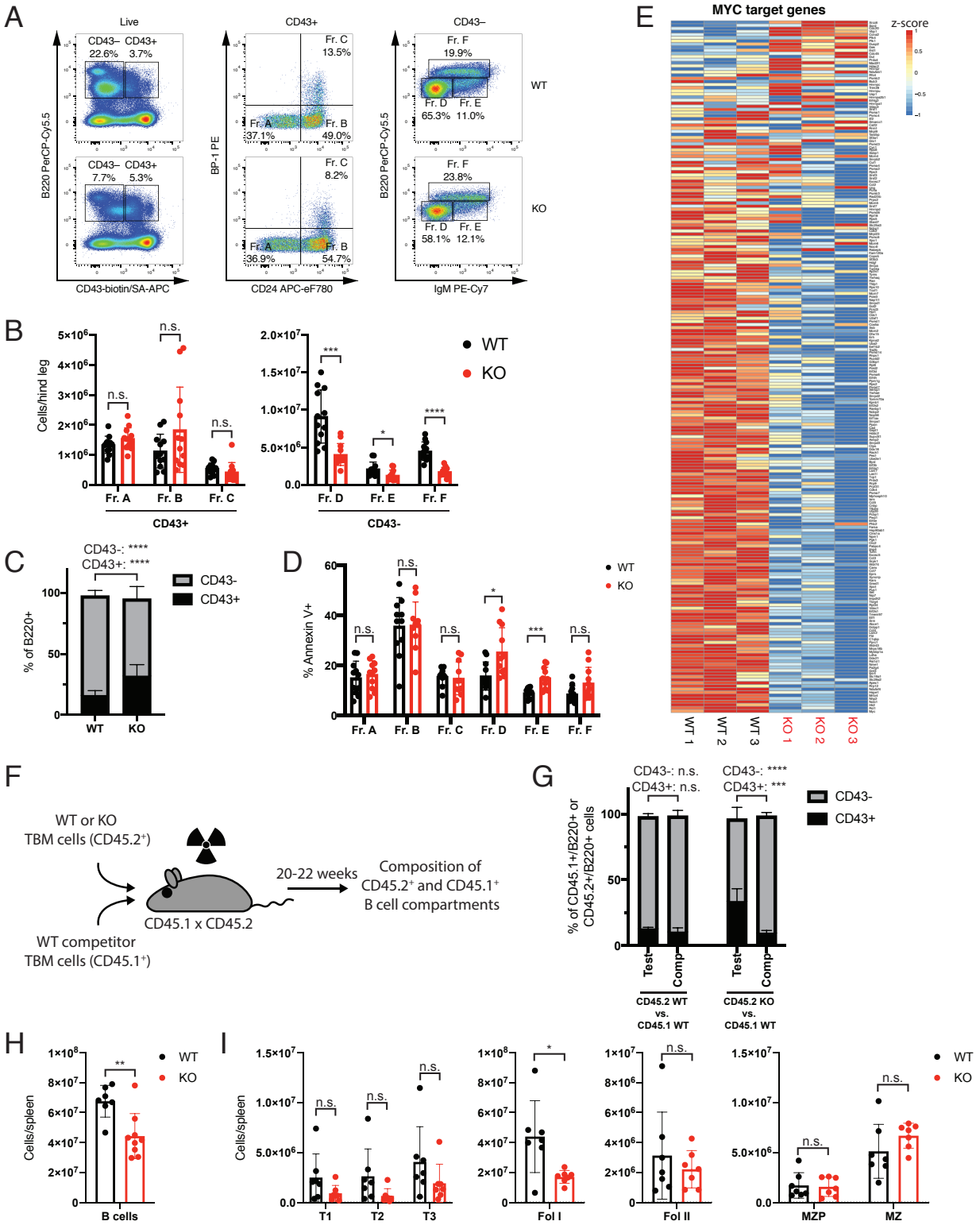

Fig. S6. Impaired B cell development in *Usp22* KO mice. (**A**) Flow cytometric analysis of B cell development in wild type and *Usp22* KO bone marrow. (**B**) Absolute numbers of the indicated

B cell progenitor populations (gated as shown in **A**) in the bone marrow of wild type and *Usp22* KO mice (n=12 mice per genotype in 4 experiments). (**C**) Relative proportions of early $CD43^+$ and late $CD43^-$ B cell progenitors within the $B220^+$ population of wild type and *Usp22* KO mice (n=12 mice per genotype in 4 experiments). (**D**) Percentage of Annexin V^+ apoptotic cells within the indicated B cell progenitor populations of wild type and *Usp22* KO mice (n=11 mice per genotype in 4 experiments). (**E**) Heatmap showing the expression of *Myc* target genes in primary pre-B cells (fraction C) from wild type and *Usp22* KO mice. (**F**) Experimental setup for the generation of mixed bone marrow chimeras. (**G**) Relative proportions of early $CD43^+$ and late $CD43^-$ B cell progenitors within the $B220^+$ population of $CD45.2^+$ test and $CD45.1^+$ competitor cells in mixed bone marrow chimeras (n=6 mice per genotype, data representative for 1 out of 2 experiments). (**H**) Absolute numbers of $CD19^+$ $B220^+$ splenic B cells in wild type and *Usp22* KO mice (n=7-9 mice per genotype in 3 experiments). (**I**) Absolute numbers of the indicated splenic B cell subsets in wild type and *Usp22* KO mice (n=7 mice per genotype in 3 experiments). Mean ± s.d. (**B**-**D**, **G**-**I**).* $p<0.05$; ** $p<0.01$; *** $p<0.001$; **** $p<0.0001$; n.s. (not significant) by unpaired, two-tailed Student's t-test.

Figure S7

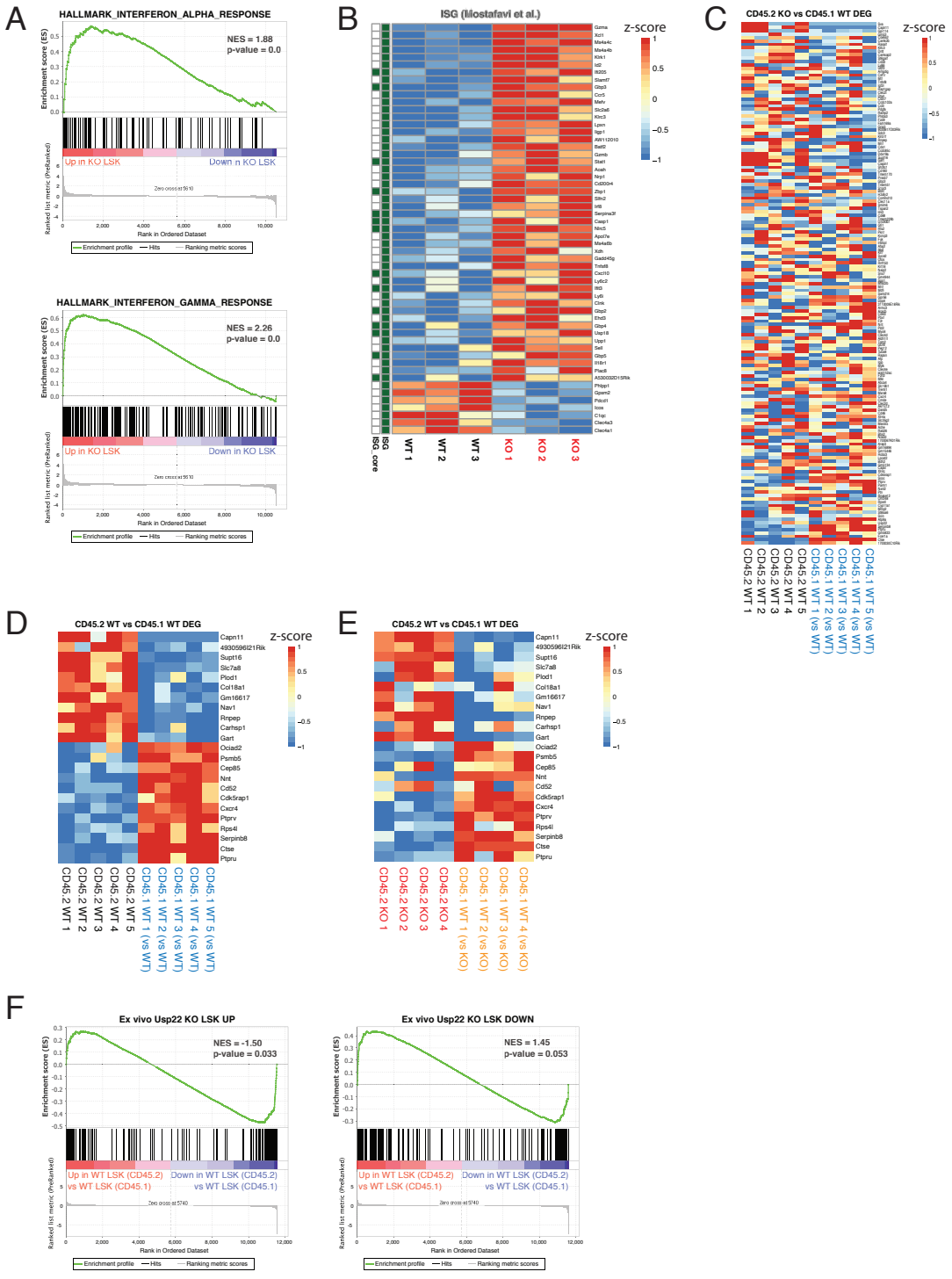

Fig. S7. *Usp22* deficiency drives inflammatory gene expression. (**A**) Gene set enrichment analysis (GSEA) plots comparing wild type and *Usp22* KO LSK for IFN-α target genes (top panel) and IFN-γ target genes (bottom panel). (**B**) Expression levels of all differentially expressed

immune cell ISG *(28)* in LSK isolated from wild type and *Usp22* KO mice. (**C**) Expression of genes shown in Fig. 5E (differentially expressed between *Usp22* KO and wild type LSK isolated from the same host (bottom panel of Fig. 5D)) in $CD45.2^+$ wild type and $CD45.1^+$ wild type LSK from the same host (top panel of Fig. 5D) (n=5 LSK samples per CD45 allotype). (**D**) Heatmap of genes differentially expressed between $CD45.2^+$ wild type and $CD45.1^+$ wild type LSK isolated from the same host (top panel of Fig. 5D) (n=5 LSK samples per CD45 allotype). (**E**) Expression of genes shown in **D** in *Usp22* KO and wild type LSK isolated from the same host (bottom panel of Fig. 5D) (n=4 LSK samples per genotype). (**F**) Gene set enrichment analysis (GSEA) plots comparing $CD45.2^+$ wild type and $CD45.1^+$ wild type LSK from the same recipients (top panel of Fig. 5D) based on DEG shown in Fig. 5A. Enrichment of upregulated and downregulated genes shown in left and right panels, respectively.

Figure S8

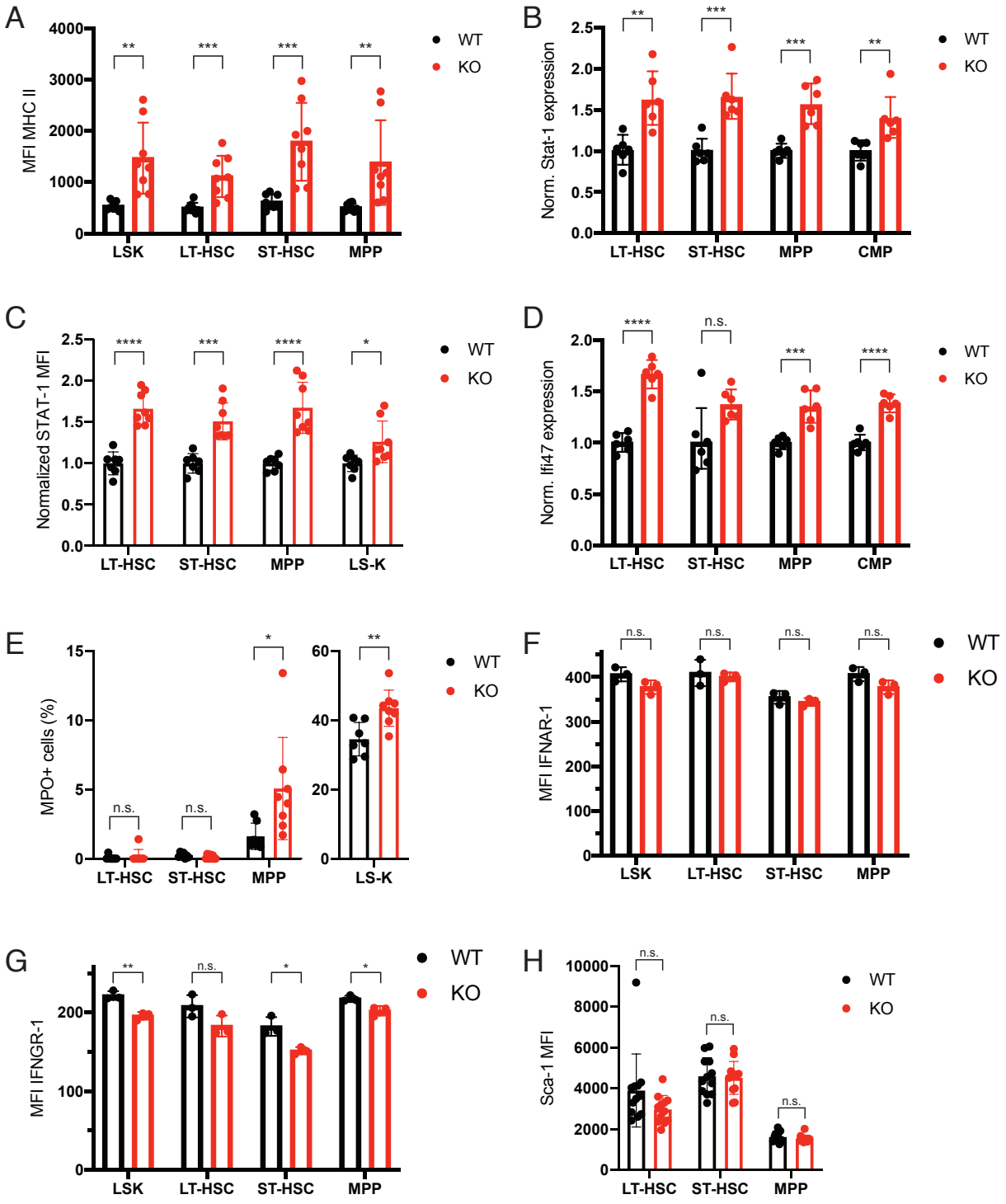

Fig. S8. Analysis of *Usp22* KO HSPC for ISG and Sca-1 expression. (**A**) MHC II median fluorescence intensity (MFI) in wild type and *Usp22* KO stem and progenitor cell populations (n=8 mice per genotype in 3 experiments). (**B**) qRT-PCR analysis for *Stat-1* in wild type and *Usp22* KO

stem and progenitor cell populations (n=6 mice per genotype in 2 experiments). (**C**) Normalized STAT-1 median fluorescence intensity in wild type and *Usp22*-deficient HSPC determined by flow cytometry (n=7-8 mice per genotype in 3 experiments). (**D**) qRT-PCR analysis for *Ifi47* in wild type and *Usp22* KO stem and progenitor cell populations (n=6 mice per genotype in 2 experiments). (**E**) Frequency of myeloperoxidase (MPO)-positive HSPC in wild type and *Usp22* KO mice (n=7-8 mice per genotype in 3 experiments). (**F**+**G**) Median fluorescence intensity (MFI) of IFNAR-1 (**F**) and IFNGR-1 (**G**) in wild type and *Usp22* KO stem and progenitor cell populations (n=3 mice per genotype). (**H**) Sca-1 median fluorescence intensity in wild type and *Usp22* KO HSPC (n=12 mice per genotype in 4 experiments). Mean ± s.d (**A, C, E-H**), geometric mean ± geometric s.d. (**B**, **D**). * $p<0.05$; ** $p<0.01$; *** $p<0.001$; **** $p<0.0001$; n.s. (not significant) by unpaired, two-tailed Student's t-test.

Figure S9

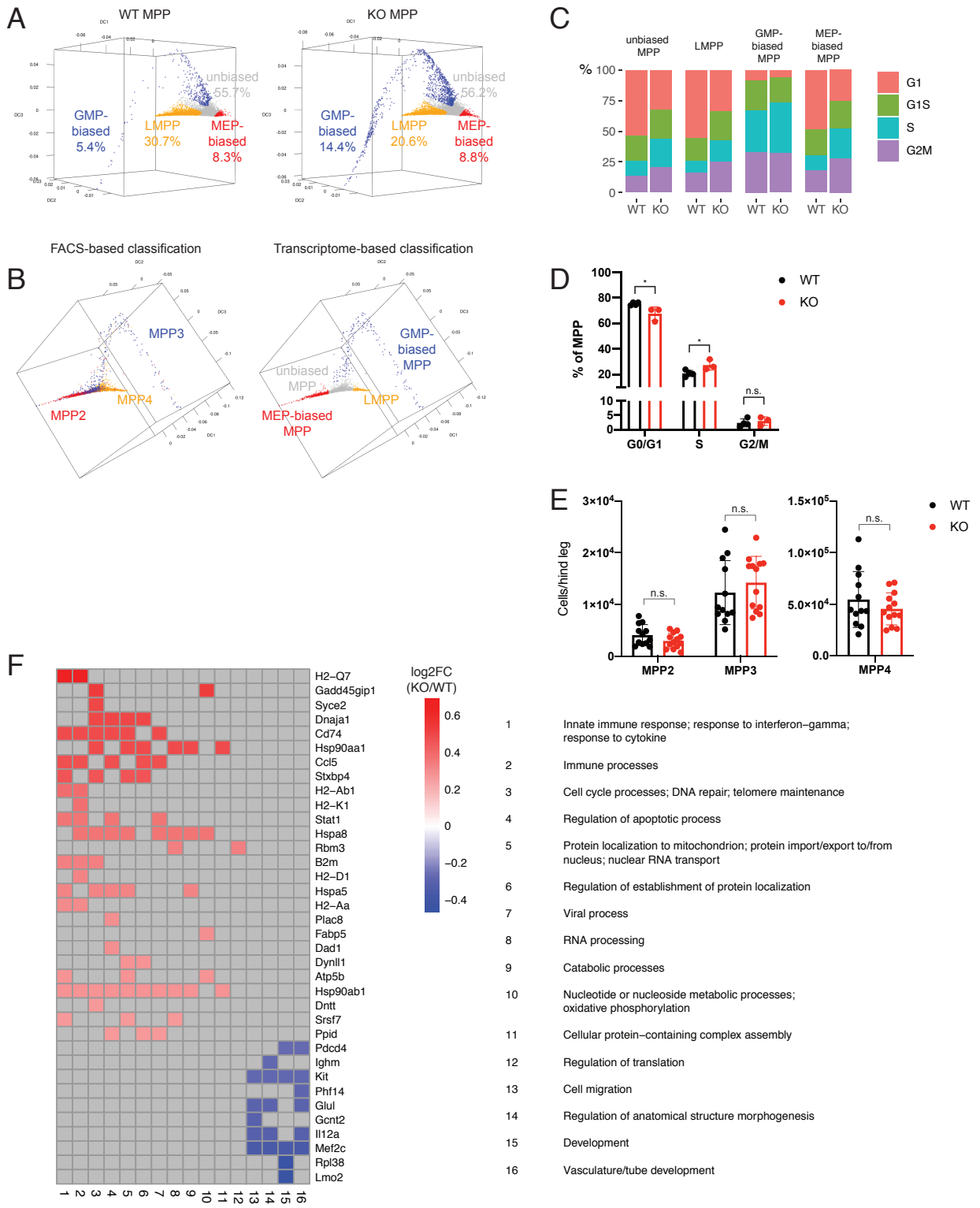

Fig. S9. MPP subsets identified in single-cell RNA sequencing data correspond to lineage-biased MPP subsets. (**A**) Diffusion maps of wild type and *Usp22* KO MPP (experiment 2). (**B**)

Diffusion maps of MPP. Publicly available single-cell RNA sequencing data of sorted MPP2, MPP3 and MPP4 were processed using the workflow described in the present study (Supplementary Methods). In the left panel, cells are color-coded by their cell surface phenotype used for sorting *(32)*; in the right panel cells are color-coded by their transcriptome-based classification. (**C**) Transcriptome-based cell cycle distribution of wild type and *Usp22* KO MPP subsets (experiment 2). (**D**) Cell cycle analysis of wild type and *Usp22* KO MPP based on EdU incorporation (n=3-4 mice per genotype in 2 experiments). (**E**) Absolute numbers of MPP2 (LSK $CD135^-$ $CD48^+$ $CD150^+$), MPP3 (LSK $CD135^-$ $CD48^+$ $CD150^-$) and MPP4 (LSK $CD135^+$ $CD48^+$ $CD150^-$) in the bone marrow of wild type and *Usp22* KO mice (n=12-13 mice per genotype in 3 experiments). (**F**) Heatmaps showing the log2 fold change in expression of genes driving the enrichment of GO groups in fig. S14. Mean ± s.d (**D**). * $p<0.05$; ** $p<0.01$; *** $p<0.001$; **** $p<0.0001$; n.s. (not significant) by unpaired, two-tailed Student's t-test.

Figure S10

Fig. S10. Expression of NK cell- and myeloid lineage-specific transcriptions factors in *Usp22* KO MPP. Average normalized mRNA read counts of the indicated transcription factor genes in

LT-HSC, ST-HSC and MPP subsets from wild type and *Usp22* KO mice determined by scRNA sequencing (n=2 mice per genotype in 2 experiments). Samples that were processed together in the same experiment are connected by grey lines.

Figure S11

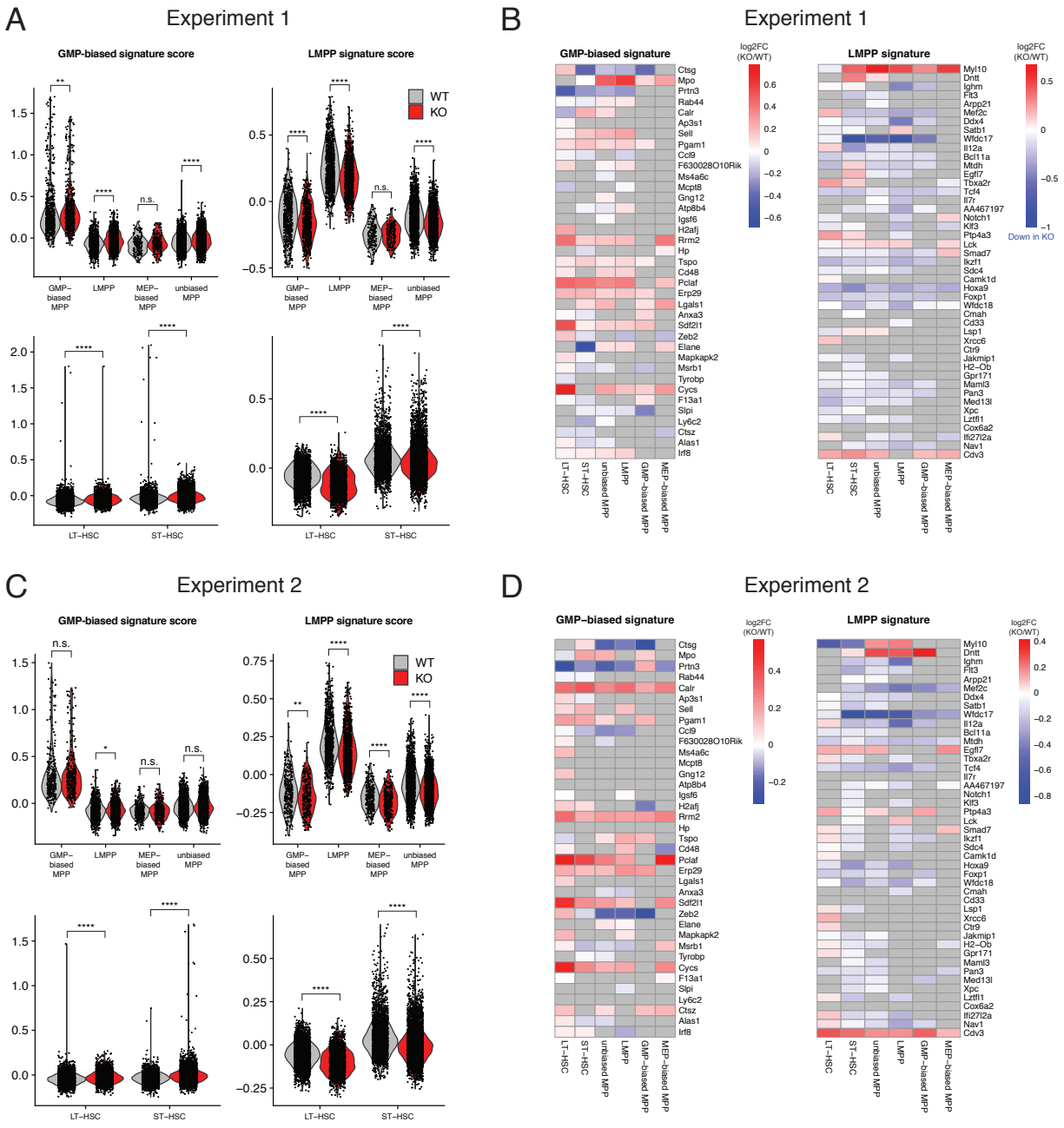

Fig. S11. *Usp22* deficiency enhances myeloid transcriptional priming in HSPC. (**A**+**C**) Violin plots showing cell scores based on the average expression of genes specifically upregulated in GMP-biased MPP (left) or LMPP (right). Scores are compared between wild type and *Usp22* KO within each MPP subset (top) and within LT- and ST-HSC (bottom). Results were obtained from two independent experiments (experiment 1 is shown in **A**, experiment 2 is shown in **C**). (**B**+**D**) Heatmaps showing the log2 fold change in expression of genes used for scores in **A** and **C**. Grey

fields mark insignificant changes with adjusted p-values > 0.05. Experiment 1 is shown in **B**, experiment 2 is shown in **D**.

Figure S12

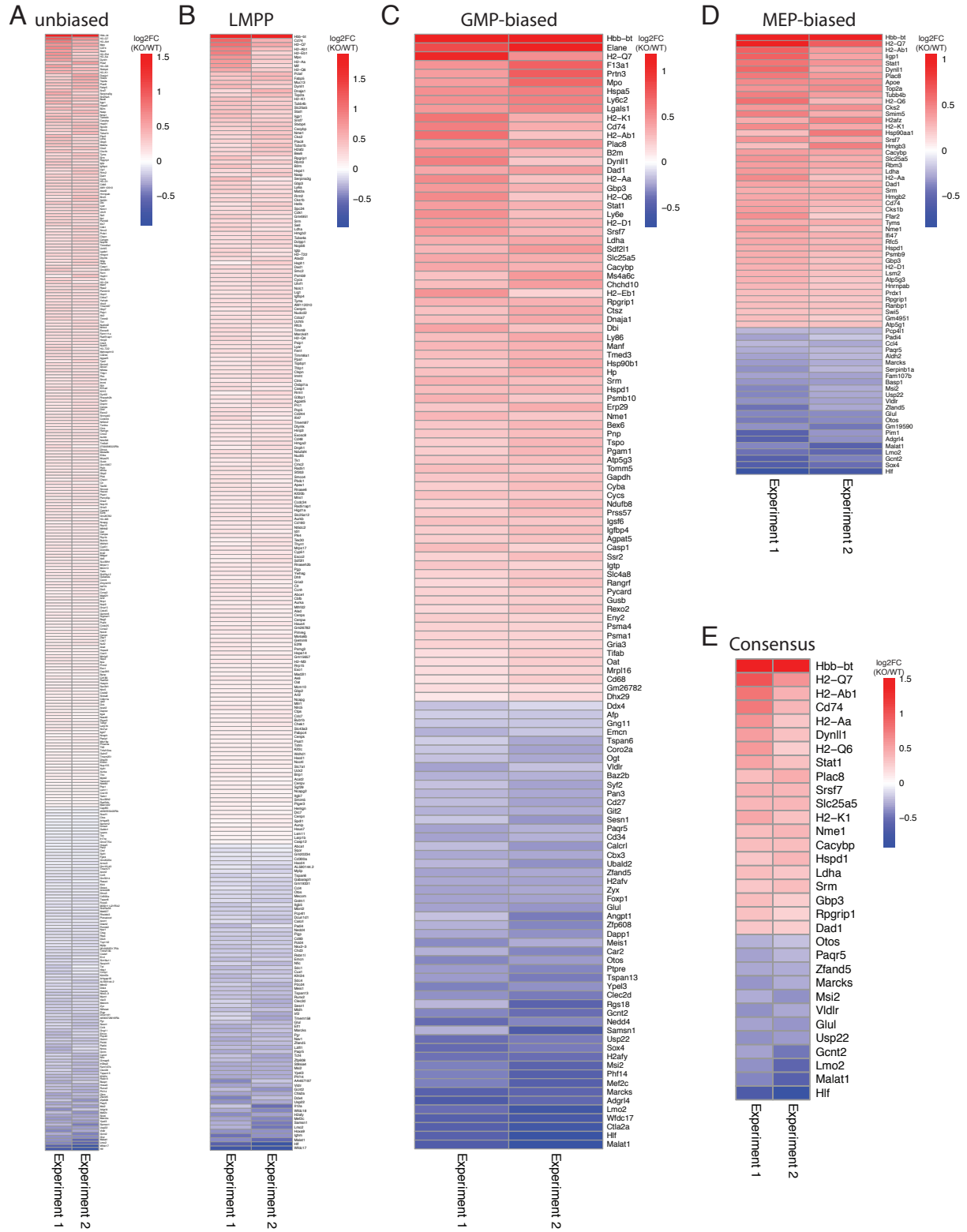

Fig. S12. Transcriptome changes in *Usp22*-deficient MPP subsets. (A-D) Heatmaps showing the log2 fold change in expression of DEG in unbiased MPP (**A**), LMPP (**B**), GMP-biased MPP

(**C**) and MEP-biased MPP (**D**) comparing *Usp22* KO and wild type mice. (**E**) Heatmap showing the log2 fold change in expression of consensus DEG of all MPP subsets shown in **A**-**D**. Log2 fold changes shown are based on all MPP. For gene lists, see also Supplementary data file S2.

Figure S13

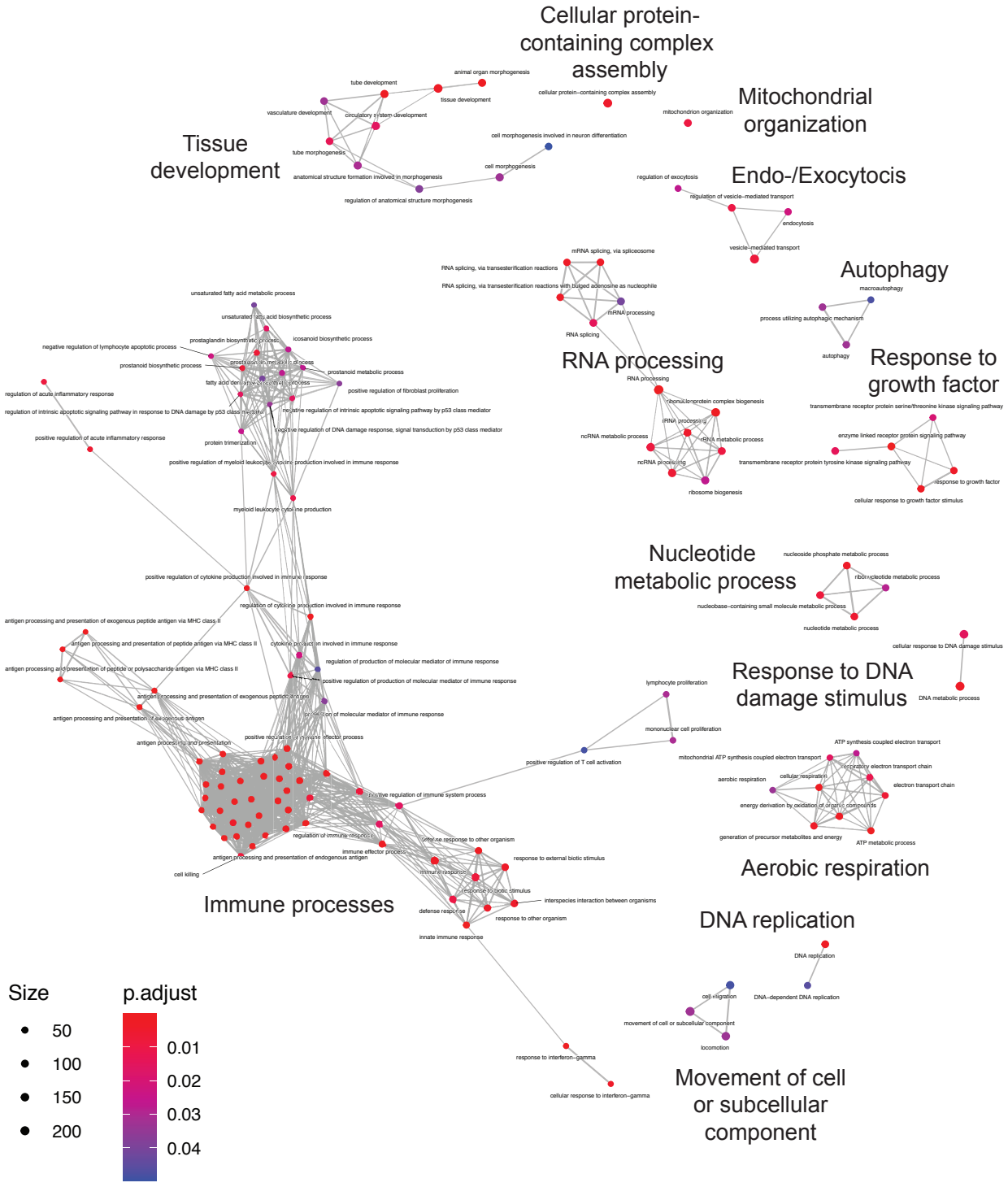

Fig. S13. GO enrichment analysis in *Usp22* KO MPP (experiment 1). Graph of GO terms significantly enriched in *Usp22* KO MPP (adjusted p-value < 0.05). Terms are connected by an edge if their corresponding gene sets have a Jaccard similarity > 0.3. Only groups of GO terms

with more than 70 unique “leading edge” genes in total are shown. Those genes drive the enrichment scores.

Figure S14

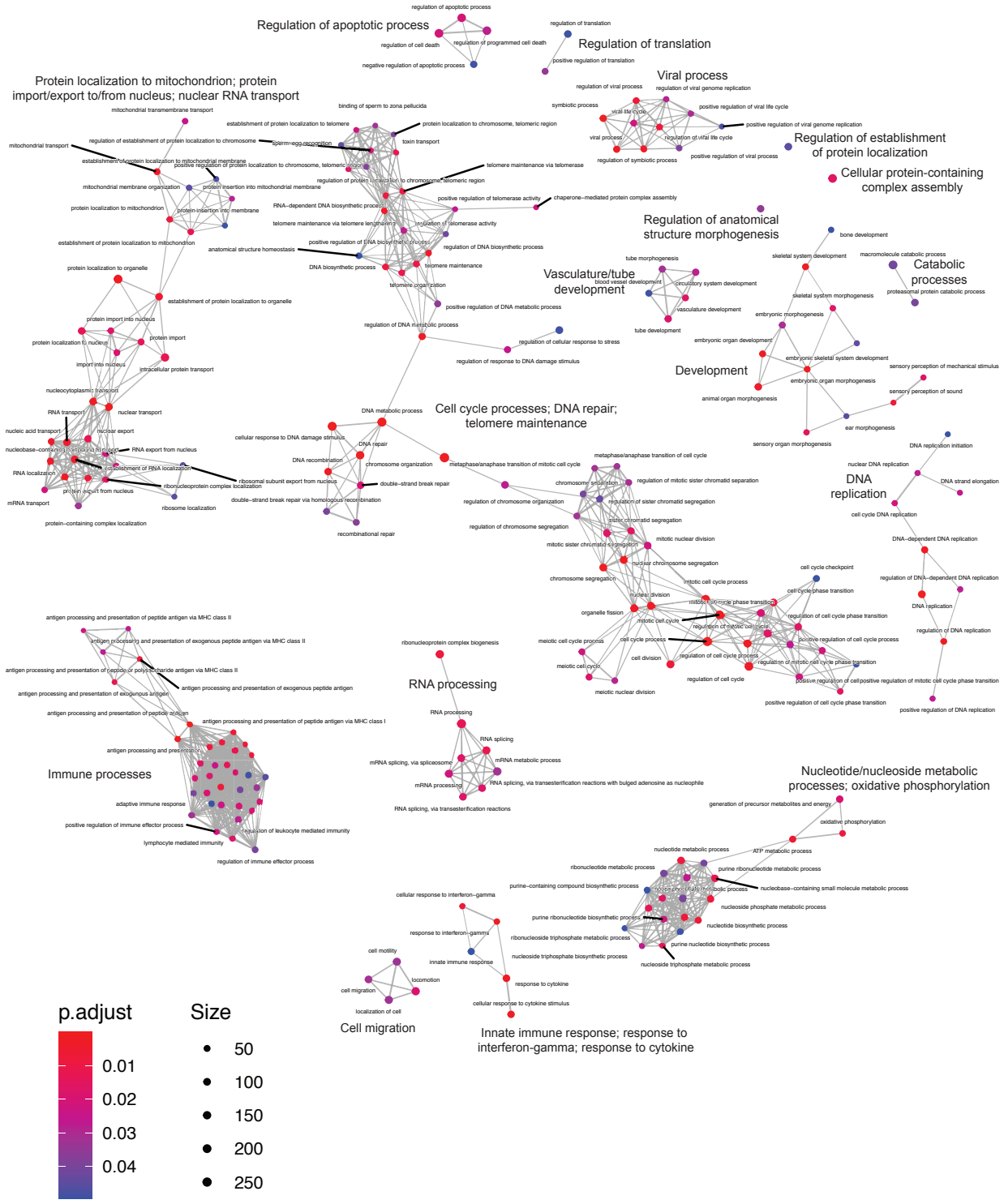

Fig. S14. GO enrichment analysis in *Usp22* KO MPP (experiment 2). Graph of GO terms significantly enriched in *Usp22* KO MPP (adjusted p-value < 0.05). Terms are connected by an

edge if their corresponding gene sets have a Jaccard similarity > 0.3. The threshold of the minimum number of "leading edge" genes per GO group was adjusted to 56 to retain GO groups of sizes comparable to experiment 1. Those genes drive the enrichment scores.

Figure S15

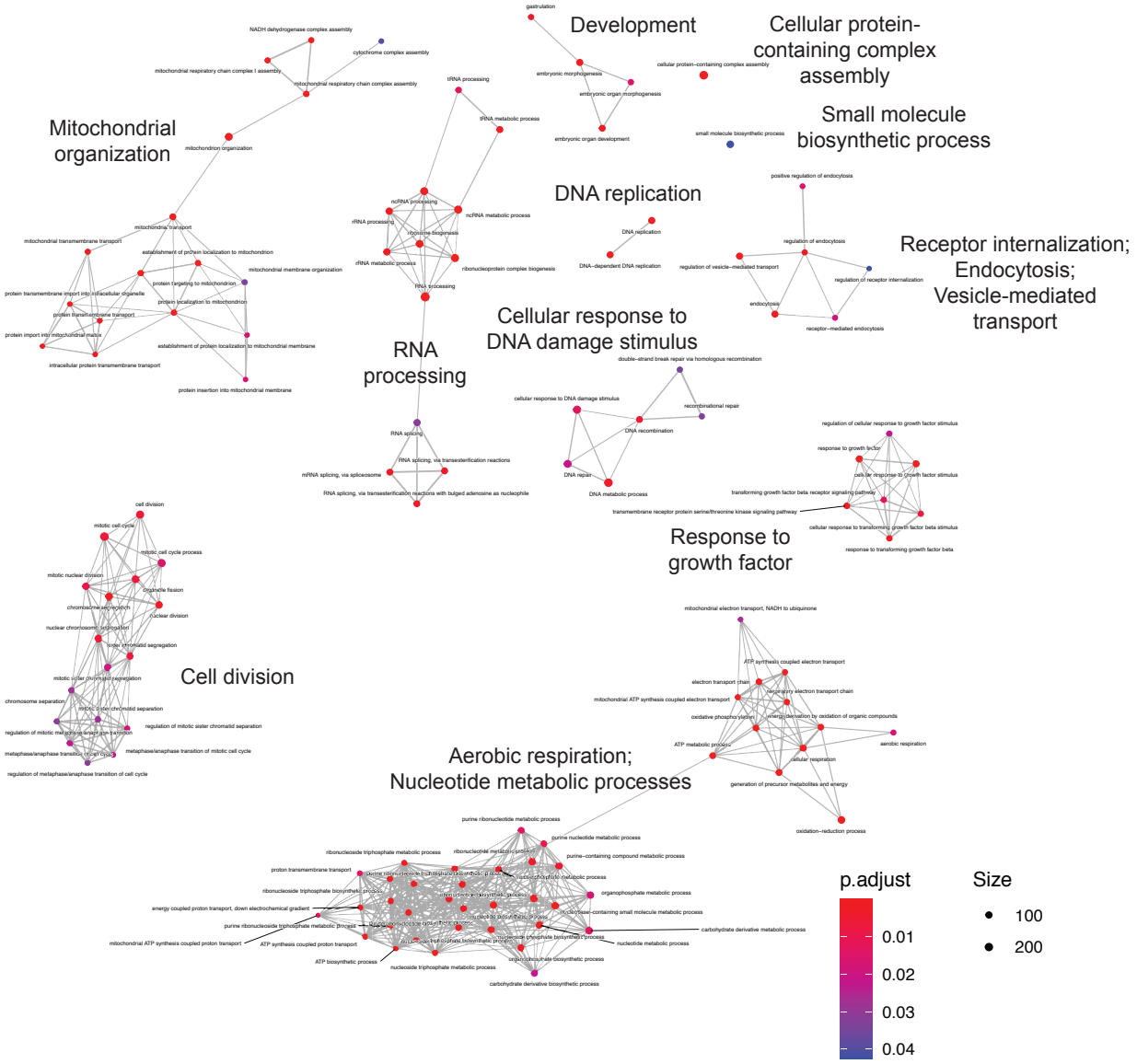

Fig. S15. GO enrichment analysis in *Usp22* KO LT-HSC (experiment 1). Graph of GO terms significantly enriched in *Usp22* KO LT-HSC (adjusted p-value < 0.05). Terms are connected by an edge if their corresponding gene sets have a Jaccard similarity > 0.3. Only groups of GO terms with more than 100 unique "leading edge" genes in total are shown. Those genes drive the enrichment scores.

Figure S16

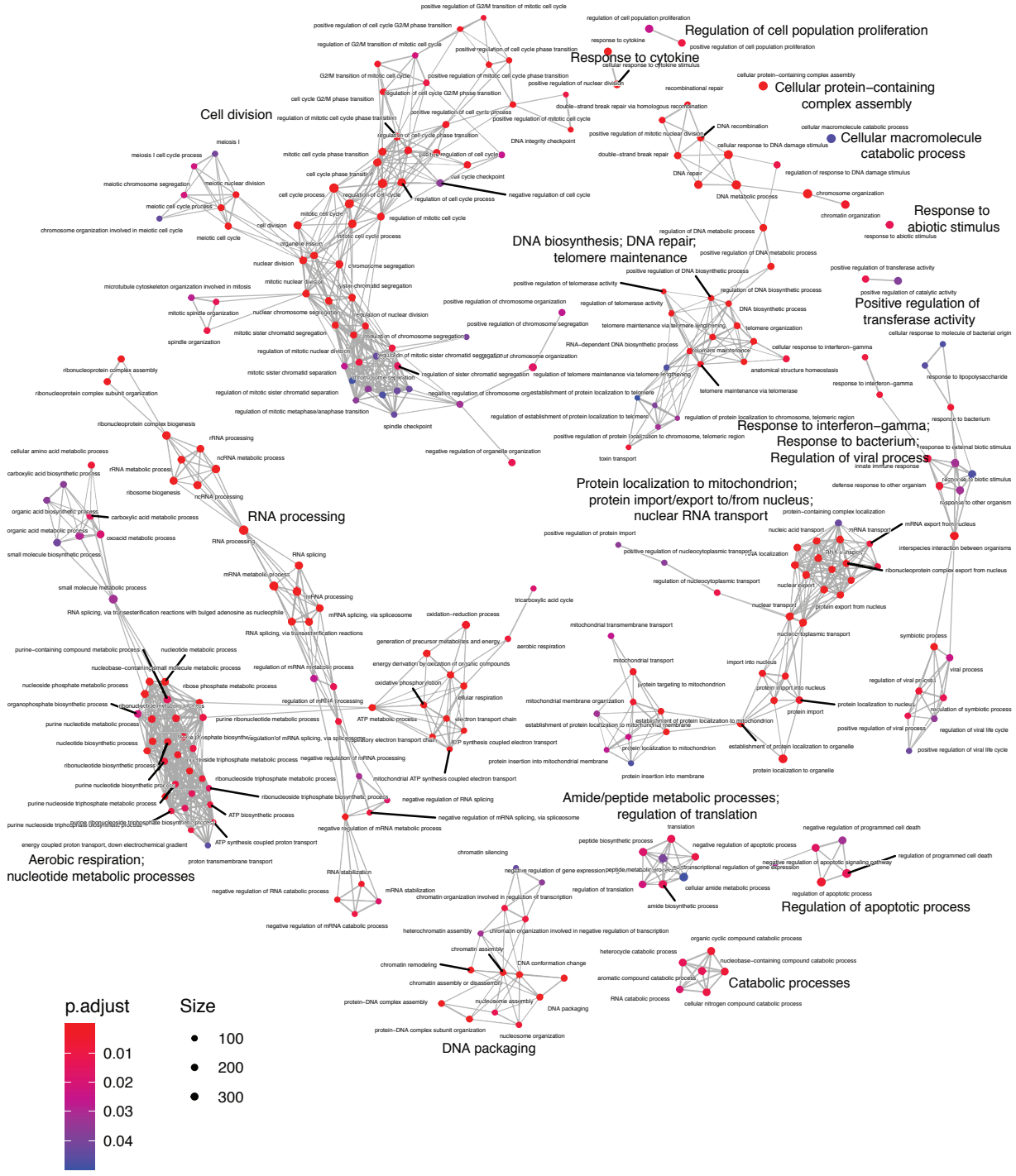

Fig. S16. GO enrichment analysis in *Usp22* KO LT-HSC (experiment 2). Graph of GO terms significantly enriched in *Usp22* KO LT-HSC (adjusted p-value < 0.05). Terms are connected by an edge if their corresponding gene sets have a Jaccard similarity > 0.3. The threshold of the

minimum number of “leading edge” genes per GO group was adjusted to 127 to retain GO groups of sizes comparable to experiment 1. Those genes drive the enrichment scores.

Figure S17

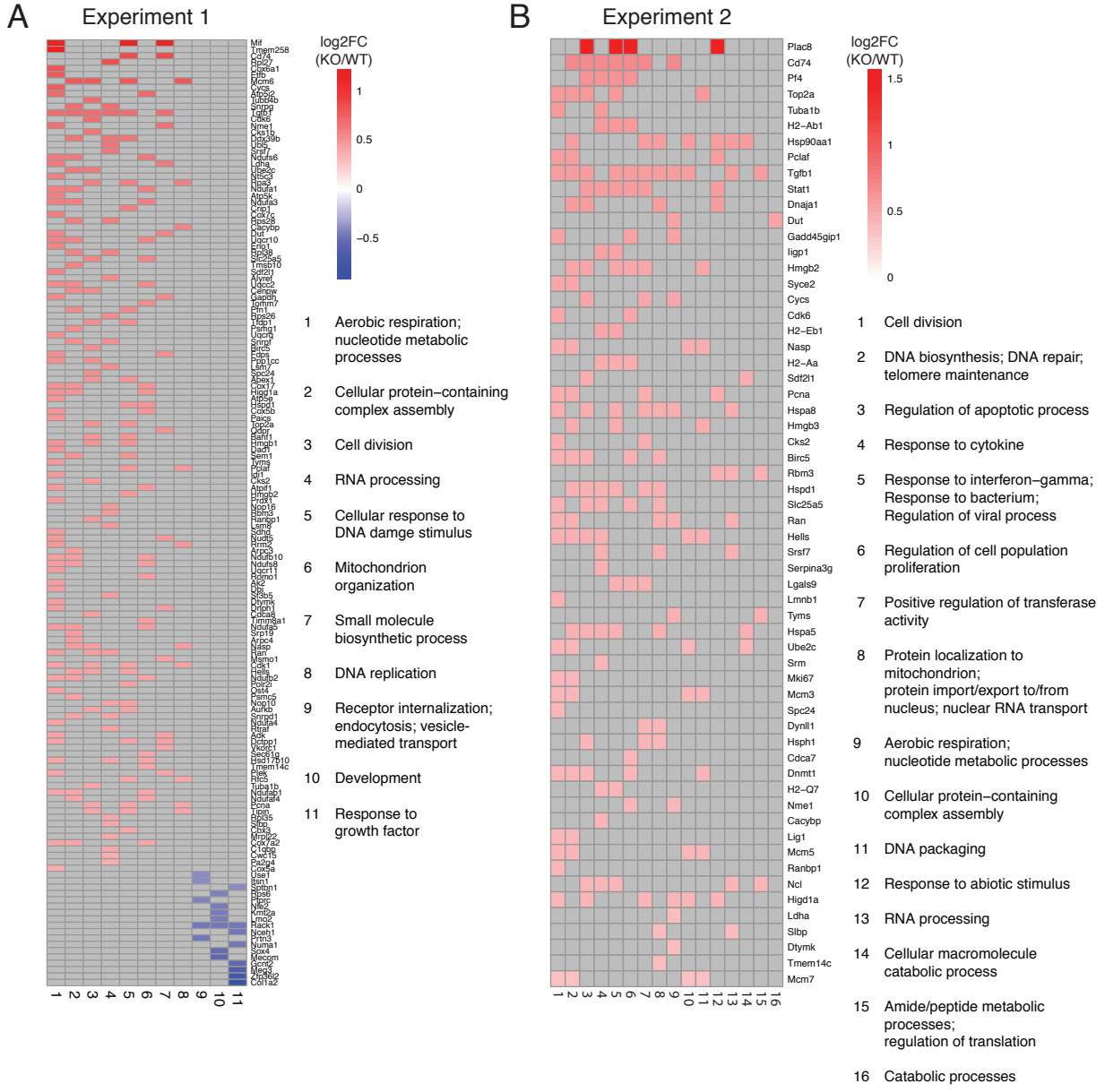

Fig. S17. GO enrichment analysis in *Usp22* KO LT-HSC (experiment 1+2) (**A**+**B**) Heatmaps showing the log2 fold change in expression of genes driving the enrichment of GO groups in fig. S15 (**A**) and fig. S16 (**B**). Only genes with a fold change > 1.3 or < 0.77 are shown. Grey fields indicate genes not contributing to the enrichment of the respective GO group.

Figure S18

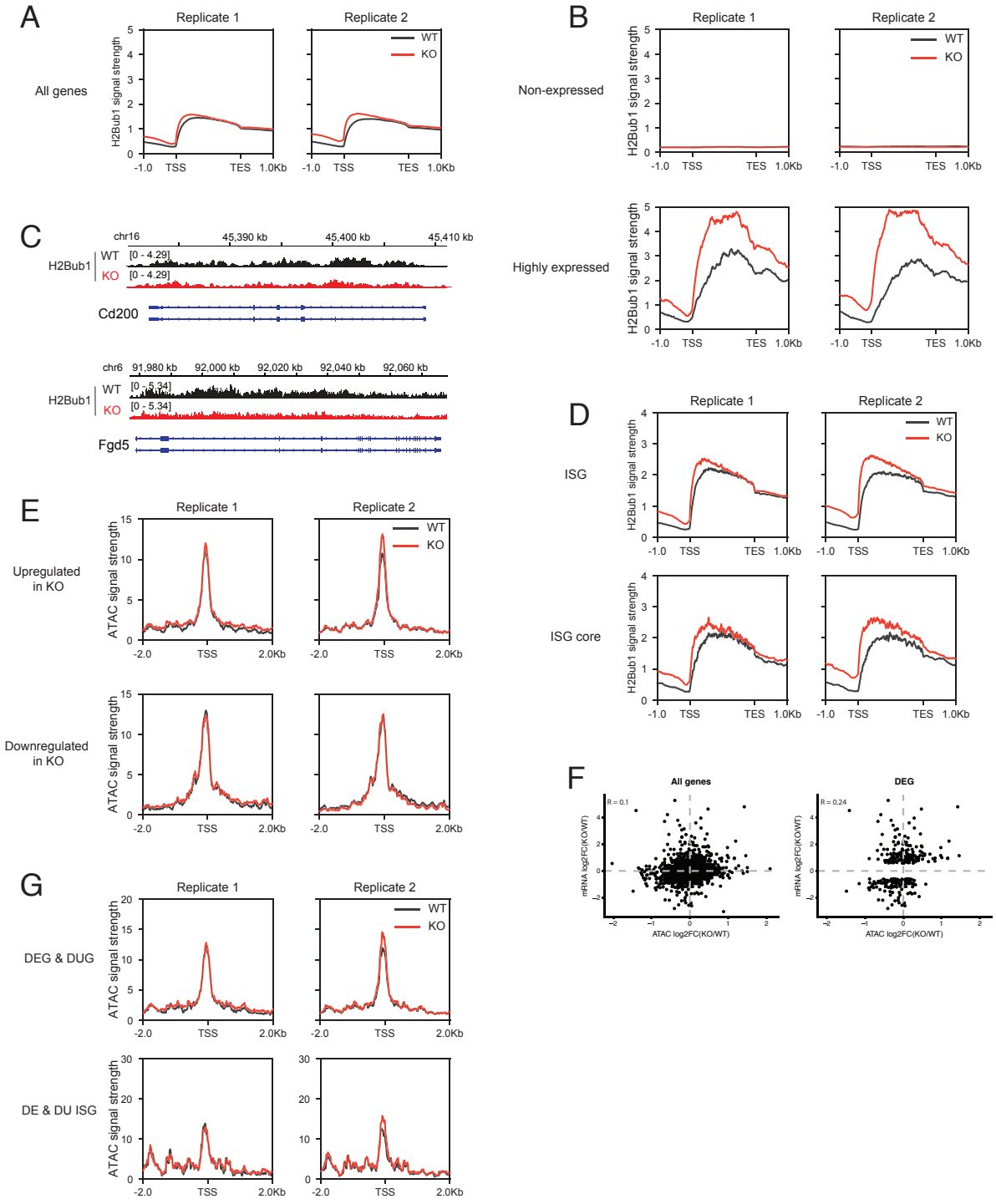

Fig. S18. ***Usp22*** **deficiency increases H2B monoubiquitination at ISG loci.** (**A**+**B**) Average H2Bub1 ChIP sequencing signal in wild type and *Usp22* KO LSK across gene bodies of all genes (**A**), of non-expressed genes (**B**, top panels), and of genes highly expressed in LSK (**B**, bottom panels). (**C**) H2Bub1 ChIP sequencing tracks of *Cd200* (top panel) and *Fgd5* (bottom panel) loci

in wild type and *Usp22* KO LSK. (**D**) Average H2Bub1 ChIP sequencing signal in wild type and *Usp22* KO LSK across gene bodies of all immune cell ISG *(28)* (**D**, top panels), and of the immune cell core ISG *(28)* (**D**, bottom panels). (**E**) Average ATAC sequencing signal around the TSS of genes upregulated in *Usp22* KO LSK (top panels), and of genes downregulated in *Usp22* KO LSK (bottom panels) comparing wild type and *Usp22* KO LSK. (**F**) Correlation between changes in TSS accessibility (measured by ATAC sequencing) and changes in mRNA expression comparing *Usp22* KO and wild type LSK. Each dot represents an individual gene, left panel shows all genes, and right panel only genes differentially expressed between wild type and *Usp22* KO LSK. (**G**) Average ATAC sequencing signal around the TSS of differentially expressed and ubiquitinated genes (top panel), and differentially expressed (DE) and differentially ubiquitinated (DU) ISG (bottom panel) in wild type and *Usp22* KO LSK. TSS = Transcription start site; TES = Transcription end site.

Methodology	Infectious agent	WT (positive/total)	KO (positive/total)
Microbiology	Bacterial infectious agents	0/4	0/4
Molecular biology	Demodex muris	0/4	0/4
	Helicobacter spp.	0/4	0/4
	Mites	0/4	0/4
	Mouse kidney parvovirus	0/4	0/4
	Pneumocystis murina	0/4	0/4
Parasitology (Microscopic)	Ectoparasites	0/4	0/4
	Endoparasites	0/4	0/4
Serology (Bacteria)	Clostridium piliforme	0/4	0/4
	Muribacter muris	0/4	0/4
	Mycoplasma pulmonis	0/4	0/4
	Rodentibacter spp.	0/4	0/4
	Streptobacillus moniliformis	0/4	0/4
Serology (Viruses)	Ectromelia virus	0/4	0/4
	Encephalomyocarditis virus	0/4	0/4
	Hantaan virus	0/4	0/4
	K virus	0/4	0/4
	Lactate dehydrogenase elevating virus	0/4	0/4
	Lymphocytic choriomeningitis virus	0/4	0/4
	Mouse adenovirus FL	0/4	0/4
	Mouse adenovirus K87	0/4	0/4
	Mouse hepatitis virus	0/4	0/4
	Mouse minute virus	0/4	0/4
	Mouse parvovirus	0/4	0/4
	Mouse rotavirus (EDIM)	0/4	0/4
	Murine astrovirus	0/4	0/4
	Murine cytomegalovirus	0/4	0/4
	Murine norovirus	0/4	0/4
	Parvoviruses	0/4	0/4
	Polyoma virus	0/4	0/4
	Puumala virus	0/4	0/4
	Reovirus 3	0/4	0/4
	Sendai virus	0/4	0/4
	Theiler's GD VII virus	0/4	0/4

Table S1. Extended survey for the presence of pathogens in wild type and *Usp22*-deficient mice reveals no signs of infections. Shown is the fraction of mice positively tested for the indicated pathogens (n=4).

Mouse	Sex	Age (weeks)	Analyzed cell populations	Experiment
WT1	female	10.3	TBM, LT-HSC, ST-HSC and MPP	1
KO1	female	10.3	TBM, LT-HSC, ST-HSC and MPP	
WT2	female	11.3	TBM, LT-HSC, ST-HSC and MPP	2
KO2	female	11.7	TBM, LT-HSC, ST-HSC and MPP	

Table S2. Mice used for scRNA sequencing.

Name	Sequence (5'-3')
Ifi47 F	CCTGAAGGAGGGCAGACC
Ifi47 R	GCAGTTACCAGGGAAGCTCA
Sdha F	AAGTTGAGATTTGCCGATGG
Sdha R	TGGTTCTGCATCGACTTCTG
Stat1 F	TGAGATGTCCCGGATAGTGG
Stat1 R	CGCCAGAGAGAAATTCGTGT

Table S3. Primers used for qRT-PCR.

Name	Sequence (5'-3')
Usp22 flox F	TGTGCCCTGGTTGCCCAGTGA
Usp22 flox R	GCACCACCACAGCCGTCCTT
Usp22 flox/delta R	TGGGGAGAGGGTAGACACAG
Usp22 nested F	CTTTCTGTACCTGACCCACCA
Usp22 nested R1	TTTGAGGTTTGAGAATCAAGGTT
Usp22 nested R2	AAATGTTTATGTTAACCAAGAGCAA

Table S4. Primers used for *Usp22* single-cell genotyping.

Name	Sequence (5'-3') (index sequences in red)
Ad1_noMX	AATGATACGGCGACCACCGAGATCTACACTCGTCGGCAGCGTCAGATGTG
Ad2.1_TAAGGCGA	CAAGCAGAAGACGGCATACGAGATTCGCCTTAGTCTCGTGGGCTCGGAGATGT
Ad2.2_CGTACTAG	CAAGCAGAAGACGGCATACGAGATCTAGTACGGTCTCGTGGGCTCGGAGATGT
Ad2.3_AGGCAGAA	CAAGCAGAAGACGGCATACGAGATTTCTGCCTGTCTCGTGGGCTCGGAGATGT
Ad2.4_TCCTGAGC	CAAGCAGAAGACGGCATACGAGATGCTCAGGAGTCTCGTGGGCTCGGAGATGT

Table S5. Indexing primers used for the preparation of ChIP and ATAC sequencing libraries.